

UNCLASSIFIED

AD NUMBER
AD843063
NEW LIMITATION CHANGE
TO Approved for public release, distribution unlimited
FROM Distribution authorized to U.S. Gov't. agencies and their contractors; Administrative/Operational use; Oct 1968. Other requests shall be referred to Air Force Aero Propulsion Laboratory, WPAFB, Ohio 45433.
AUTHORITY
AFAPL ltr, 12 Apr 1972

THIS PAGE IS UNCLASSIFIED

AD843063

AFAPL-TR-68-100

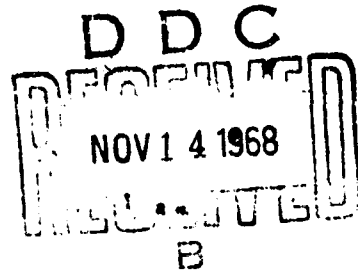
INVESTIGATION OF SUPERCRITICAL
(FEHER) CYCLE

E. G. Feher et al.

Astropower Laboratory, Missile & Space Systems Division
A Division of McDonnell Douglas Corporation

TECHNICAL REPORT AFAPL-TR-68-100

October 1968



STATEMENT OF WORK

This document is subject to special export controls and its
transmittal to foreign governments or foreign nationals may be
made only with prior approval of _____

Air Force Aero Propulsion Laboratory
Air Force Systems Command
United States Air Force

Att: AFIP

PROJECT	W 11 11 11				
ORG	ENR SECTION				
UNCLASSIFIED					
JUSTIFICATION					
BY					
DISTRIBUTION AVAILABILITY					
<table border="1"> <tr> <th>QST.</th> <th>AVAIL. MOD. OR SPEC.</th> </tr> <tr> <td>2</td> <td></td> </tr> </table>	QST.	AVAIL. MOD. OR SPEC.	2		
QST.	AVAIL. MOD. OR SPEC.				
2					

NOTICE

When Government drawings, specifications, or other data are used for any purpose other than in connection with a definitely related Government procurement operation, the United States Government thereby incurs no responsibility nor any obligation whatsoever; and the fact that the Government may have formulated, furnished, or in any way supplied the said drawings, specifications, or other data, is not to be regarded by implication or otherwise as in any manner licensing the holder to any other person or corporation, or conveying any rights or permission to manufacture, use, or sell any patented invention that may in any way be related thereto.

Copies of this report should not be returned unless return is required by security considerations, contractual obligations, or notice on a specific document

ABSTRACT

Preliminary Design of the XFCTAP 01-01 Combined Rotating Unit (CRU) is described in this report. The unit is intended for the investigation of Supercritical (Feher) cycle engine components.

The CRU consists of a single stage axial reaction turbine, a single stage radial pump and a solid rotor alternator with its rotor supported on self-acting radial and thrust bearings with working fluid lubrication. The working fluid is supercritical CO₂. Net power output of the CRU is 10 kWe at a design speed of 80,000 RPM.

In addition, this report covers the design of an Air Turbine Test Configuration intended to verify the performance of the CRU turbine with compressed air under dynamically similar conditions prior to testing with high temperature supercritical CO₂. The air turbine test unit includes an air dynamometer. The turbine is attached to the dynamometer shaft for direct torque measurement. The housing provides means for regulating air flow rate.

Both the CRU and the Air Turbine Unit are fully instrumented to yield data on pressures, temperatures, flow rates, and electrical power from which the performance of the various components can be determined.

Investigation of the feasibility of miniaturized turbine fabrication resulted in the conclusion that these components can be made to specifications that will yield a turbine efficiency of about 0.70 and a pump efficiency of about 0.67 at the design point. The alternator efficiency is estimated to be about 0.89.

It is recommended that these preliminary designs be carried through final design and that the units be fabricated and tested.

AFAPL-TR-68-100

**INVESTIGATION OF SUPERCRITICAL
(FEHER) CYCLE**

E. G. Feher et al.

**Astropower Laboratory, Missile & Space Systems Division
A Division of McDonnell Douglas Corporation**

FOREWORD

This technical report is on Contract F33615-67-C-1924 covering the Combined Rotating Unit Preliminary Design and Air Turbine Preliminary Design.

Work on this contract was carried out between 1 July 1967 and 15 May 1968 at Astropower Laboratory, Advance Systems and Technology, Douglas Missile and Space Systems Division, McDonnell Douglas Corporation under the supervision of Dr. G. Moe, Director of Astropower. This report was submitted for approval on 14 June 1968. Mr. E. G. Feher, Section Chief, Feher Cycle Program was Study Director. E. A. Brass, Senior Engineering Specialist executed the mechanical design studies. J. E. Drever, Research Engineer performed the instrumentation. A. H. Fink, Engineering Specialist, conducted the cycle optimization and component matching and design studies. R. A. Harvey, Engineering Specialist contributed to all technical areas. Detailed component loss analysis and associated tradeoff studies relating to turbo-machinery flow path configurations and to aerothermal performance were conducted by Dr. O. E. Balje, technical consultant to Astropower Laboratory. Analysis and preliminary design of the solid rotor alternator was performed by North American Rockwell Corporation. The program was administered by the Air Force Aero Propulsion Laboratory, Wright Patterson Air Force Base, Ohio under the technical direction of Mr. Lloyd M. Hedgepeth.

Publication of this report does not constitute Air Force approval of the report's findings or conclusions. It is published only for the exchange and stimulation of ideas.

Philip E. Stover

PHILIP E. STOVER
Act'g Chief, Propulsion & Power Branch
Aerospace Power Division

CONTENTS

Section I	INTRODUCTION	1
Section II	CHARACTERISTICS OF THE SUPERCRITICAL (FEHER) CYCLE	3
	1. Description of Cycle	3
	2. Working Fluids and Their Properties	3
	3. Cycle Performance Analysis	5
	4. Cycle Performance Considerations	9
Section III	CRU PRELIMINARY DESIGN	11
	1. Initial Cycle Selection	11
	2. Turbine and Pump Analysis	13
	a. General Discussion	13
	b. Configuration and Performance Analysis Using Design Point Data	21
	c. Turbine Design Point Selection	25
	d. Pump Performance Considerations	28
	e. Final Design Point Selection and Pump Calculation	29
	3. Bearings	29
	4. Rotor Dynamics	38
	5. Alternator Analysis and Preliminary Design	44
	a. Alternate Generator Types	45
	b. Power-Speed Trade Off Study	50
	c. Selected Preliminary Design	64
	d. Thermal Analysis	70
	e. Results	71
	f. Alternator Test Procedure	75
	6. Turbine Design	82
	a. Sub-base	82
	b. Scrolls	82
	c. Shroud	84
	d. Thermal Considerations	87
	e. Turbine Flow Losses	88
	7. Pump Design	88
	a. Rotor	88
	b. Diffuser	90
	c. Seal	90

8.	Design Integration	91
a.	General Arrangement	91
b.	Principal CRU Structure	94
c.	Alternator Installation	94
d.	Rotor Design	96
e.	Bearing Construction	96
f.	Pressure Containment	98
9.	Turbine Fabrication	100
a.	Douglas Company Welding Facility Santa Monica, California	104
b.	Company A	104
c.	Company B	105
d.	Company C	105
e.	Company D	105
f.	Company E	106
10.	Instrumentation	107
a.	Purpose of Instrumentation	107
b.	Measurements Required and Methods	107
c.	Turbine and Pump Instrumentation Assemblies	111
d.	Data Error Analysis	113
Section IV	AIR TURBINE PRELIMINARY DESIGN	119
1.	Definition of Air Test Conditions	119
a.	Establishment of the Air Test Conditions Equivalent to the Turbine Design Point	122
b.	Review of the Equivalent Air Test Conditions	123
2.	Design Integration	124
a.	Rotor Dynamics	125
b.	Bearing Thrust	129
3.	Instrumentation	130
Section V	CONCLUSIONS AND RECOMMENDATIONS	133
1.	Conclusions	133
2.	Recommendations	133
	REFERENCES	135

FIGURES

1	Feher Cycle Superimposed on a Mollier Diagram	4
2	Recuperator Enthalpy vs Pump Outlet Pressure	6
3	Cycle Efficiency as a Function of Pressure Ratio	8
4	Feher Cycle Performance Spectrum at the 10 kW Power Level (Single Stage Turbine)	12
5	Typical $N_s D_s$ Diagram for Turbines	15
6	Simplified Diagram for Turbines, Maximum Efficiency - N_s	17
7	Optimum Turbine Geometry	18
8	Simplified Diagram for Pumps, Maximum Efficiency - N_s	19
9	Optimum Pump Geometry	20
10	Turbine Diameter, Blade Chord and Blade Height as a Function of Degree of Reaction	22
11	Turbine Blade Angle and Blade Number as a Function of Degree of Reaction	23
12	Turbine Thrust as a Function of Degree of Reaction	24
13	Trailing Edge Thickness and Exit Velocity Loss as a Function of Degree of Reaction	24
14	Turbine Efficiency as a Function of Blade Trailing Edge Thickness and Chord Ratio, Assuming Hydraulically Smooth Surface	26
15	Turbine Efficiency as a Function of Blade Surface Roughness	27
16	Comparison of Bearing Load Carrying Capacity Incompressible Theory vs Compressible Theory	34
17	10 kW _e CRU Radial Bearing Performance	37
18	Thrust Bearing Analysis	39
19	Rotor Critical Speeds vs Bearing Stiffness	42
20	Generator Principles	47
21	Nadyne Alternator Concept	49
22	11 kW Nadyne Rotor	52
23	11 kW Stator and Housing Assembly	53
24	5.5 kW 2-Pole Nadyne Alternator Trade-Off Parameters	57
25	5.5 kW 2-Pole Nadyne Alternator Weight-Efficiency Trade-Off	58

26	Fluid Churning Load Measurements	61
27	Parametric Data 5.5 kW Nadyne 2 Pole	62
28	Parametric Data 5.5 kW Nadyne 4 Pole	63
29	Generator - 10 kW Nadyne 80,000 RPM, 2 Pole	65
30	DC Magnetization Curves at Room Temperature	68
31	Temperatures (°F) Resulting from Various Flows of Carbon Dioxide	72
32	Effect of Flow of Internal Coolant (CO ₂) on Heat Loads	74
33	Temperatures (°F) Resulting from Various Frame Temperatures	76
34	Effect of Frame Temperature on Heat Loads	77
35	Turbine Section	83
36	Turbine Scroll Analysis	85
37	Turbine Shroud Deflection	86
38	Pump Section	89
39	CRU Layout	92
40	Feher Cycle Combined Rotating Unit, 10 kWe Test Model KFCTAP 01-01	93
41	Feher Cycle Combined Rotating Unit, 10 kWe Test Model KFCTAP 01-01	95
42	10 kWe CRU Rotor Assembly Check	97
43	Bearing Attachment	99
44	Turbine Assembly 10 kW Feher Engine	101
45	Turbine Rotor	102
46	Turbine Blade	103
47	CRU Instrumentation Schematic	108
48	Turbine Instrumentation	112
49	Pump Instrumentation	114
50	Air Turbine Test Configuration	126
51	Air Turbine Assembly	127
52	Rotor Proportions	128
53	Air Turbine Instrumentation	132

TABLES

I	Critical Constants of Working Fluids	2
II	Initial Selection of Turbine and Pump Characteristics	14
III	First Turbine Design	28
IV	Final Test Unit Design Point	30
V	General Component Specification	30
VI	Final Turbine Specifications	30
VII	Pump Specifications	31
VIII	Air Bearing Performance: Compressibility Factor and Load Carrying Capability as Functions of Radial Clearance Ratio	33
IX	Viscosity Characteristics of Various Fluids	33
X	Performance Summary	51
XI	List of Primary Design Variables	54
XII	Machine Ratings and Performance Parameters	66
XIII	Weight Breakdown	66
XIV	Loss Breakdown	66

LIST OF ABBREVIATIONS AND SYMBOLS

b_p	Pump rotor exit blade width (in.)
C	Turbine chord length (inch)
C_o	Optimum chord length (in.)
C_s	Acoustic velocity in working fluid at turbine rotor inlet
c_o	Turbine spouting velocity = $\sqrt{2g\delta h_T}$ (ft per sec)
c_3	Turbine exhaust velocity (ft per sec)
D	Turbine hub diameter (inch)
D_s	Specific diameter
e_r	Recuperator efficiency
F_{thr}	Turbine thrust (lb)
g	Gravitational constant (32.2 ft/sec ²)
h	Enthalpy
H_{ad}	Adiabatic head
h_t	Turbine blade height (inch)
δh_{pinch}	"Pinch" enthalpy differential
δh_θ	Approach temperature enthalpy differential
δh_T	Ideal turbine head
k	Surface roughness
M_a^*	U/C_s = peripheral Mach number
N	CRU rotational speed (rpm)
N_s	Specific speed
P	Pressure (psia)
ΔP^*	Characteristic half-cycle parasitic pressure loss
S	Turbine tip clearance
T	Temperature (^o F)
U	Turbine blade tip velocity (ft/sec)
t_e	Turbine blade trailing edge thickness (inch)
V	Volume flow rate (ft ³ /sec)
W	Weight flow rate (lb/sec)

Z_N	Turbine nozzle blade number
Z_R	Turbine rotor blade number

Greek Symbols

α_2	Nozzle exhaust flow angle ($^\circ$)
α_3	Turbine exhaust flow angle ($^\circ$)
β_2	Turbine rotor inlet blade angle ($^\circ$)
β_3	Turbine rotor exit blade angle ($^\circ$)
η_{cy}	Cycle thermal efficiency
η_p	Pump efficiency
η_t	Turbine efficiency
ρ	Turbine degree of reaction

Subscripts

a	Heat sink exchanger outlet and pump inlet
b	Pump discharge and recuperator inlet
c	High pressure side recuperator outlet and heater inlet
d	Turbine inlet
e	Turbine outlet and recuperator inlet
f	Low pressure side recuperator outlet and heat sink exchanger inlet
T, t	Turbine
P, p	Pump

Other symbols are defined as they appear in the text.

BLANK PAGE

SECTION I

INTRODUCTION

The purpose of this study is to investigate certain aspects of the Supercritical (Feher) cycle. In this phase the preliminary design of a Combined Rotating Unit (CRU) has been completed. This CRU is intended to test the dynamic components of an engine based on this cycle. Additionally, the preliminary design of an Air Turbine Test Unit has been completed. This unit will be used to pretest the turbine prior to testing in the CRU.

The supercritical (Feher) cycle is a new concept in dynamic energy conversion. It is characterized by high thermal efficiency, compact components, and mechanical simplicity. Additional advantages of this cycle are, (1) no abrupt phase change occurs in the cycle and therefore no erosion of turbine blades due to vapor quality, (2) elevation of pump inlet pressure well above critical prevents the occurrence of cavitation in the pump, (3) high fluid densities result in smaller components than are characteristic of other power cycles, and (4) the characteristic high thermal efficiency can be obtained with a single stage pump and a small diameter turbine of one or two stages.

A detailed description of the Supercritical (Feher) cycle can be found in Reference 1.

TABLE I. CRITICAL CONSTANTS OF WORKING FLUIDS

<u>Name</u>	<u>Formula</u>	<u>Critical Temperature (°F)</u>	<u>Critical Pressure (psia)</u>
Ammonia	NH ₃	271.2	1636
Carbon Dioxide	CO ₂	87.8	1072
Hexafluorobenzene	C ₆ F ₆	460	402
Perfluoropropane	C ₃ F ₈	161.4	388
Sulfur Dioxide	SO ₂	315.5	1143
Sulfur Hexafluoride	SF ₆	114	546
Water	H ₂ O	705	3206
Xenon	Xe	61.9	853

SECTION II

CHARACTERISTICS OF THE SUPERCRITICAL (FEHER) CYCLE

1. DESCRIPTION OF CYCLE

The supercritical (Feher) cycle power conversion system is similar to both the Rankine and Brayton dynamic power cycles in that (1) head is produced by pumping a working fluid from a lower to higher pressure level, (2) heat is added to the high pressure fluid at constant pressure thereby elevating the temperature to a maximum compatible with the metallurgy of the equipment, (3) the fluid is expanded back to the lower pressure level through a turbine producing work, and (4) the residual unused thermal energy is rejected at constant pressure by cooling the low pressure working fluid back to its original pump inlet condition.

From a thermodynamic viewpoint the three cycles differ radically due to the differing pressure levels and properties of working fluids used for each. Brayton cycle efficiency is essentially limited by a characteristic compression work factor. Rankine vapor cycle performance is inherently limited by the condensing-boiling process which precludes major energy recovery from the turbine exhaust flow.

The Feher cycle, by operating at supercritical pressures, retains the most efficient aspects of both the Brayton and Rankine cycles (i. e. , a high degree of recuperation plus a relatively low pump work factor) and thus is capable of providing higher cycle efficiency than either of the other two.

2. WORKING FLUIDS AND THEIR PROPERTIES

In principle, the Supercritical Cycle can be operated with any fluid just as a Brayton Cycle can be operated with any gas. In practice, the choice of working fluid controls the range of cycle operating pressures and temperatures. Table I lists critical properties of some of the working fluids that can be used in practical applications.

For initial investigations carbon dioxide was selected as the working fluid for several reasons. First, its critical pressure is one third that of water, allowing lower operating pressures. Second, it is known to be a stable and inert material throughout the temperature range of interest. Third, there is a considerable body of literature on the properties of carbon dioxide, hence cycle analysis is based on reasonably firm data. And finally, carbon dioxide is abundant, nontoxic, and relatively inexpensive.

The thermodynamic and transport properties of carbon dioxide were assembled from several sources, notably from R. L. Sweigert, et al., (Ref. 2), G. C. Kennedy (Ref. 3), D. Price (Ref. 4), D. M. Newitt, et al., (Ref. 5) and L. H. Chen (Ref. 6). This data covers the temperature range

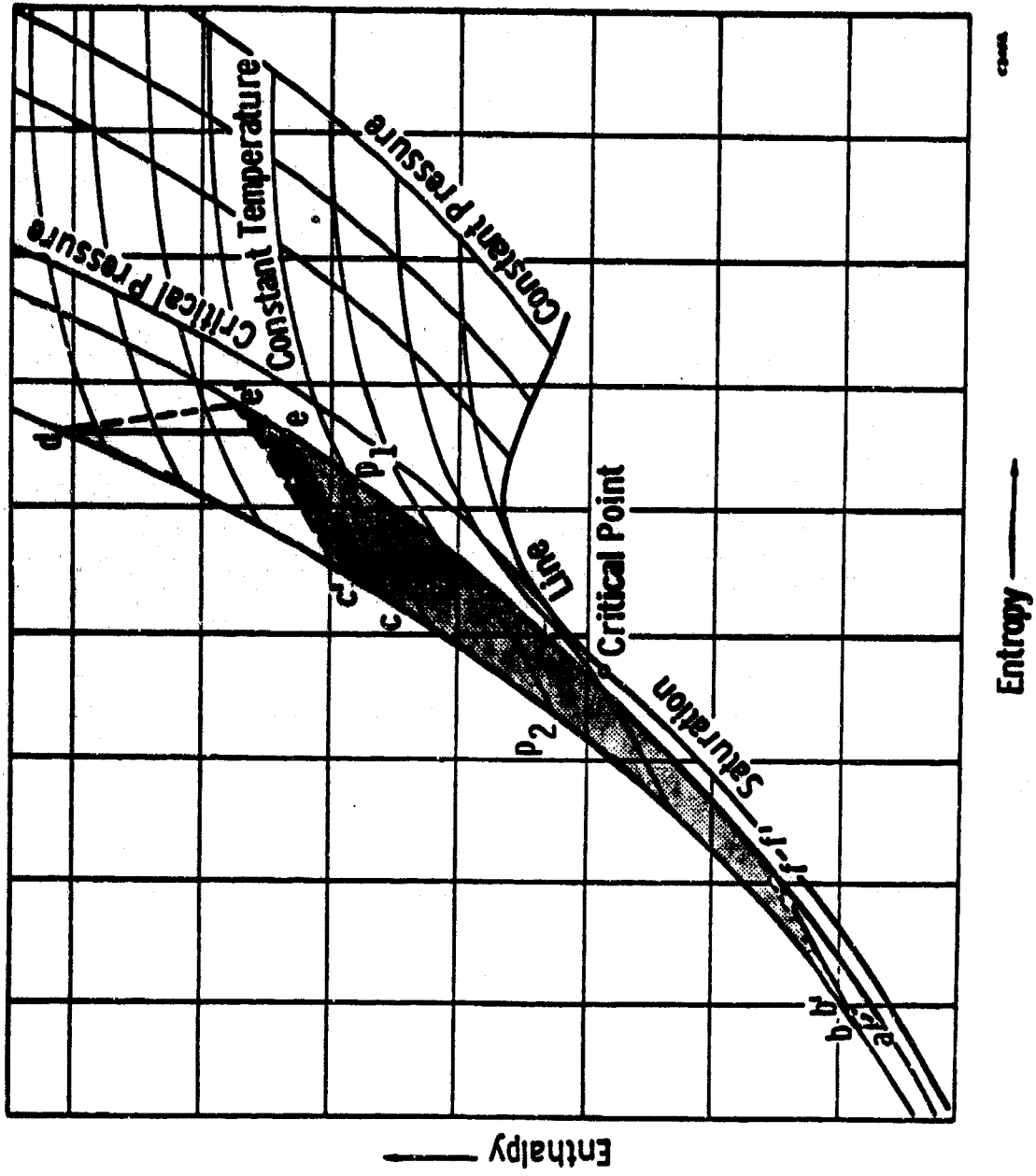


Figure 1. Feher Cycle Superimposed on a Mollier Diagram

from 32°F to 1800°F and the pressure range from 0 to 500 atmospheres.

The properties of carbon dioxide as a working fluid are very good. There are some cautionary points, but in general its behavior is close to ideal. The molecular weight of 44 gives rise to extremely dense working fluid conditions at the high pressures involved thereby reducing the working fluid volume flow and the size of associated equipment. The triatomic molecular structure and consequent low specific heat ratio mean that the gas dynamic machines proposed are limited more by gas density considerations than by rotating machinery tip speed.

Carbon dioxide is very stable. At the pressures involved, dissociation is less than 5 parts in 100 million at 1300°F. It will oxidize steels slowly at elevated temperatures but at a rate substantially less than air and markedly less than steam at temperatures above 1100°F. (For example, in advanced gas cooled reactors, the stainless steel fuel cladding operates at 1472°F nominal with higher temperature hot spots, in a CO₂ environment.) It actually inhibits the internal corrosion of aluminum alloys. The extensive and expanding use of the carbon dioxide as a reactor coolant is providing a great body of experience which can be drawn on for materials compatibility. Such experience indicates that it causes little or no corrosion to the primary system.

3. CYCLE PERFORMANCE ANALYSIS

As indicated on a typical Mollier Type diagram (Figure 1), the (Feher) cycle operates entirely in the supercritical pressure regime. At all points in the cycle, the working fluid (i. e., CO₂) is a single phase substance.

A qualitative review of Figure 1 illustrates the unique characteristics of this thermodynamic cycle. At the cold end of the cycle (a-b) the supercritical CO₂ is a liquid and the pumping process is that of an incompressible fluid with a consequent low work input requirement. The low pump-to-turbine work ratio is reflected by considerable divergence of the constant pressure lines as they extend upward. Also, the dependency of this cycle upon efficient recuperation is represented by the high residual differential enthalpy in the turbine exhaust ($h_{e1} - h_a$) as contrasted to the much smaller turbine work differential ($h_d - h_{c1}$). Thus, without recuperation, such a cycle would deliver a relatively low efficiency. Conversely, with highly efficient recuperation the thermal input requirement ($h_d - h_{c1}$) is only slightly greater than the turbine work differential. Combining this with the low pump-to-turbine work ratio results in very high cycle efficiencies.

The effect of fluid properties upon potential recuperator performance can be inferred by noting in Figure 1 the sudden droop of the constant temperature lines as they penetrate the supercritical regime. The implication is that the low pressure turbine exhaust fluid (at P₁) has more enthalpy to dispose of than the high pressure pump outlet fluid (at P₂) can absorb even were an infinite surface recuperator (with zero driving temperature differential) applied to the system.

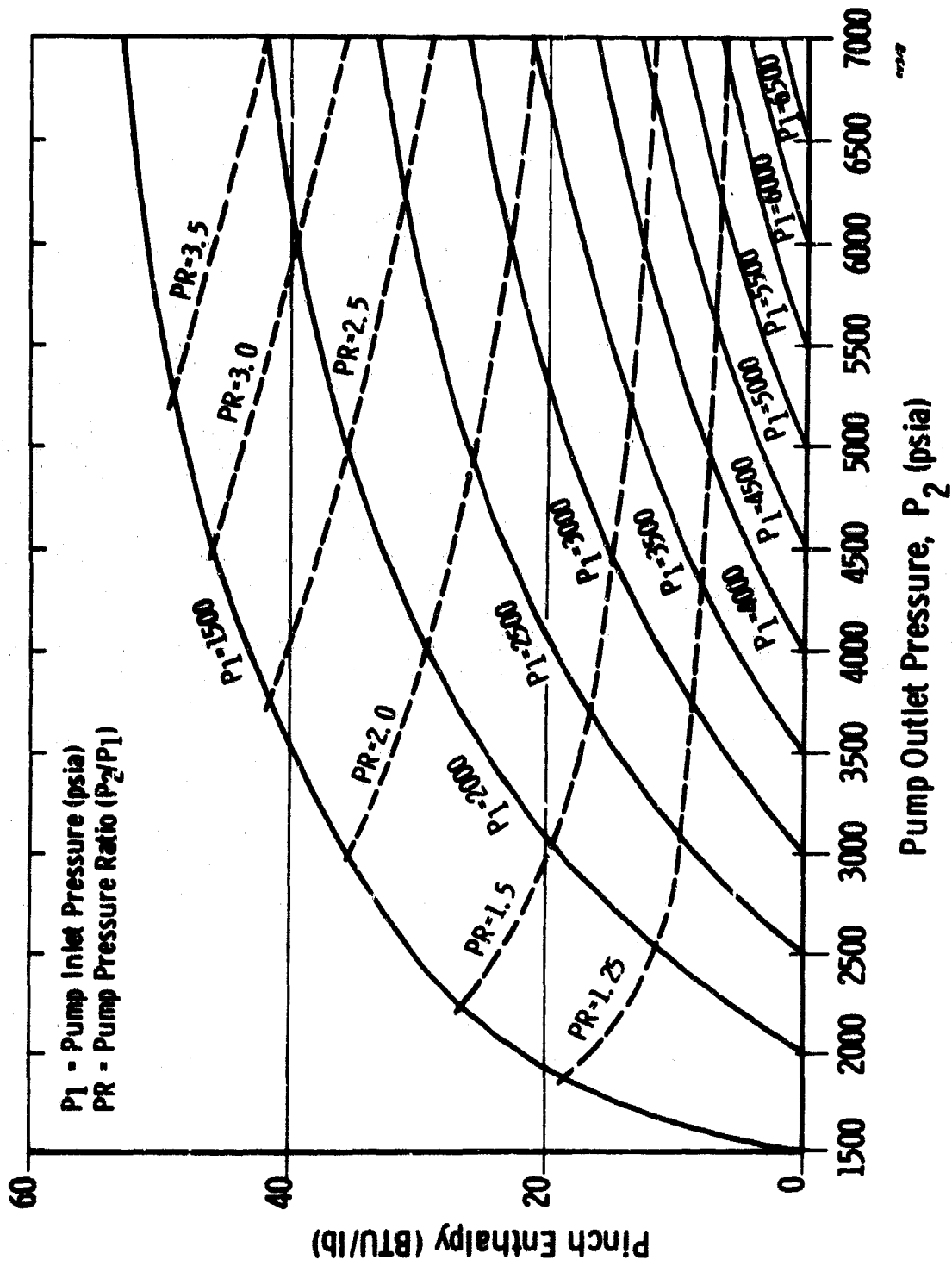


Figure 2. Recuperator Enthalpy vs Pump Outlet Pressure
 (Based on data of D. M. Newitt, et al. (Ref. 5))

This characteristically unrecoverable energy is referred to as the pinch enthalpy differential (δh_{pinch}). Quantitative values for CO_2 are given in Figure 2 for the range of pressures currently of interest.

In this cycle the cycle thermal efficiency may be described using three energy terms; namely pump work, turbine work, and unrecoverable turbine exhaust energy. The last of these three incorporates the two component quantities, δh_{pinch} and δh_{θ} , where δh_{θ} refers realistically to an additional increment of unrecoverable energy ascribed to a finite heat exchanger surface. The recuperator efficiency term (e_r) has been selected to describe real recuperator performance so that

$$(e_r) = \frac{\delta h_{\text{pinch}}}{\delta h_{\text{pinch}} + \delta h_{\theta}}$$

Thus, cycle thermal efficiency may be directly described by

$$\eta_{\text{cy}} = \frac{\text{Net Work}}{\text{Heat Input}} = \frac{\text{Turbine Work} - \text{Pump Work}}{\text{Turbine Work} + \delta h_{\text{pinch}} + \delta h_{\theta}} \quad (1)$$

In a simpler ratio form, this becomes:

$$\eta_{\text{cy}} = \frac{1.0 - \frac{\text{Pump Work}}{\text{Turbine Work}}}{1.0 + \frac{\delta h_{\text{pinch}}/e_r}{\text{Turbine Work}}} \quad (2)$$

Thus, the performance spectrum of the practical supercritical cycle can be predicted accurately by subjecting the energy terms included in equation (2) to a realistic degree of variation.

Reference 1 explains at length the nature of the aforementioned cycle variables and explores in considerable detail the effects on overall cycle performance of varying such parameters as

- a. turbine inlet temperature
- b. pump inlet temperature
- c. cycle pressure ratio
- d. turbine efficiency
- e. pump efficiency
- f. recuperator efficiency
- g. cycle characteristic pressure drop.

Turbine Inlet Temp. = 1300°F
 Pump Inlet Temp. = 68°F
 Pump Inlet Press. = 2000 psia
 Cycle Press. Drop = 0
 Recuperator Pinch Temp. = 8°F
 Working Fluid: CO₂

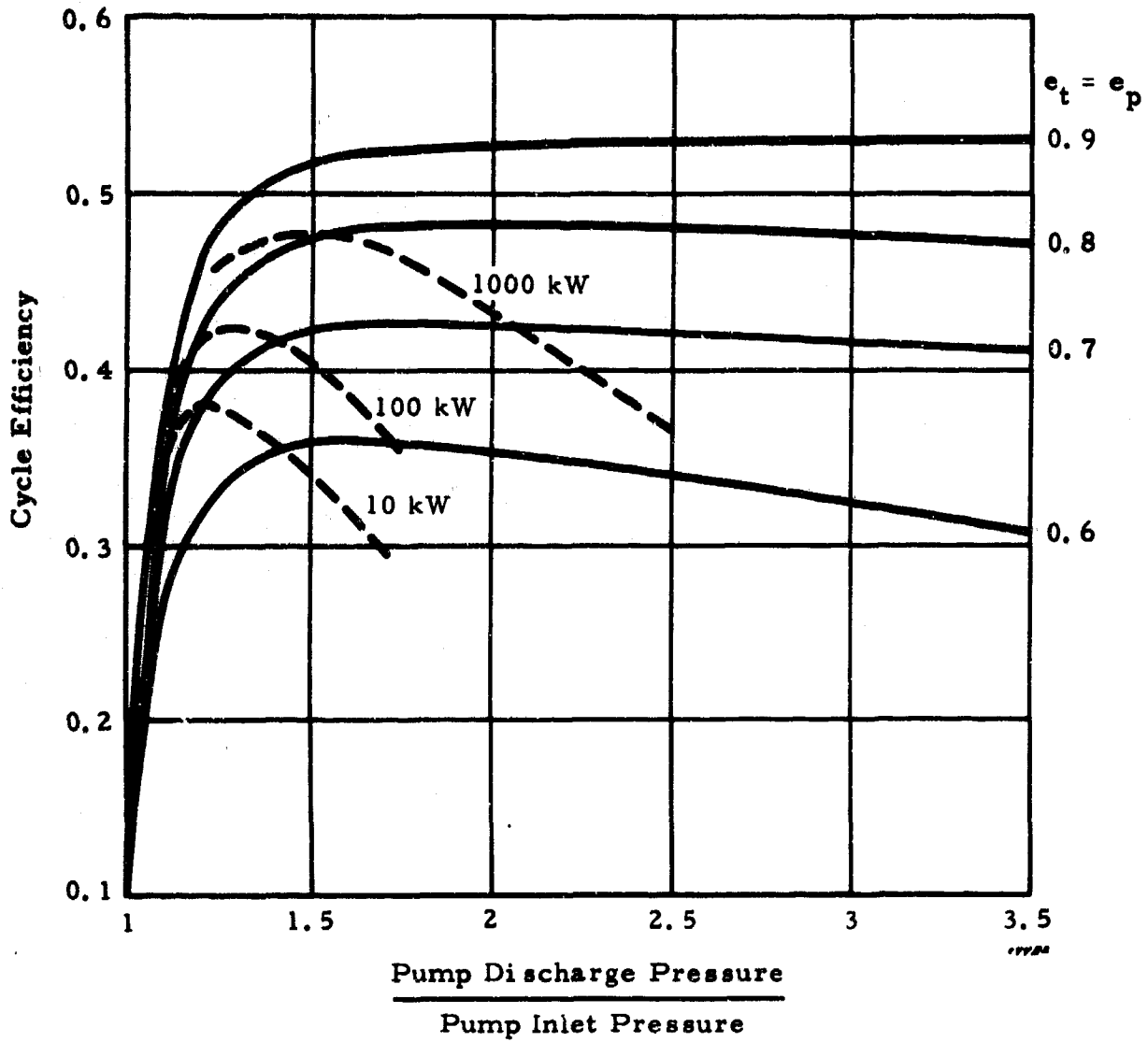


Figure 3. Cycle Efficiency as a Function of Pressure Ratio

4. CYCLE PERFORMANCE CONSIDERATIONS

The optimization of a supercritical CO₂ Power Conversion System (PCS) will be a function of the design power level, the turbomachinery rotational speed and the component efficiency as reflected by the degree of sophistication available in fabricating the turbo components.

The cycle itself has a characteristic performance trend as indicated in Figure 3. The solid curves represent the expansion of equation (2) for fixed values of turbine and pump efficiencies across a representative range of cycle pressure ratios. The resulting cycle efficiencies accurately represent the real performance which can be attained with a practical installation since all variables are accounted for in Figure 3 with the exception of cycle pressure drop. This term, however, can be compensated for simply by elevating turbine inlet temperature. Thus, at a pressure ratio of 1.50 for a cycle pressure drop of 25 psia for each side of the cycle, a turbine inlet temperature of 1400°F will show approximately the same cycle efficiency as Figure 3. For $\Delta P^*_{side} = 50$ psia, the turbine inlet temperature must be raised to around 1500°F to provide the same performance.

As in the case with all turbomachinery power cycles, decreasing power level design points are accompanied by decreasing flow rates, increased rotational speeds and ultimately, where mechanical design constraints limit speed, a degradation in component performance due either to low characteristic specific speeds or fabricational limitations imposed on miniaturized turbomachinery.

To demonstrate this effect, the performance for three different power levels, 1000 kW, 100 kW and 10 kW, have been superimposed on Figure 3 and are shown as dashed lines. In each case, a practical rotational speed was selected and a realistic component degradation factor was assumed, representing the current state-of-the-art.

Case A would represent the high power category where turbine dimensions, rotational speed and stage number are compatible with the best state-of-the-art efficiency throughout the entire pressure ratio range shown. Thus, for a fixed turbine efficiency, as pressure ratios increase, the turbine specific work increases, decreasing the denominator of equation (2), resulting in increasing cycle efficiencies.

Case B reflects the intermediate power category which implies reduced flow rates, smaller turbomachinery and a desire either to operate at higher rotational speeds or to increase the number of turbine stages. If the RPM and stage number are restricted by other system design constraints, increasing pressure ratio is accompanied by a decreasing specific speed below the best efficiency range and a subsequent degradation of turbomachinery performance occurs.

Case C shows the typical continuing cycle degradation as design power levels, flow rates, and turbomachinery dimensions are decreased even further.

Thus, it can be seen that maximum cycle performance occurs at some optimum pressure ratio which can be determined once the system design and component fabrication constraints have been established.

The problem of designing for the 10 kW power class is represented by Case C where maximum cycle performance will be achieved at pressure ratios of

$$1.20 < \frac{P_{\text{pump out}}}{P_{\text{pump in}}} < 1.30$$

and, as will be demonstrated later, at pump inlet pressures of

$$1850 \text{ psia} < P_{\text{pump in}} < 2100 \text{ psia}$$

If lower pressure ratios are applied, the turbine specific work decreases, increasing the relative magnitude of pinch enthalpy which, itself, increases with decreasing pressures. Additionally, for a real regenerative closed cycle, other parasitic losses begin to dominate, further depressing the cycle performance potential. This degradation is not adequately offset by the corresponding tendency for improved expander efficiencies at lower pressure ratios.

Conversely, although increasing pressures and pressure ratios improve the relative pinch enthalpy and parasitic loss factors, their degree of improvement lessens rapidly beyond the range indicated above while at the same time turbine performance and associated design criteria become successively less favorable.

Thus, for a selected low power level there is a relatively narrow range of pressures and pressure ratios that will deliver maximum performance in conjunction with acceptable component specifications.

SECTION III

CRU PRELIMINARY DESIGN

1. INITIAL CYCLE SELECTION

The study objective calls for a preliminary design (using current technology) of a test unit that will confirm the operational feasibility of the Feher cycle and establish component efficiencies at a level compatible with high cycle efficiency objectives.

It has been indicated above that for the 10 kWe power class optimum cycle performance occurs at turbine discharge pressures of around 2000 psia. For verification purposes, the cycles corresponding to three turbine exhaust pressures (1800 psia, 2000 psia, and 2200 psia) were investigated for each of three turbine pressure ratios, namely

$$P_d/P_e = 1.22, 1.25, \text{ and } 1.30.$$

These nine combinations are shown in Figure 4 indicating CRU design speed and cycle efficiency for each as a function of actual turbine efficiency and also of the characteristic half-cycle parasitic pressure drop. For each pressure ratio, the cross hatched central sector represents the 2000 psia pump inlet pressure with 1800 and 2200 psia bracketing on either side. It is apparent that for any practical RPM, the 2000 psia spectrum will result in cycle efficiencies comparable to or better than the other two.

The speeds shown represent the desirable design range for optimum cycle efficiency. To design to higher RPM would offer relatively small improvements in cycle efficiency while incurring uncertainties in producibility and mechanical performance.

Alternately, lower RPM would correspond to lower turbine pressure ratios, incurring a serious drop-off in cycle efficiency for systems reflecting realistic pressure losses.

From the analysis reflected by Figure 4 and a selected CRU design speed of 80,000 RPM (discussed further in the mechanical design section), the following design point was initially selected for the test unit.

Turbine inlet temperature	= 1440°F
Turbine inlet pressure	= 2460 psia
Turbine discharge pressure	= 2000 psia
CO ₂ mass flow rate	= 0.86#/sec
Rotational speed	= 80,000 RPM

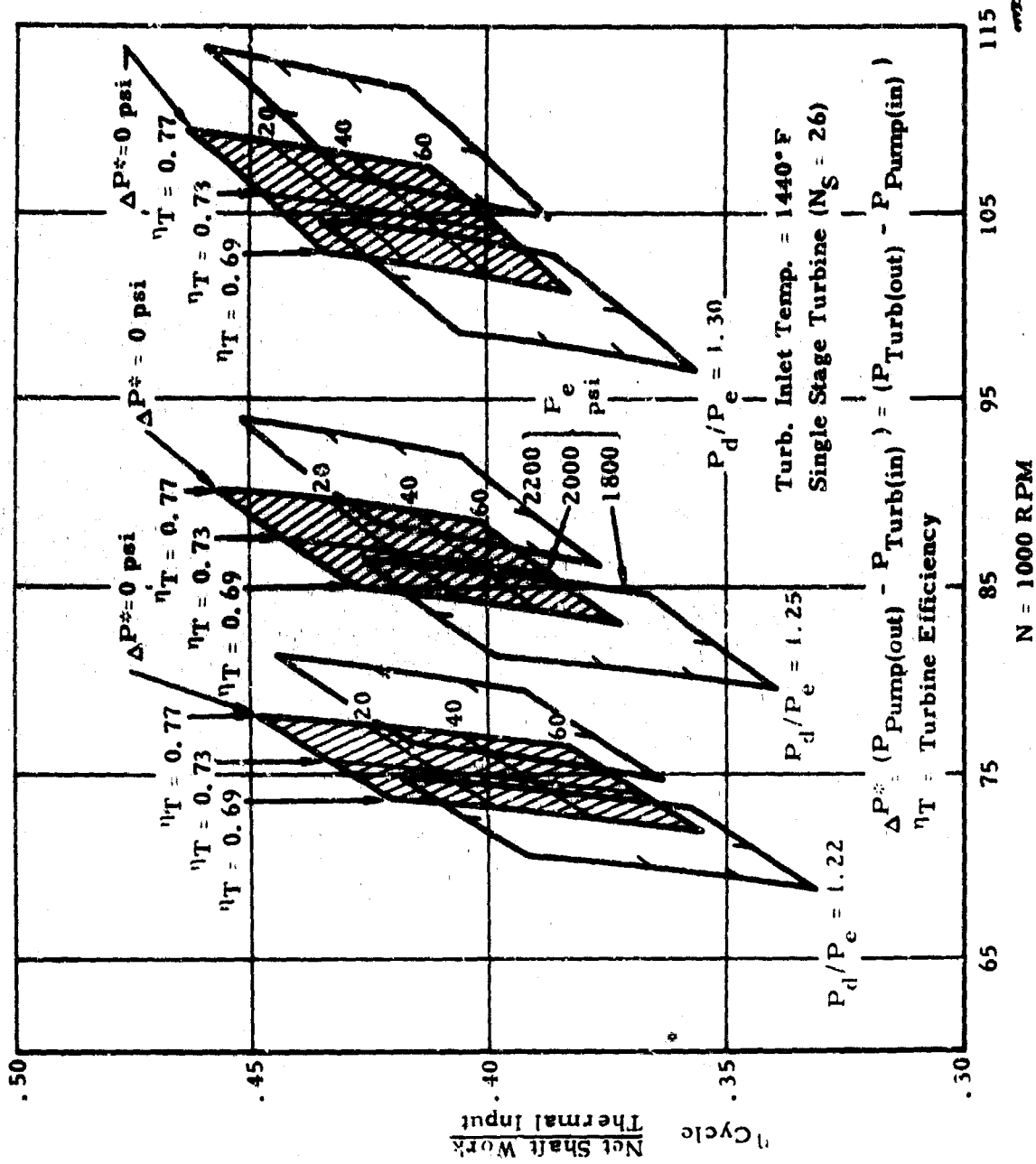


Figure 4. Feher Cycle Performance Spectrum at the 10 kW Power Level (Single Stage Turbine)

Pump inlet temperature	= 80°F
Pump inlet pressure	= 1960 psia
Pump discharge pressure	= 2500 psia

Table II describes approximate turbine and pump designs that conform to the design point selected.

2. TURBINE AND PUMP ANALYSIS

a. General Discussion

Comprehensive studies have been made on the characteristic values of turbomachines. The result of these studies is that only few significant parameters are needed to define the performance potential and the optimum geometry of turbine and pump designs. This results from (1) potential flow and boundary layer arguments which show that the cascade losses are a function of the Reynolds Number, Mach Number, solidity, aspect ratio, blade loading, and mean vector angle and from (2) similarity considerations which show that the above parameters are interrelated with the machine similarity parameters: specific speed N_s , specific diameter D_s , peripheral Mach number Ma^* , peripheral Reynolds Number Re^* and ratio of specific heats. Thus the maximum obtainable turbocomponent efficiency and the optimum design geometry can be computed as functions of the similarity parameters by numerically evaluating the pertinent interrelation until the optimum configuration has been found for given operating conditions. This leads to the calculation of design selection diagrams ($N_s - D_s$ diagrams) which show the maximum obtainable turbocomponent efficiency and significant geometrical ratios (representing the optimum geometry) for fixed values of the peripheral Reynolds Number, peripheral Mach Number and ratio of specific heats. A typical diagram is shown in Figure 5 for turbines. It is important to realize that every point on this diagram is a design point. Similar design selection diagrams can be computed for pumps.

Actually, the specific speed and specific diameter parameters are the most important for the stage efficiency. The influence of the other parameters, Mach Number and Reynolds Number, is comparatively small as long as the chord Reynolds Number is above the critical value, and as long as the flow velocities do not exceed the velocity of sound. Lower efficiencies than quoted in Figure 5 are to be expected when the Reynolds Number is smaller than the critical Reynolds Number. The Mach Number influence on turbine performance usually is very small, it does, however, affect the optimum geometry to some degree. The similarity parameter, ratio of specific heats, which also does not affect the maximum obtainable stage efficiency significantly, will however, have an influence on the optimum geometry.

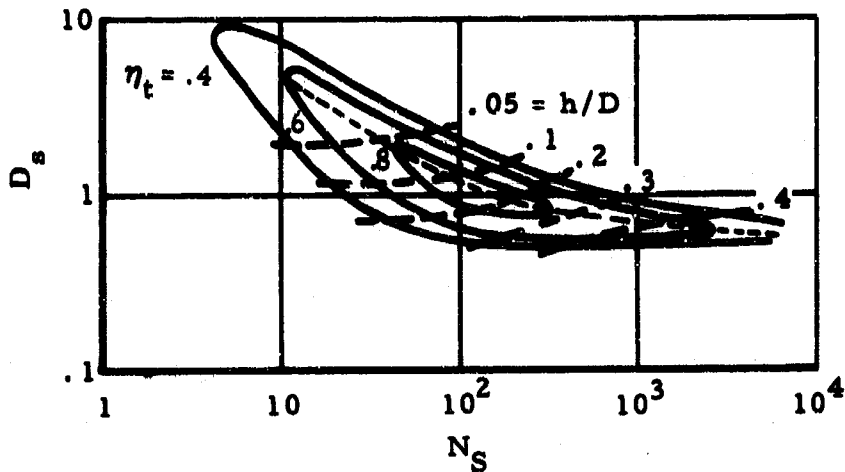
Other assumptions for the selection diagrams are that the blade surfaces be hydraulically smooth, that the trailing edge thickness of the rotor and stator blades be smaller than 2% of the blade pitch, and that the tip clearance between rotor and stator be no more than 2% of the blade height.

TABLE II. INITIAL SELECTION OF TURBINE AND PUMP CHARACTERISTICS

Component	Specific Speed	Approximate Diameter (inches)	Component Efficiency		Best State of Art Prediction (η_{max})
			($\eta/\eta_{max} = 0.90$)	($\eta/\eta_{max} = 0.95$)	
Turbine	$N_{ST} = 26$	1.2	0.69	0.73	0.77
Pump	$N_{SP} = 43.6$	1.0	0.73	0.77	0.81
η_{cycle} :			0.37	0.39	0.41

$$R_e^* > 2 \times 10^6, M_a^* < 1.2 \quad S/h = .02, t_e/t = .02$$

$$r = 1.4$$



$$N_s = \frac{N \sqrt{V}}{H_{ad}^{3/4}}$$

$$M_a^* = \frac{U}{C_s}$$

$$D_s = \frac{D H_{ad}^{1/4}}{\sqrt{V}}$$

$$R_e^* = \frac{D U}{\theta}$$

N Rotative Speed (RPM)

h Blade Height

D Rotor Diameter (Ft)

S Tip Clearance

H_{ad} Adiabatic Head (Ft)

t Blade Pitch

V Volume Flow Rate (Ft³/Sec)

t_e Trailing Edge Thickness

U Tip Speed

C_s Velocity of Sound

θ Kinematic Viscosity

r Ratio of Specific Heats

44527

Figure 5. Typical N_s , D_s Diagram For Turbines

The specific speed and specific diameter parameters are defined in such a manner that they directly reflect the turbo component design requirements such as the adiabatic head, the flow rate, the rotative speed and the rotor diameter. These diagrams are applied to the preliminary design of turbo components by determining the specific speed for the desired operating conditions and by selecting from the N_s , D_s diagrams the maximum obtainable stage efficiency. This value is obtained at the optimum specific diameter (identified in Figure 5 by a dotted line) which then represents the desired rotor diameter D . This value would be selected for the design in cases where the application of this diameter does not cause excessive tip speeds (from a stress point of view). At the same time, the associated h/D value is found so that then the blade height h is determined which then indicates the maximum allowable tip clearance.

In cases where excessive tip speeds are not anticipated (nonstress-limited designs) only the efficiency obtainable at the optimum specific diameter is of interest. Thus, the information presented in typical N_s , D_s diagrams can be condensed to simplified plots that show the maximum efficiency (at the optimum specific diameter) as a function of specific speed. Figure 6, calculated for turbines, shows that up to specific speeds of 13, partial admission turbines give highest efficiencies, whereas for specific speeds higher than 13, full admission designs should be considered. The maximum obtainable efficiency, in general, decreases with decreasing specific speeds. Impulse type rotor blading is assumed for $N_s < 50$. The optimum specific diameter and the ratio of blade height to diameter is shown in Figure 7, indicating decreasing optimum specific diameters with increasing specific speeds. Examining now the optimum ratio of blade height to diameter, it is found that this ratio increases in general with increasing specific speeds, reaching values of .07 at specific speeds of 13 for partial admission turbines but having values of .02 for full admission turbines operating at the same specific speed.

Figure 8 presents similar information for pumps and shows that for low specific speeds (up to $N_s = 10.5$) Pitot pumps give best efficiencies. For specific speeds from 10.5 to 22 partial emission designs give highest efficiencies, whereas for even higher specific speeds, full emission centrifugal pump designs offer the highest efficiency potential. The maximum obtainable pump efficiency generally decreases with decreasing specific speeds. The associated rotor diameter ratio and exit blade width are shown in Figure 9 indicating similar trends as discussed for turbines, namely decreasing specific diameters with increasing specific speeds.

The information shown in Figures 6 and 7 can also be applied for calculating the maximum performance potential of multistaged turbines. The procedure is to assume a head split between the stages, calculate the stage specific speed on this basis, and to find the maximum efficiency and optimum geometry from the stage performance diagram. The head split is then varied until the maximum overall efficiency is found.

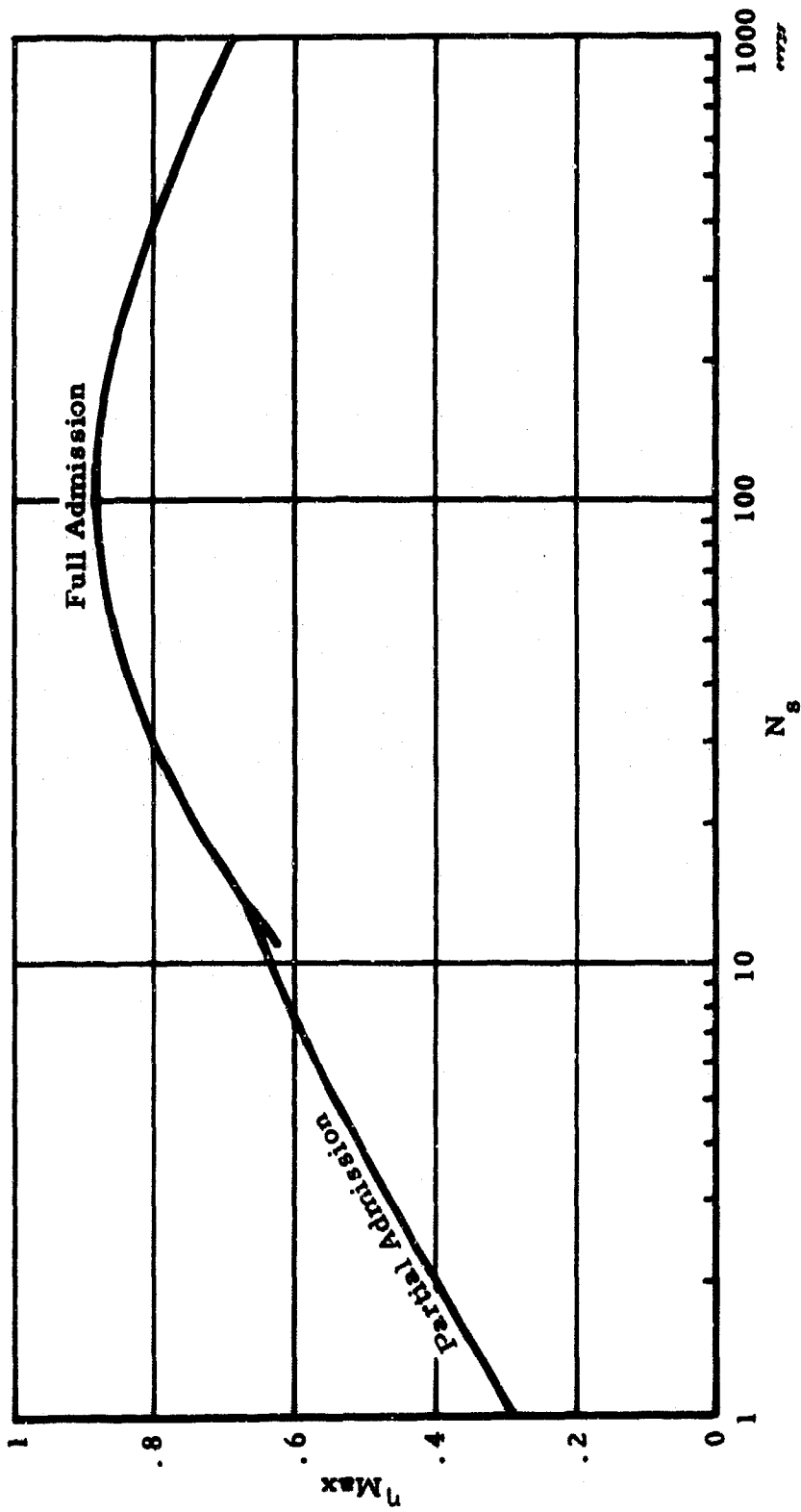


Figure 6. Simplified Diagram for Turbines
Maximum Efficiency - N_s

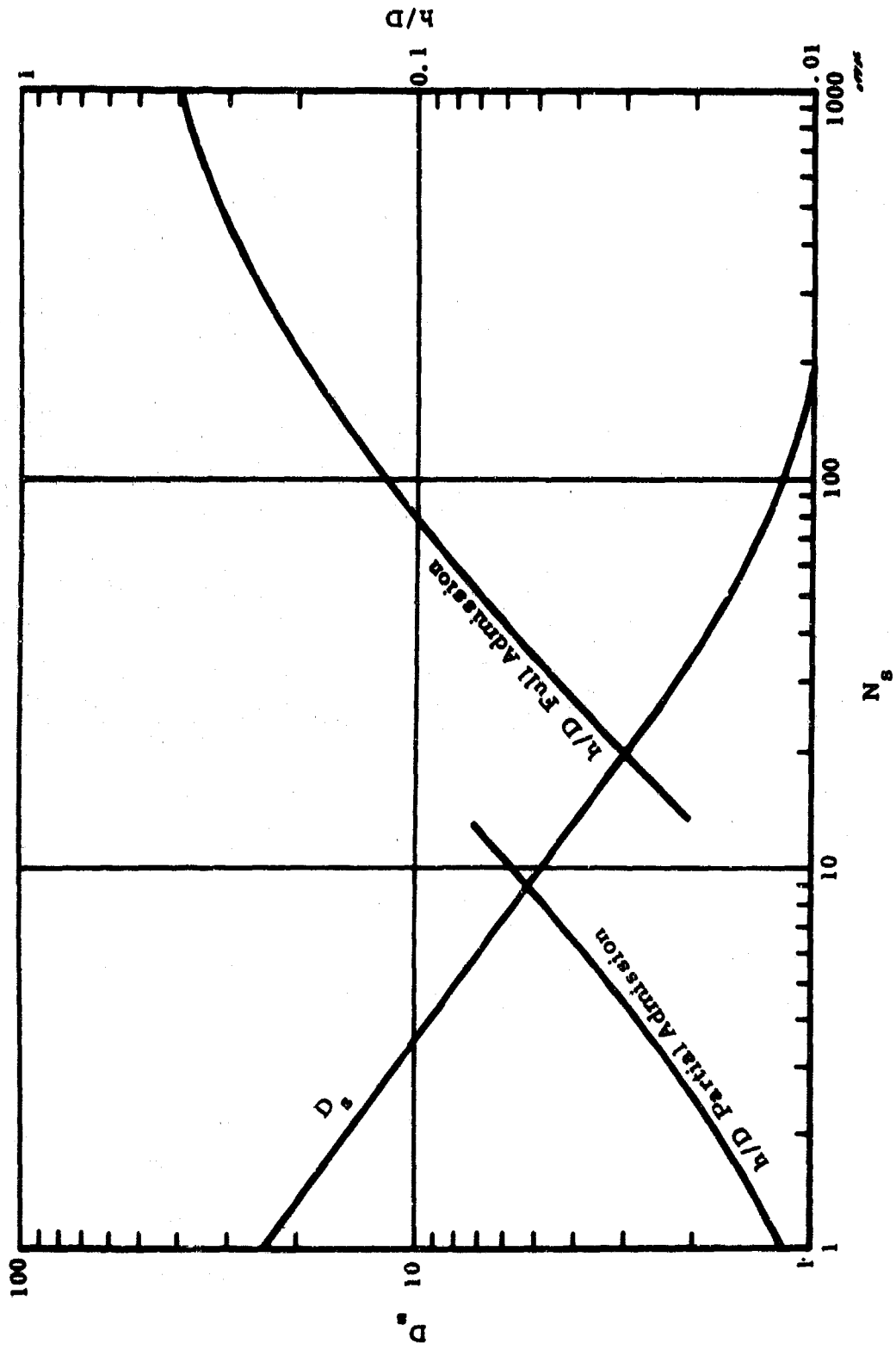


Figure 7. Optimum Turbine Geometry

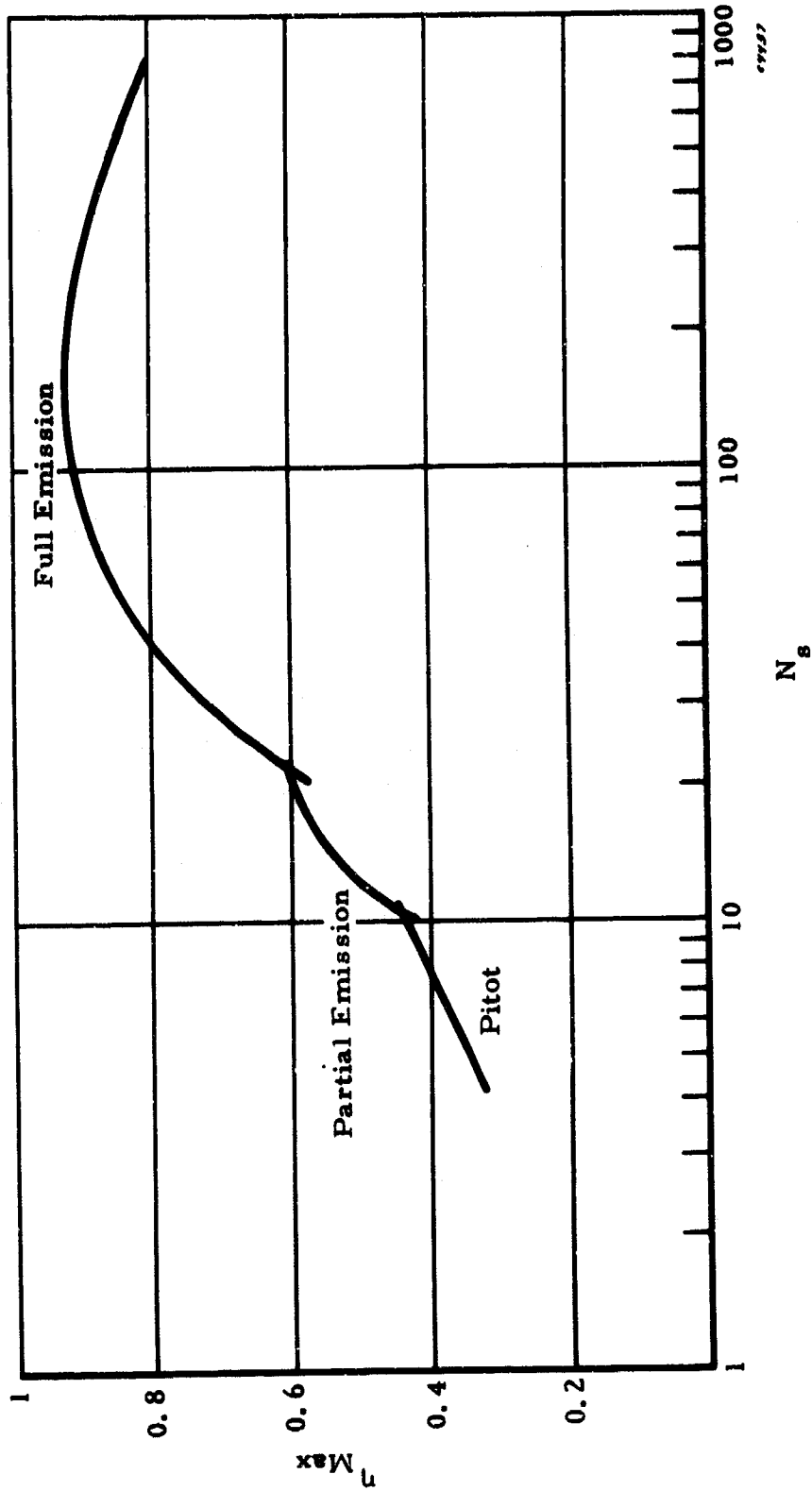


Figure 8. Simplified Diagram for Pumps
Maximum Efficiency - N_s

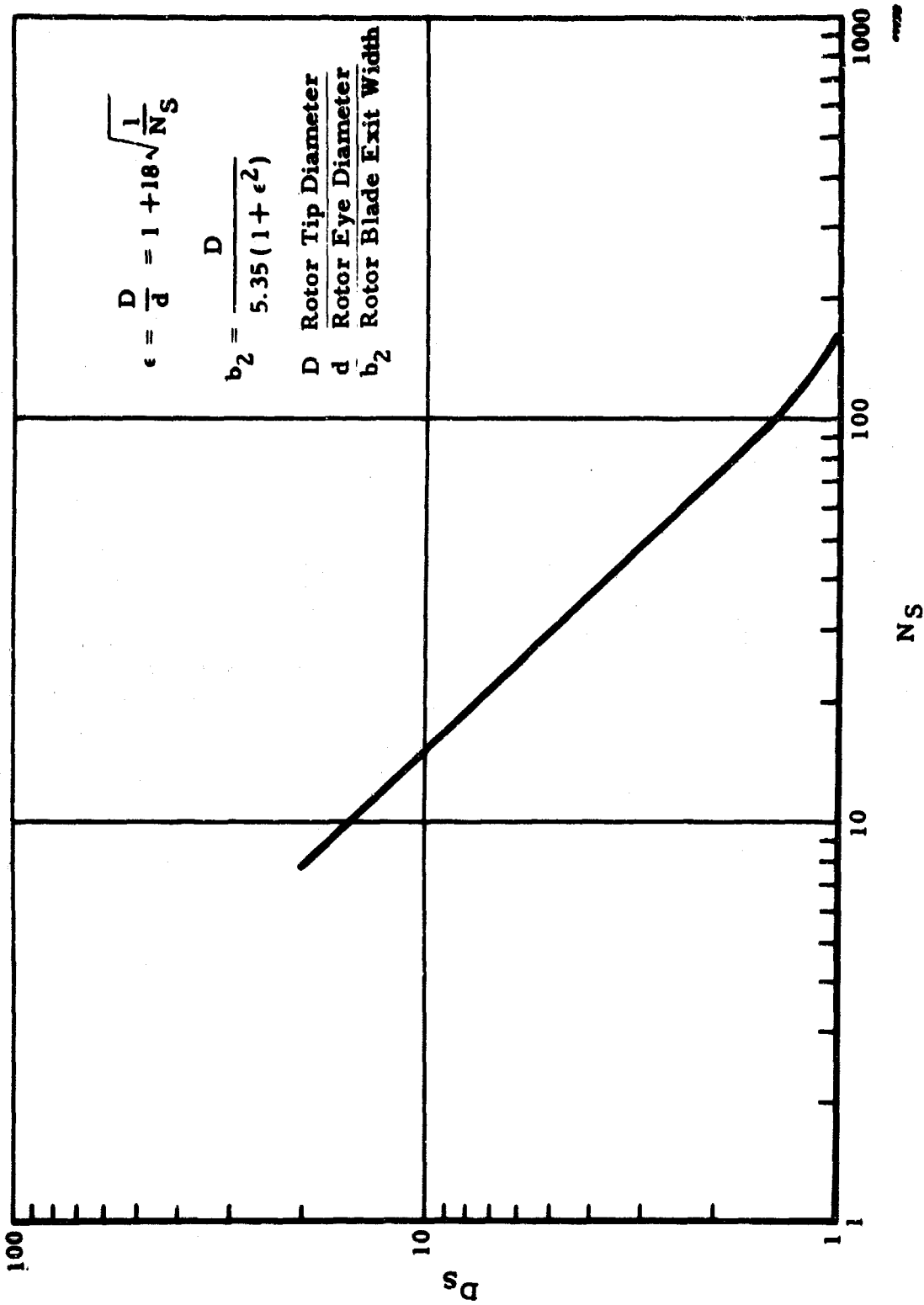


Figure 9. Optimum Pump Geometry

b. Configuration and Performance Analysis
Using Design Point Data

The generalized studies were based on the selection of axial impulse turbines as near optimum designs. Actually, an impulse design is also favored by mechanical design considerations since, in this operating mode, the pressure difference across the turbine disc is small so that the resultant axial thrust is small. By selecting double shrouded rotor designs for the pump component, the axial thrust on the pump side would also be small. Thus, the load carrying capacity of the axial thrust bearing can be kept low so that high power losses are avoided. Detailed aerodynamic considerations, however, would indicate that reaction turbines may offer a higher efficiency potential than impulse turbines.

In order to determine the validity of this argument, the degree of reaction was changed step-wise and the desired geometry and efficiency potential was calculated. The results are shown in Figures 10 and 11, by plotting the rotor diameter D , the chord lengths C and the blade height h as functions of the degree of reaction ρ in Figure 10, and by showing the optimum rotor blade number Z_R , nozzle blade number Z_N , rotor blade inlet angle β_2 and rotor blade exit angle β_3 as functions of the degree of reaction in Figure 11. Increasing rotor diameters, increasing chord lengths and blade height together with increasing number of nozzle blades result from increasing degrees of reaction. The rotor blade inlet and exit angles, however, decrease together with the optimum rotor blade number with increasing degrees of reaction. This also means that the rotor flow deflection decreases with increasing degrees of reaction. The exit swirl angle α_3 increases with increasing degrees of reaction, meaning that high degrees of counter swirls occur at low degrees of reaction.

Figure 12 shows the axial thrust load across the turbine disc as a function of degree of reaction and Figure 13 shows the desired trailing edge thickness of the nozzle and rotor. Comparatively low values for the axial thrust occur at impulse operation, but extremely high axial thrust loads (up to about 500 pounds) are calculated for 50% reaction turbines. The desired trailing edge thickness, in all cases, is comparatively small, namely .00035 inch for 50% reaction designs, and even smaller for impulse designs. The absolute leaving energy from the turbine rotor expressed by the square of the ratio of leaving velocity to spouting velocity $(c_3/c_0)^2$ decreases with increasing degrees of reaction, meaning that exhaust diffusers are important for low reaction designs, but of little significance for high reaction designs.

It is apparent from these figures that high reaction turbines have larger dimensions, i. e. also larger blade heights and thus fewer manufacturing problems than impulse turbines. At the same time, high degrees of reaction offer, in general, a higher efficiency potential than impulse turbines. However, the required thrust bearing capacity will be comparatively high for this turbine type, so that considerations dealing with the power loss in axial thrust bearings will tend to favor low reaction designs.

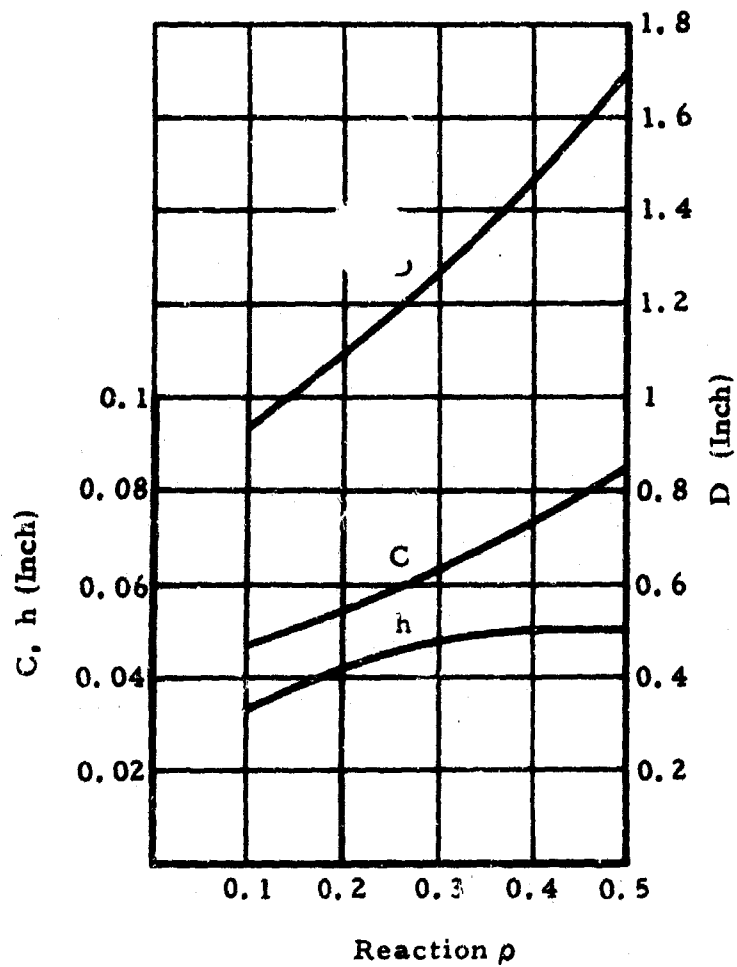


Figure 10. Turbine Diameter, Blade Chord and Blade Height as a Function of Degree of Reaction

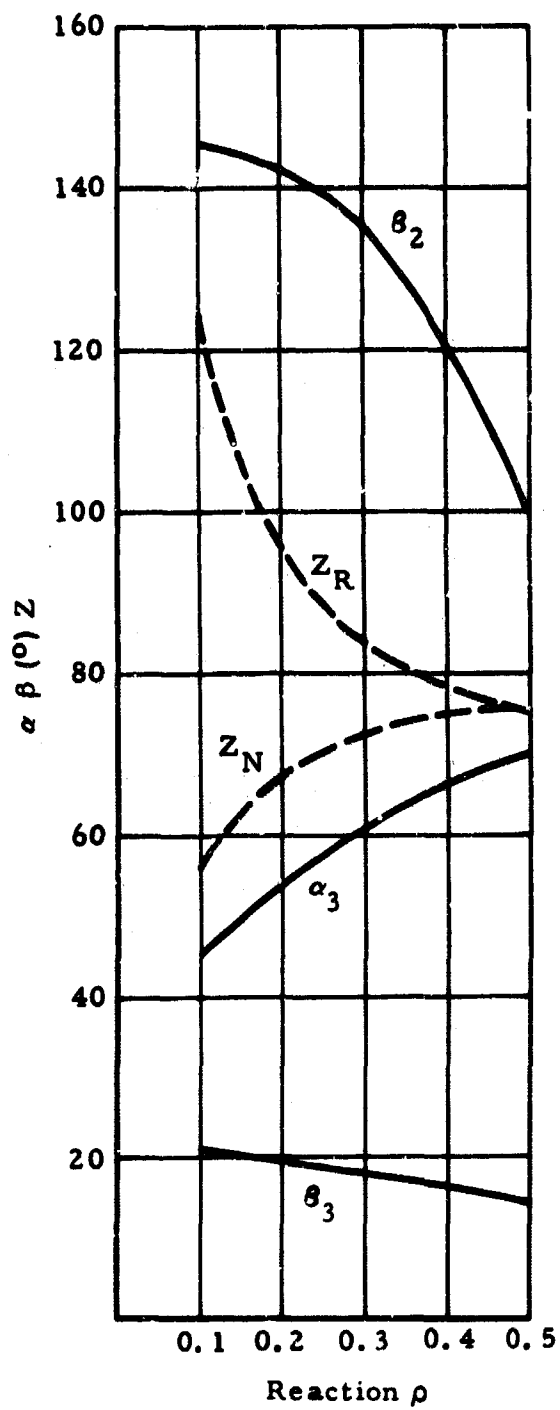


Figure 11. Turbine Blade Angle and Blade Number as a Function of Degree of Reaction

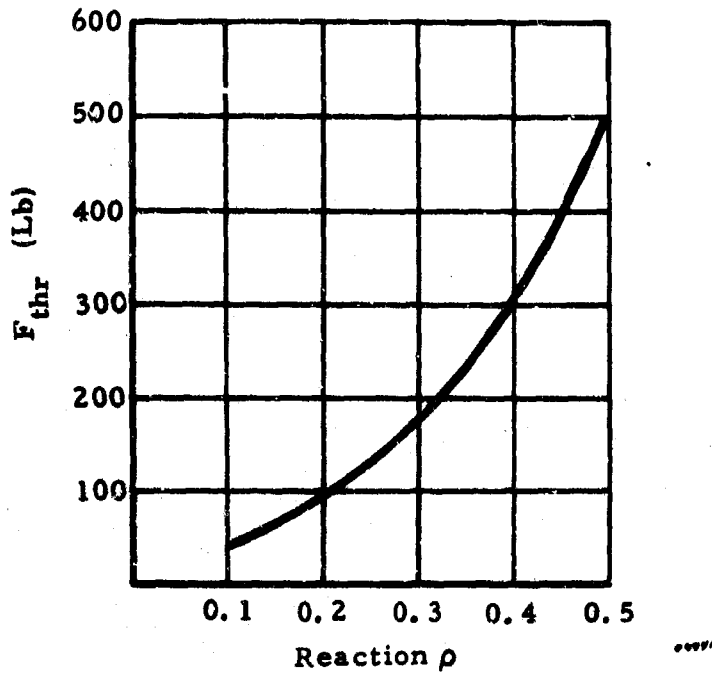


Figure 12. Turbine Thrust as a Function of Degree of Reaction

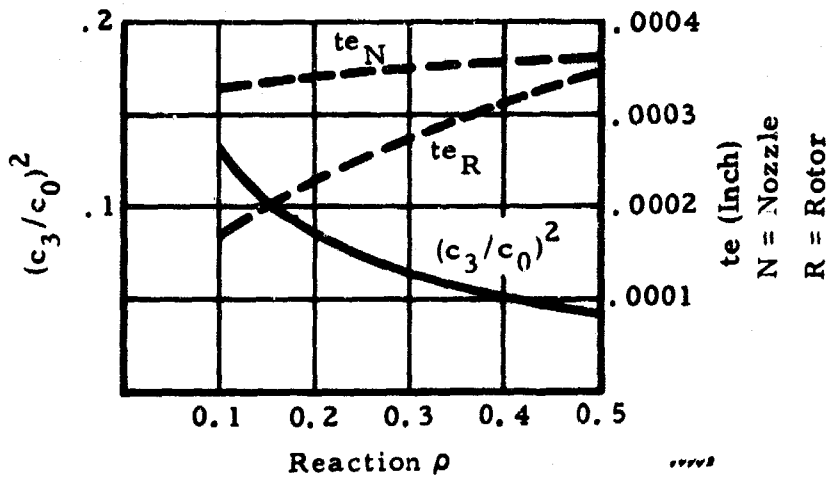


Figure 13. Trailing Edge Thickness and Exit Velocity Loss as a Function of Degree of Reaction

The small trailing edge thickness desired for low as well as high reaction turbines, will be difficult to maintain during turbine operation. The effect of the trailing edge thickness on turbine performance is particularly strong for the optimum chord length shown in Figure 14a. The efficiency drops drastically with increasing trailing edge thickness, for example, from 70% to 57% for designs with 10% degree of reaction, when the originally assumed trailing edge thickness of 0.0007" is increased to .002". A similar drop in efficiency occurs for 50% reaction turbines. Since the efficiency level of 50% reaction turbines is considerably higher than that of impulse turbines, a trailing edge thickness penalty can more readily be accepted for the 50% reaction design. This diagram also shows the influence of the tip clearance indicating a comparatively high sensitivity of the 50% reaction design to tip clearance, and a smaller sensitivity to tip clearance for the impulse type design.

The turbine efficiency sensitivity to trailing edge thickness can be modified when the chord length is increased to values above the original (optimum) chord lengths. Selecting higher than optimum values for the chord length means that fewer blades will be required when the optimum solidity is retained. Since the trailing edge penalty is a function of the ratio of trailing edge thickness to pitch, larger chord lengths, i. e. smaller blade numbers, become more tolerant to trailing edge thickness. The maximum efficiency potential, however, is reduced since larger chord lengths mean higher end-wall losses and consequently lower efficiencies. These trends are shown on Figure 14b. The maximum efficiency level obtainable with this design version is smaller than the design with the original chord length. The efficiency obtainable with a trailing thickness of .002 inch, however, is higher for the increased chord length than for the original chord length.

All data presented so far assumed a hydraulically smooth surface. The effect of surface roughness on performance is shown in Figure 15 for a design with the original chord lengths as well as with extended chord lengths. Assuming a trailing edge thickness and tip clearance of .002 inch, a surface roughness effect can be expected in cases where the surface roughness is larger than 16 micro-inches. For a surface finish of 32 micro-inches, only very little performance loss is calculated. More significant efficiency penalties will occur, however, if the surface roughness is larger than 32 micro-inches.

c. Turbine Design Point Selection

It is apparent that to maximize turbine efficiency, the designer must accommodate the highest degree of reaction that can be accepted with confidence.

Figure 14 also shows that the optimum chord length (C_0) is an optimum only where extremely thin trailing edges can be maintained. As the trailing edge thickness (t_e) increases, the shorter chord ($C = C_0$) degrades far more rapidly than the longer chord ($C = 3C_0$) and at $t_e = .002$, the long chord blade is more efficient than the short chord.

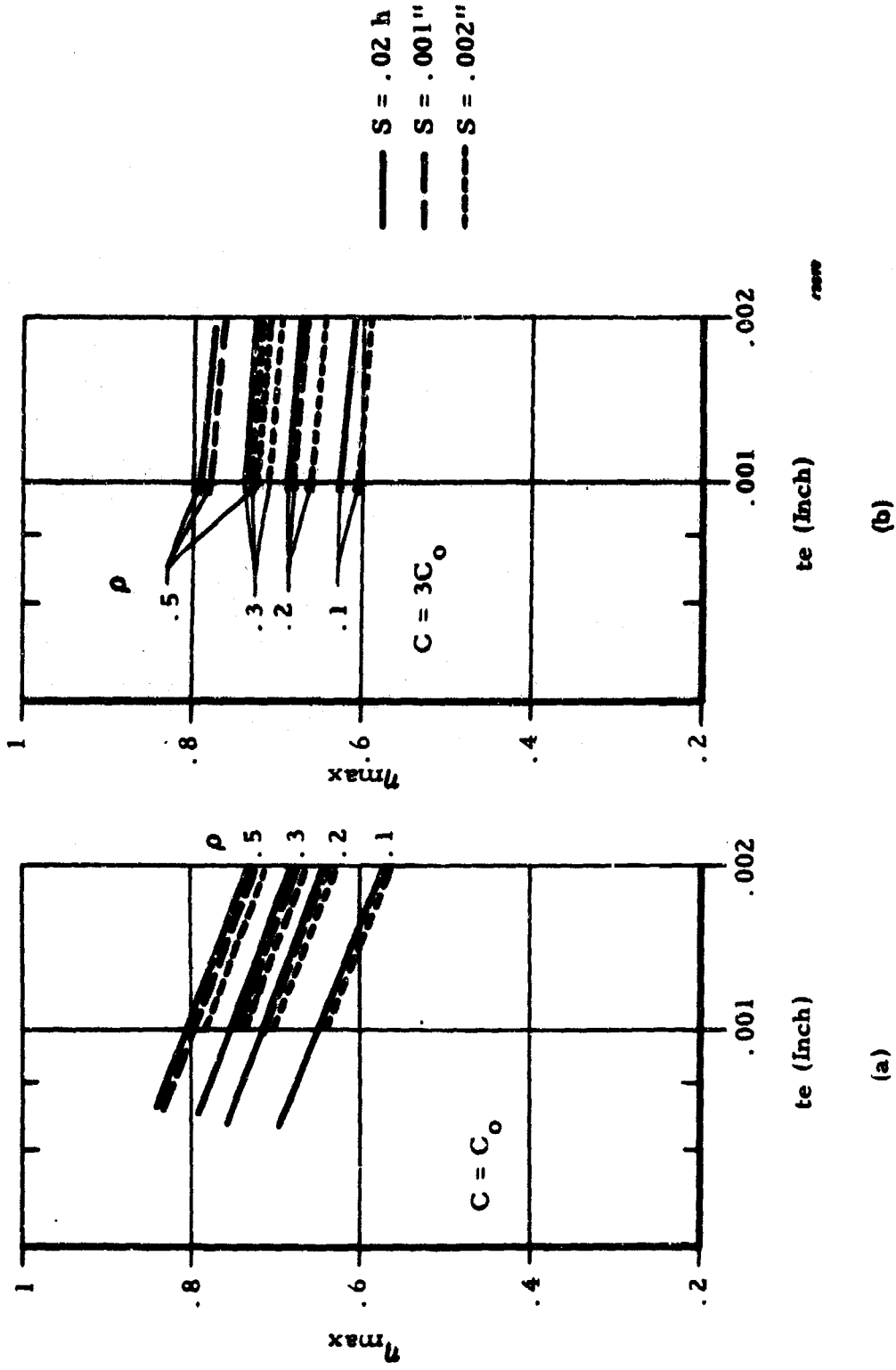


Figure 14. Turbine Efficiency as a Function of Blade Trailing Edge Thickness and Chord Ratio, Assuming Hydraulically Smooth Surface

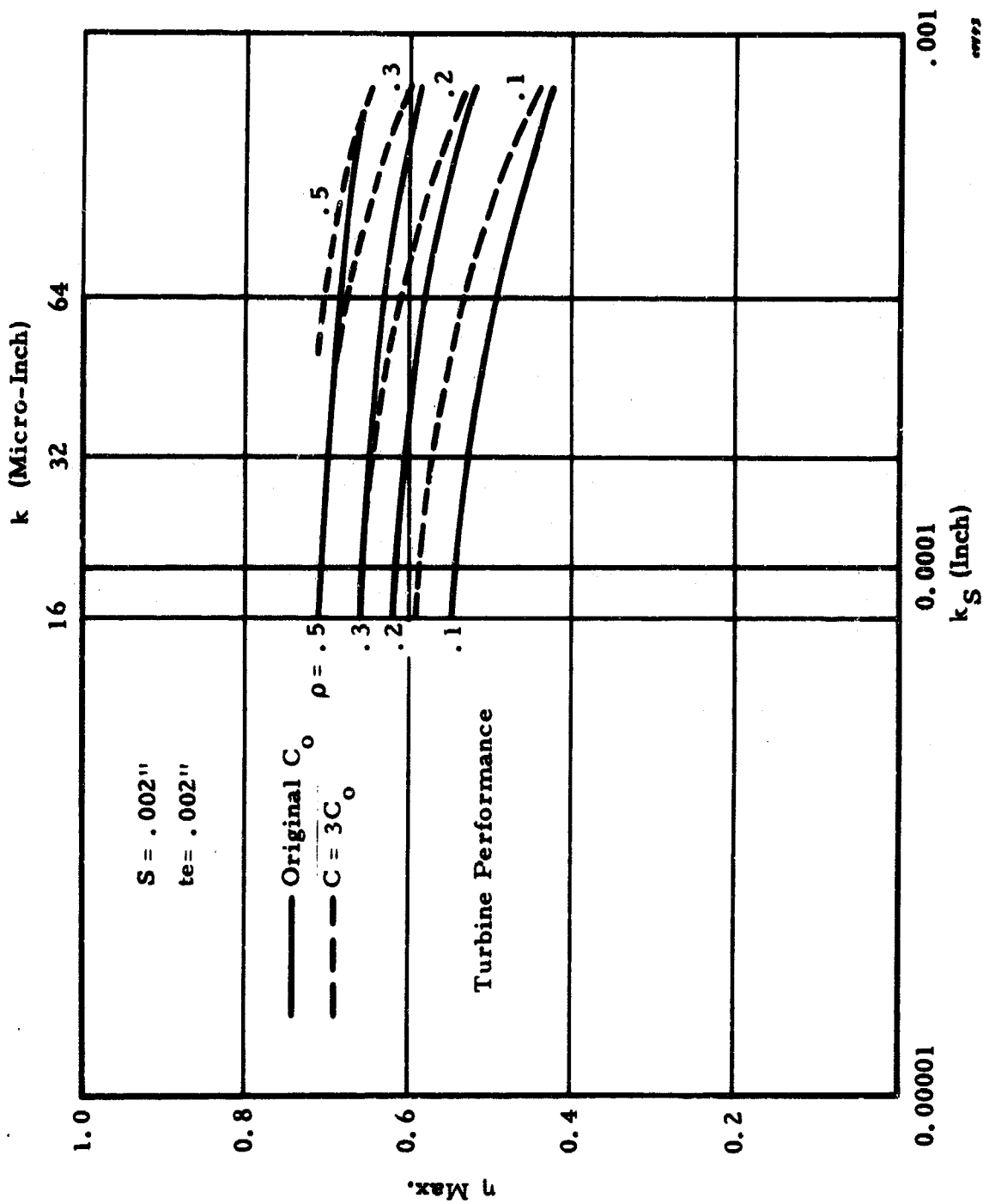


Figure 15. Turbine Efficiency as a Function of Blade Surface Roughness

Noting also from Figure 11 that the high degree of reaction results in the smallest turbine exit angle and (for $C = C_0$) a relatively high blade number ($Z_R \sim 75$), the combination of high blade number, low exit angle and very thin trailing edge presents a difficult configuration to fabricate.

Thus, the real optimization of turbine performance can be assessed only after sufficient fabricating experience has been acquired to predict with confidence the maximum number of blades, the smallest exit angle and the thinnest trailing edge that can be consistently reproduced.

These three criteria can then be reintroduced into the component loss analysis to determine specifically the corresponding chord length and blade profile that will provide a maximum turbine efficiency.

For the initial design point, the first turbine design selected for fabrication studies had the basic specifications shown in Table III.

TABLE III. FIRST TURBINE DESIGN

Degree of reaction	.30
Blade number: nozzle	36
rotor	42
Chord length	.110 inch
Surface roughness	16-32 μ inch
Tip clearance	.001 inch
Trailing edge thickness	.001 inch
Blade height	.048 inch

d. Pump Performance Considerations

The pump impeller fabrication problems are similar to those described for the turbine but perhaps less due to the reduced blade number. The same manufacturing techniques may be applied with a high degree of confidence that a satisfactory impeller can be fabricated.

The pump tip speed is relatively low (slightly over 300 ft per second) permitting a double shrouded impeller having a predictable hydraulic efficiency of $\eta_{\text{impeller}} \approx 0.90$.

The overall pump efficiency will be sensitive to impeller blade accuracies, rotor and stator alignment, the recirculating leakage, and performance of the vaned diffuser. Optimum performance will necessitate attention to all these areas. A preliminary estimate of pump performance indicates overall efficiency range for the test component of

$$0.66 < \eta_{\text{pump}} < 0.70$$

e. Final Design Point Selection and Pump Calculation

Following preliminary investigation of the fabrication problems with specialists in the art (covered in detail later) the specifications of the First Turbine Design were reexamined. It was decided that to increase the probability of meeting the component efficiency targets as reflected in Table II, the turbine and pump specific speeds will be increased. This was done by reducing the pressure ratio, therefore increasing the mass flow, while retaining the design speed of 80,000 RPM (see Table IV). Although this results in slightly lower cycle efficiency, the margin between the best prediction and expected performance increases as can be seen by comparing Tables II and V.

Specifications of the Final Turbine Design are shown in Table VI.

Having established the turbine specifications those of the pump were calculated and are given in Table VII.

3. BEARINGS

The use of high-pressure CO₂ as a bearing fluid presents several interesting and rather unique circumstances. The high-pressure CO₂ bearing cannot be considered a gas bearing because the fluid is decidedly incompressible, in the hydrodynamic theory sense of compressibility. This differentiation has several important ramifications, but perhaps the most significant is that the load-carrying capacity of an incompressible-fluid, self-acting bearing increases sharply as the average film thickness is reduced, whereas compressibility in the fluid acts quickly to limit the bearing load-carrying capacity as the average film thickness is reduced. This effect will be demonstrated by computing the load-carrying capacity of a typical standard air gas bearing for various values of the average film thickness. The computation will extend over both the compressible and incompressible regimes so that the point of departure from incompressible theory will be evident.

For the example assume a 360° continuous film bearing as follows:

- angular shaft speed (ω) = 9250 rad/sec
- fluid viscosity (μ) = 2.7×10^{-9} reyns
- shaft radius to radial clearance ratio (R/C) = 100
- fluid bulk modulus (β) = 15 psi
- bearing length to diameter ratio (L/D) = 1

For these conditions, the compressibility factor, Λ , is as follows:

$$\Lambda = \frac{6\mu\omega}{\beta} \left(\frac{R}{C}\right)^2 = \frac{6(2.7 \times 10^{-9})(9250)}{15} (100)^2 = .10$$

Using the load carrying coefficients from Elrod and Malanoski (Ref. 7) for an

TABLE IV. FINAL TEST UNIT DESIGN POINT

Turbine inlet temperature	1440°F
Turbine inlet pressure	2200 psia
Turbine discharge pressure	1850 psia
CO ₂ mass flow rate	1.064 #/sec
Rotational speed	80,000 RPM
Pump inlet temperature	80°F
Pump inlet pressure	1825 psia
Pump discharge pressure	2225

TABLE V. GENERAL COMPONENT SPECIFICATION

Component	Specific Speed	Diameter (inches)	Component Efficiency	
			Expected Test Performance	Best State of Art Prediction
Turbine	34.0	1.20	0.72 - 0.73	0.82
Pump	60.5	0.76	0.66 - 0.70	0.86

TABLE VI. FINAL TURBINE SPECIFICATIONS

Degree of reaction	0.30
Blade number: nozzle	30
rotor	38
Chord length	0.106
Surface roughness	16-32 μinch
Tip clearance	0.001 inches
Trailing edge thickness	0.002 inches
Blade height	0.055 inches

TABLE VII. PUMP SPECIFICATIONS

Degree of reaction	0.60
Number of vanes: rotor	13
diffuser	15
Impeller blade:	
Inlet diameter	0.42
Inlet vane height	0.043 inches
Inlet vane angle	20.5°
Discharge diameter	0.76 inches
Discharge vane height	0.023 inches
Discharge vane angle	50°
Discharge trailing edge thickness	0.002 - 0.004 inches
Diffuser blade:	
Inlet diameter	0.95 inches
Inlet vane angle	17°
Discharge diameter	1.33 inches
Discharge vane angle	40°
Discharge trailing edge thickness	0.002 - 0.004 inches

operating eccentricity of 0.6, the bearing load carrying capacity per square inch of bearing projected area, P' , is found to be 0.48 lbs per square inch.

If (R/C) is now increased, the load carrying capacity also increases as shown in Table VIII. These results are shown graphically in Figure 16. The divergence between incompressible and compressible theories is seen to occur at an R/C ratio value of approximately 450, corresponding to a compressibility factor of about 2.0.

The bulk modulus of the supercritical CO_2 is extremely high. Defining the bulk modulus as

$$\beta = P \left(\frac{\partial P}{\partial \rho} \right)_T$$

where ρ = fluid mass density
 P = fluid pressure, and
 $()_T$ denotes differentiation at constant temperature

the CO_2 bulk modulus at 2000 psi and 100°F is approximately 6200 psi. This high bulk modulus value almost assures that the supercritical CO_2 bearing will operate well within the incompressible regime. To illustrate, at 2000 psi and 100°F , the viscosity of CO_2 is 6.9×10^{-9} reyns. If the bearing operates at 8370 rad/sec (80,000 rpm) with an R/C ratio of a relatively high 1250, the compressibility factor calculates to be

$$A = \frac{6\mu\omega}{\beta} (R/C)^2 = \frac{6(6.9 \times 10^{-9})(8370)}{6200} (1250)^2 = .088$$

This indicates quite clearly that incompressible theory would definitely be applicable. The ability of the supercritical CO_2 bearing to exploit this feature would depend of course on its being able to operate with relatively high values of R/C . The usual design restriction on R/C is that viscous shear losses in the bearing increase in approximately inverse proportion to the average film thickness so that high values of R/C tend toward high viscous shear losses. However, the viscous shear losses are also directly proportional to the fluid viscosity so that low viscosity tends toward low viscous shear losses. The viscosity of supercritical CO_2 in relation to other familiar fluids is given in Table IX.

In the discussion of the actual bearing geometry selection, it will be shown that R/C values above 1000 appear to be reasonable for the supercritical CO_2 bearing.

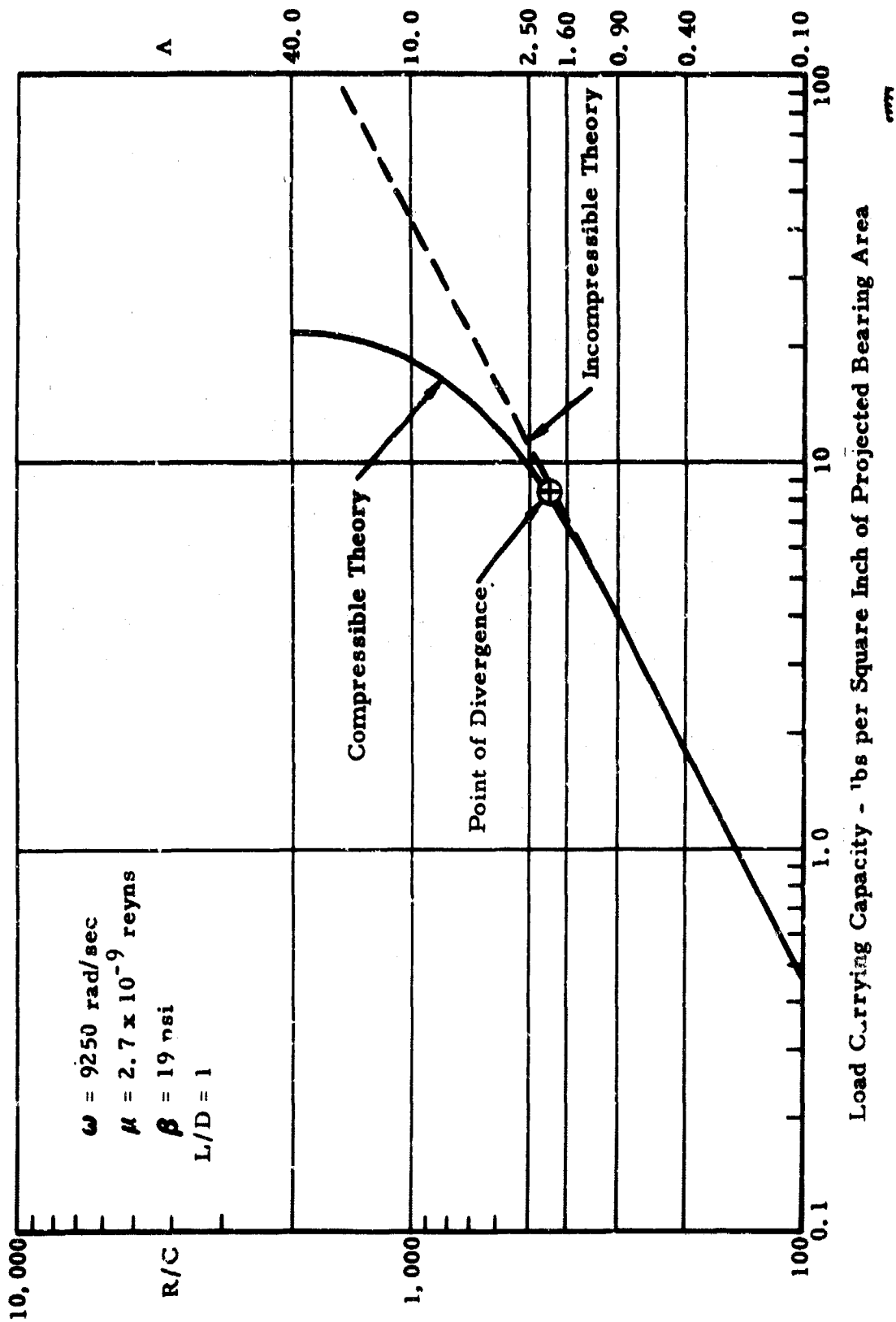
Another aspect of the high-pressure CO_2 employed as a bearing fluid is that the operating Reynold's number tends to infringe on the laminar-turbulent boundary as defined by Taylor's instability criterion. Very little work has been done on turbulent bearings, however, the experimental work reported by Smith and Fuller (Ref. 8) and the analytical treatment given by Constantinescu

**TABLE VIII. AIR BEARING PERFORMANCE:
COMPRESSIBILITY FACTOR AND LOAD
CARRYING CAPACITY AS FUNCTIONS
OF RADIAL CLEARANCE RATIO**

R/C	Λ	P'
100	0.10	0.48
150	0.23	1.10
200	0.40	1.88
300	0.90	4.01
400	1.60	6.70
500	2.50	9.50
600	3.60	12.30
800	6.40	16.00
1000	10.00	18.70
1500	22.50	20.90
2000	40.00	21.60

**TABLE IX. VISCOSITY CHARACTERISTICS
OF VARIOUS FLUIDS**

Fluid	Pressure	Temperature	Viscosity in reyns
Air	14.7 psia	70°F	2.6×10^{-9}
CO ₂	2000 psi	100°F	6.9×10^{-9}
Liquid Freon	—	100°F	30-90 $\times 10^{-9}$
Water	—	70°F	145×10^{-9}
Mercury	—	70°F	217×10^{-9}
Olive Oil	—	70°F	14500×10^{-9}
SAE 30	—	150°F	36000×10^{-9}



Load Carrying Capacity - lbs per Square Inch of Projected Bearing Area

Figure 16. Comparison of Bearing Load Carrying Capacity Incompressible Theory vs Compressible Theory

(Ref. 9) indicate that the consequence of operating at Reynold's numbers in excess of Taylor's value is not at all drastic but might be expected to result in somewhat higher friction factors and reduced whirl-instability resistance.

The complete lack of test and operational experience with supercritical CO₂ as a bearing fluid does present some uncertainties relating to the behavioral aspects of the fluid as a dynamic load carrying film. The tenacity of the film to resist rupture is of major importance. It would be expected that surface tension, adhesive properties, shearing rate, minimum film thickness, shaft and stator surface conditions, and fluid impurities would all have a significant influence on the stability of the load carrying film. Specific experimental verification of the supercritical CO₂ bearing design will be necessary to ensure reliable operation of the test CRU.

A list of radial bearing design specifications follows:

1. In order to minimize bearing losses, the bearing diameter should be as small as possible. However, design integration considerations limit the bearing diameter to 0.65 inch.
2. Consideration of overall rotor dynamics (discussed under a separate heading) indicated that the line-of-centers bearing stiffness should be 5×10^5 lbs per inch.

Note: Half-frequency whirl stability would also normally impose a minimum bearing stiffness requirement. However, in a rotor system designed to operate subcritically, i. e., maximum shaft speed is below the first resonant frequency of the shaft, bearing, and support system; the required bearing stiffness is greater than that necessary to suppress the half-frequency whirl instability. (See a more detailed discussion under Rotor Dynamics.)

3. The bearing length was set at 0.75 inch as a compromise between controlling end leakage, and the overall design integration considerations.
4. An active bearing arc of 160° was selected so that a hydrostatic loading pocket could be placed in opposition to the load carrying segment. The application of hydrostatic pressure in this pocket places the rotor under a steady, predetermined load that is reacted hydrodynamically by the action of the radial support bearings. The bearing will then operate at an eccentricity corresponding to the desired line-of-centers bearing stiffness. Furthermore, as mentioned previously, the application of this steady load will also serve to suppress the half frequency whirl instability tendency.
5. The minimum film thickness was set at .000100 inch. With due consideration for the aforementioned uncertainties as to the stability of a dynamic supercritical CO₂ load carrying film, the .000100-inch minimum film thickness appears to be a reasonable selection.

With these requirements, all that remains is to find the particular value for the bearing radial clearance so that at an operating eccentricity corresponding to a minimum film thickness of .000100 inch, the line-of-centers spring rate is 5×10^5 lbs per inch. After several trial-and-error cuts, a radial clearance of .000260 inch was found to give the desired results. A summary of the radial bearing geometry and operating characteristics are as follows:

Bearing diameter = 0.65 inch
Bearing length = 0.75 inch
Bearing radial clearance = 0.000260 inch
Fluid average viscosity = 4.95×10^{-9} reyns corresponding
to 2000 psi and 150°F
R/C ratio = 1250
Active bearing arc = 160°

The bearing performance was computed from the design charts of Boyd and Raimondi (Ref. 10).

The results, shown in Figure 17, are as follows:

shaft eccentricity ratio = 0.60
eccentricity = 0.000160 inch
minimum film thickness = 0.000100 inch
bearing load = 40 pounds
bearing attitude angle = 41°
line-of-centers load = 30 pounds
line-of-centers stiffness = 5×10^5 lbs per inch
viscous shear losses = 24 watts

The thrust bearing will react a rotor axial load of approximately 120 lbs at maximum power conditions. Due to the 30% reaction turbine, the rotor axial load will be decidedly unidirectional at all operating conditions so that a single acting bearing will suffice. At start-up, the rotor will be positioned in the anti-thrust direction, i. e., toward the pump, by stationary sapphire contact pins located on the pump-side of the thrust bearing rotor. (The unit will be mounted vertically, with the pump-end down.)

Although a design point load of 120 pounds for the approximate one square inch of effective thrust face area is relatively high for the usual self-acting gas bearing, the favorable properties of the working fluid, e. g., three-fold improvement in viscosity and an extremely high bulk modulus, greatly facilitate the design of a hydrodynamic bearing.

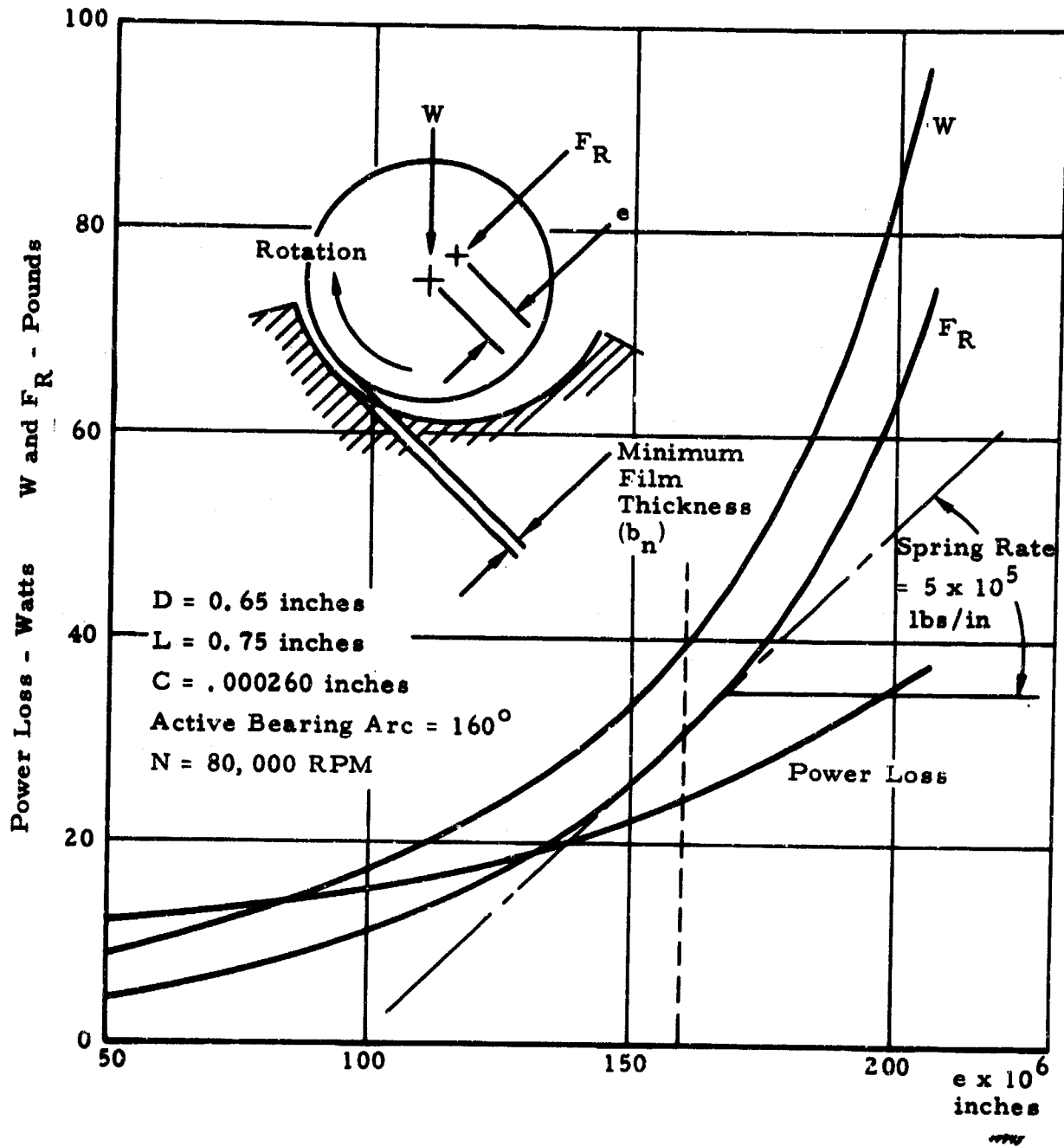


Figure 17. 10 kW_e CRU Radial Bearing Performance

Although the relative advantages and disadvantages of hydrodynamic and hydrostatic bearings are numerous and well known, the one consideration in the instance of the test CRU that appears to be decisive in favor of the self-acting bearing is the desirability of divorcing the bearing performance from the head developed by the pump. It might be necessary to operate the test unit under conditions which would materially affect the performance of a hydrostatic bearing. A self-acting bearing is generally tolerant of off-design circumstances and would be totally independent of the developed pump head.

A general parametric study was made for the self-acting thrust bearing in which the thrust face outer diameter was varied to establish the effect this has on the load, minimum film thickness, and the viscous power loss in the bearing.

The factors that were held constant for the analysis are as follows:

Thrust face inside diameter	= 0.70 inch
Effective fluid viscosity	= 6.85×10^{-9} reyns
Number of pads	= 6
Rotational speed	= 80,000 RPM
End-to-end pad film thickness ratio	= 2

The analysis follows the classical application of Reynold's equation to the tapered wedge. Leakage corrections were obtained from Theory and Practice of Lubrication for Engineers (Ref. 11).

The results of the thrust bearing study are shown in Figure 18. Having selected a minimum film thickness of .000100 inch at the design point, the thrust face outer diameter is 1.50 inches, and the fluid film viscous power loss is 178 watts. At the design point, the axial spring rate of the thrust bearing is 23.6×10^5 pounds per inch. This compliance, in conjunction with the approximate rotor mass of 1.8 pounds, provides an acceptable axial motion natural frequency of 215,000 cycles per minute.

4. ROTOR DYNAMICS

The dynamic design of a Feher cycle engine highlights an important advantage of the concept. The extremely compact and light turbomachinery, combined with relatively high stiffness radial bearings (a consequence of the process fluid incompressibility) makes it possible to design a subcritical CRU rotor system in the 10 kWe power class. A subcritical rotor system, i. e., the maximum rotor speed is less than the lowest resonant transverse frequency of the rotor-bearing-support dynamic system; has several distinct advantages including:

1. Flexibility to safely operate steady-state at any shaft speed up to maximum speed,
2. Lateral shaft motions are minimized thereby permitting minimum turbine tip clearance provision.

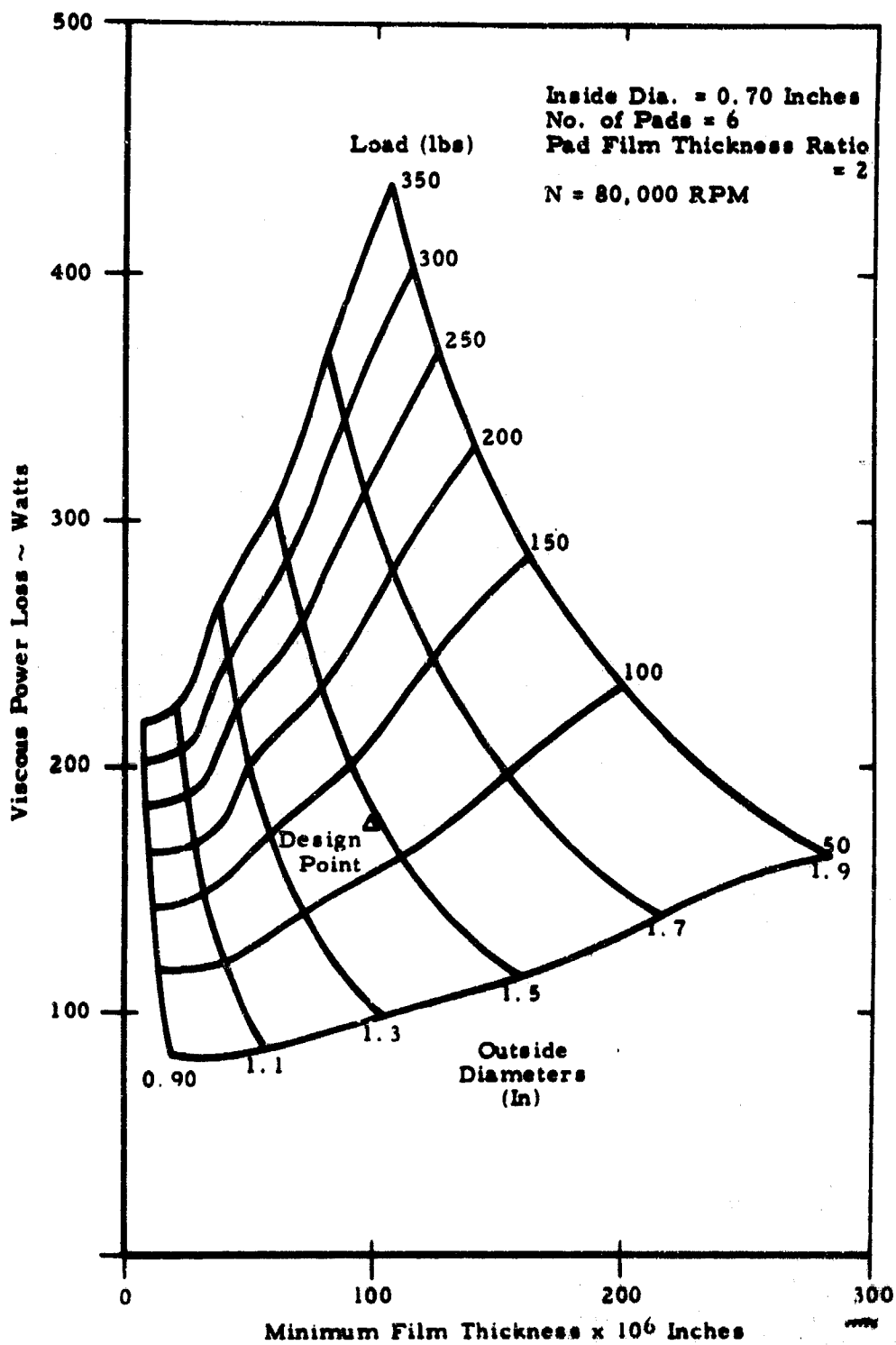


Figure 18. Thrust Bearing Analysis

The feature of being able to operate safely at all speeds below the maximum speed is of particular importance in the case of an experimental machine in that initial operation will undoubtedly occur at reduced speeds in order to avoid catastrophic failures at the outset of the program. Furthermore, engine performance at reduced speeds might be useful to the conduct of the research and development effort.

The usual approach in other CRU designs that employ process fluid bearings is to design a supercritical rotor dynamic system. In this case, the rotor maximum speed is well above the lowest transverse resonant frequency of the system. Indeed, in order to obtain a region of sufficient separation between adjacent modal shape resonant frequencies, it is often found necessary to adjust the stiffness of the bearings so that normal operation occurs between the second modal shape and the first rotor bending frequency. The development problems associated with supercritical dynamic systems are well known. The source of the difficulties are likely to stem from one or more of the following:

1. Inability to accurately tune the system for the safe operational regime due to the multitude of influencing factors.
2. Even momentary periods of operation (as when accelerating to design speed) at or near a system critical speed can result in bearing damage and harmful rotor deflections.
3. A low natural frequency system is susceptible to dangerous vibrations that might be excited by unexpected sources such as fluid pressure pulses, or resonances in adjoining structures.

Note: These would be true resonant vibratory motions whereas the previous references to subcritical and supercritical frequencies were concerned with the shaft instability which is usually identified as shaft criticals. The shaft assumes a modal shape which, without damping, will increase the amplitude of the modal shape deflection until failure occurs. However, even with sufficient damping to prevent failure, the deflected rotor will produce out-of-balance loads which rotate at rotor speed. It is these loads, and the vibration they produce, that are often the undesirable results of operating at or near a shaft critical. The confusion concerning shaft criticals and vibratory phenomena is of course due to the fact that numerically, the shaft criticals are identical to the corresponding modal shape transverse resonant frequencies.

In addition to the high stiffness bearings (see the discussion of the process fluid bearings under a separate heading) and the lightweight turbomachinery, it was necessary to consider rotor dynamics in the optimization of the alternator. The alternator subcontractor performed several design iterations that led to the adoption of a relatively short rotor configuration that required very little compromise on other performance and design considerations. The shortened rotor greatly facilitated the design of the subcritical rotor system. A

simplified analytical approach was used to establish the rotor system critical speeds. The Rayleigh Principle was used to establish an approximate third critical (rigid supports) for the distributed mass-variable stiffness rotor. With this value, an equivalent constant diameter shaft of the same length and the same third critical was computed. The dynamic model of the rotor system was then established as this constant diameter shaft on elastic supports. The solution for this system is (see as an example Reference 12):

$$\frac{K}{EIq^3} = \left\{ \begin{array}{l} \frac{\tan \frac{qL}{2} + \tanh \frac{qL}{2}}{2} \quad \text{or} \\ \frac{-\cot \frac{qL}{2} + \coth \frac{qL}{2}}{2} \end{array} \right.$$

where $q = \left(\frac{2W\omega^2}{gEIL} \right)^{1/4}$ and

E = shaft modulus of elasticity, psi

I = shaft moment of inertia, (inches)⁴

K = bearing stiffness, lbs per inch

W = 1/2 shaft weight, lbs

ω = natural frequency of the system, radians/sec

L = shaft length, inches

The transcendental functions were solved graphically. The results are shown in Figure 19 for various values of the bearing stiffness. At the design point bearing stiffness of 5×10^5 pounds per inch, the first critical speed is 135,000 RPM. Since the maximum rotor speed is 80,000 RPM, sufficient margin is indicated to accommodate unrecognized compliances, over-speeds, bearing performance uncertainties, and a comfortable displacement from the high response zone of the amplification-frequency spectrum.

In the final design, a more precise critical speed determination will be made in which an accounting of other structural compliances will be included. The Douglas Missile and Space Systems Division computer program library has available a program to handle up to 800 discrete mass points for a lumped-parameter type computation of the critical speeds.

A very common form of rotor instability in high speed turbomachinery that use fluid bearings is an orbiting motion of the rotor about the geometric rotor centerline at a frequency equal to about one-half rotor shaft speed. This orbiting motion tends to be divergent leading to severe unbalance loads and bearing failure. At the cost of bearing complexity, this whirling tendency can be suppressed by employing pivotable load pads, Rayleigh steps, rotor motion dampers, and other schemes to prevent the divergence phenomenon.

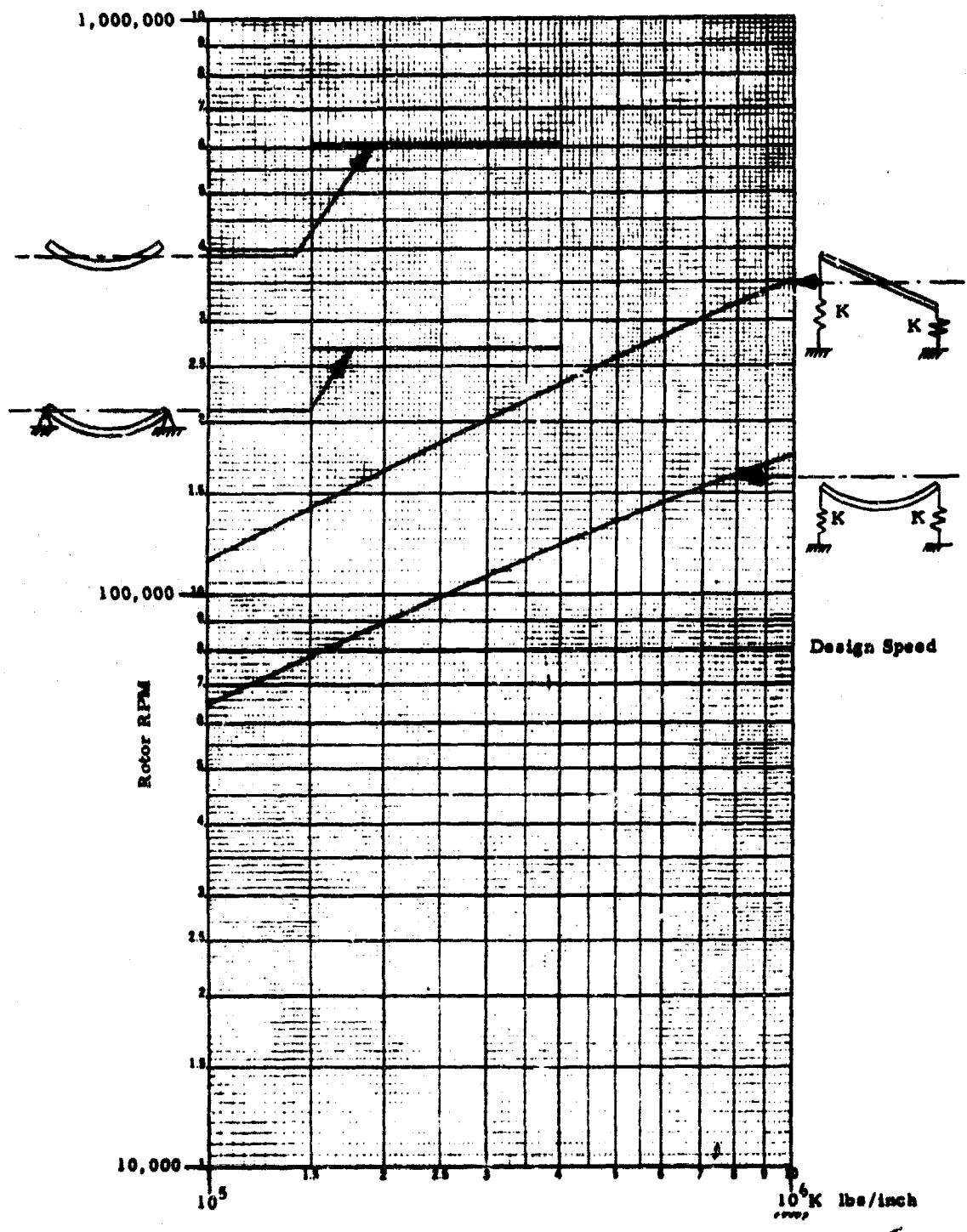


Figure 19. Rotor Critical Speeds vs Bearing Stiffness

Another method for preventing the half-frequency whirl instability is to supply static load to the bearing so that in its steady-state operation, the bearing develops sufficient stiffness in relation to the rotor mass that the system is stable.

Note: As a broad generalization, but reasonably accurate approximation, the bearing stiffness, K , is given by:

$$K = \frac{2W}{C} \text{ lbs per inch}$$

where W = bearing load in lbs

C = bearing radial clearance in inches.

The application of a steady load has been incorporated in the bearing design (described in detail under Bearings) for the purpose of stiffening the bearing so that the rotor system could be designed to be subcritical. It will be shown that a subcritical rotor design will necessarily involve a sufficiently stiff bearing that half-frequency whirl instability is prevented.

Consider a simple flexible shaft supported by a flexible bearing. It can be shown (see as an example Reference 14) that the first critical speed, ω_c , is approximately given by:

$$\omega_c^2 = \frac{1}{M} \frac{K_B + K_S}{K_B K_S}$$

where K_B = bearing stiffness

K_S = shaft stiffness,

M = rotor mass per bearing

Clearly, if the shaft stiffness was infinitely high,

$$\omega_c^2 = \frac{K_B}{M}$$

and that for $K_S < \infty$, the first critical is even less than

$$\sqrt{\frac{K_B}{M}}$$

From Reference 14, the expression for the half-frequency whirl threshold speed is

$$\omega^2 = \frac{4}{M} \frac{K_B + K_S}{K_B K_S}$$

which, for any combination of stiffnesses will produce a higher speed than the first critical shaft speed. In summary, the hydrostatic loading of the process fluid bearing intended to provide a subcritical rotor system, will, at the same time, prevent half-frequency whirl instability.

5. ALTERNATOR ANALYSIS AND PRELIMINARY DESIGN

The alternator design and analysis was performed by the Los Angeles Division of North American Rockwell Corporation under purchase order No. 7A-899081 from the McDonnell Douglas Corporation.

The work performed by the subcontractor in support of the 10 kW CRU Preliminary Design Task is as follows:

1. Conduct parametric studies of the alternator performance to obtain maximum overall efficiency (electrical plus viscous drag effects) consistent with interface constraints,
2. Cooperate with MDC to establish mutually compatible interfaces,
3. Perform a thermal analysis of the alternator for various boundary and cooling flow conditions so that environmental requirements could be established,
4. Prepare a test plan for the alternator which includes check-out at the subcontractor's facility, calibration and determination of electrical losses, and initial testing in CO₂ which is to be done at Astropower.

The major constraint imposed by MDC on the alternator configuration was to press for a sufficiently short rotor so that a subcritical rotor system could be designed (see Section 4 - Rotor Dynamics). After several trials, the subcontractor was able to propose a shortened rotor configuration that involved a negligible drop in overall efficiency, and an inconsequential increase in housing diameter and weight. This configuration was adopted and incorporated in the CRU design described in Section 8 - Design Integration.

A potentially difficult and complex interface was avoided by adopting a through-bolt rotor design so that the alternator rotor did not directly influence either bearing performance or turbomachinery positioning. Furthermore, the alternator housing was made nonstructural by employing an outer shell (MDC responsibility) which provides the structural coupling between the two rotor bearing supports. These features are described in detail in Section 8 - Design Integration.

The results of the thermal analysis conducted by the alternator subcontractor indicated that the water coolant loop could be eliminated. The alternator will be cooled by maintaining a 250°F environment in the vicinity of the alternator housing, and by directing small quantities of low temperature process fluid to heat generation locations within the alternator. The primary objection to the water cooling is that unnecessarily severe thermal

gradients might induce structural problems in the CRU, and in addition, the water plumbing is subjected to an 1800 psi differential which complicates the design of the coolant system and introduces, to some degree at least, a potential problem source.

The balance of the material presented in this section has been extracted, without change, from the subcontractor's final report to MDC. The drawing of the alternator assembly, Figure 27, does not reflect the decision to eliminate the water cooling. In addition, the means for attaching the alternator assembly to the CRU structure is not shown but is included in Section 8 - Design Integration.

a. Alternate Generator Types

An evaluation was made of the design features and operational capabilities of the basic alternator types suitable for high speed, high efficiency operation in a CO₂ environment. A review of the advantages and disadvantages of the types of machines considered is given below.

(1) Wound-Rotor Machines

Wound-rotor, rotating rectifier machines are not suitable for direct connection to high-speed turbines because of relatively low peripheral speed limits imposed by field winding structural and balance limitations. Peripheral speeds are limited to less than 400 feet per second (approximately 900 feet per second is required for direct connection at 80,000 rpm) and as such require the use of a gearbox between the engine and generator. The gearbox forces a substantial weight and volume penalty undesirable for compact lightweight power systems. Furthermore, the added gearbox losses due to operation in a CO₂ environment would reduce the system efficiency. Also, reliability is decreased because of gearbox problems and little opportunity is available for improvement in second generation systems. The wound rotor alternator was not selected for these reasons.

Solid-rotor alternators have the capability of high peripheral speeds and offer the best potential for the intended application.

(2) Solid-Rotor Machines

Permanent magnet, reluctance, hysteresis, and induction alternators, although brushless, are considered inherently unsuitable for the following basic reasons. Permanent magnet alternators have poor regulation characteristics, tend to be large because of low flux densities, and are difficult to fabricate with the structural integrity required for operation at high speed. Reluctance, hysteresis, and induction generators are capable of supplying real power only, and must receive reactive power for excitation sources from a separate supply. These types, therefore, are excluded from further consideration because of added capacitor weight.

The family of alternator types, which includes the Inductor, Lundell, Inductor-Lundell, and the NADYNE alternator, generally receive

consideration for applications requiring long life and high reliability. Figure 20 shows the basic schematics of these machines. The entire family is predominantly marked by the generation of field flux in a field coil mounted as part of the stator, with the flux transferred into the rotor across an air gap. Generation of field flux in this way permits windings to be removed from their classic position on each pole of the rotor, thus eliminating all conductors, insulators, brushes, slip rings, or rotating rectifiers from the rotor, with a subsequent elimination of many problem areas that certainly would lower reliability.

(a) Inductor Machine

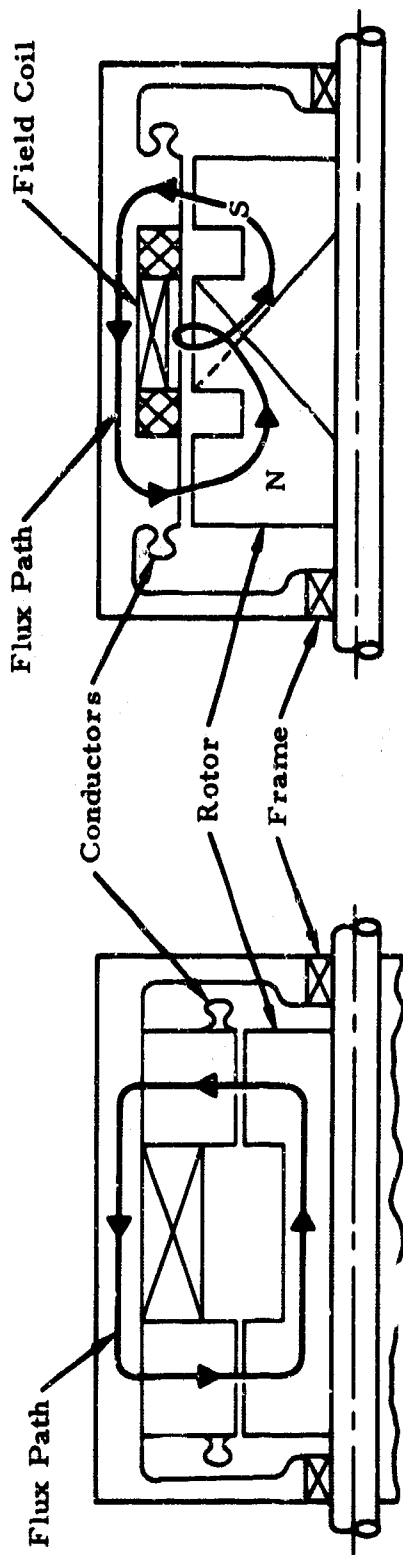
The inductor machine (double hemipolar design) has a particularly simple rotor construction that is well suited to high speed and high temperature. In this design, the field windings are mounted in a central location on the stator. The magnetic flux follows low reluctance paths through the stator into a rotor body, and into the stator through a second pole. At each pole, the flux alternates from essentially zero to full north or south, respectively. Magnetic steel is utilized to only half of its capacity in either positive or negative flux direction (but not both) and, therefore, nearly twice as much magnetic material is required as is theoretically possible. The longer parts result in increased weight and size in addition to a low efficiency. Low efficiency is brought about by three factors: increased copper losses, increased windage losses, and increased core losses. All three are a direct result of a long stator and rotor. An important aspect of this type of machine is that the total number of poles are split between each end of the rotor. That is, a four-pole machine has two poles at each extremity of the rotor and six-pole machine has three. Accordingly, dynamic and static balance are inherent in the rotor except when two poles are used. This machine is the heaviest of the solid alternators and the least efficient per pound of machine weight. It is discarded because of these characteristics.

(b) Lundell Machine

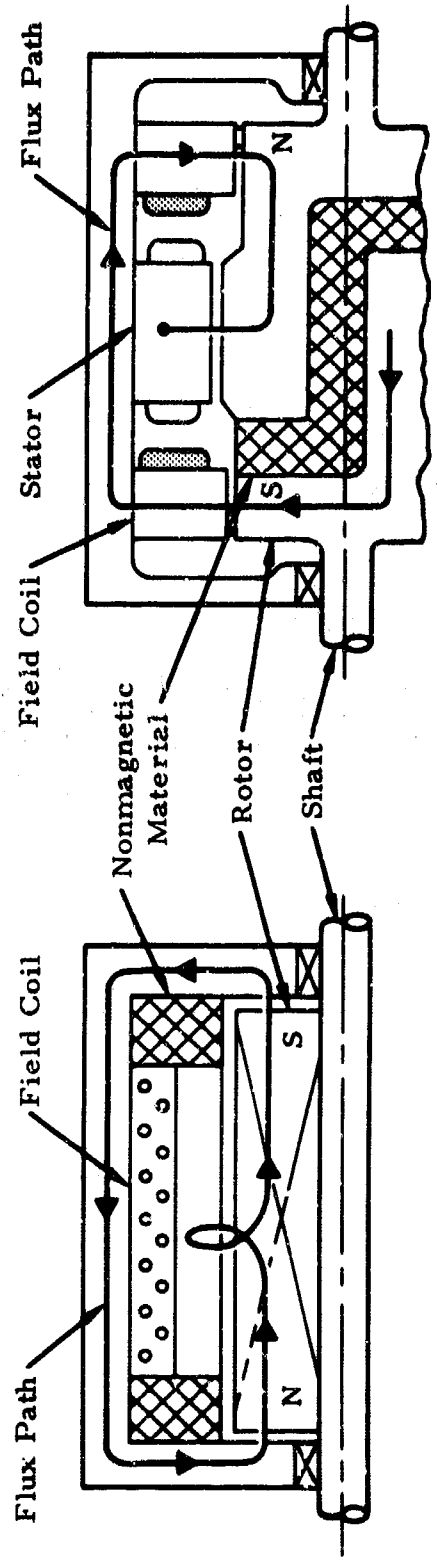
The pure Lundell configuration (Figure 20), which has advantages in some applications, has the disadvantage of high field leakage, and the subsequent high weight per kilovolt-ampere which results. The high rotor leakage also has adverse effects on transient performance and voltage recovery times because of the magnetomotive force difference between the armature and the frame. A variation of the basic design, the inside-coil Lundell, or Bechy Robinson machine, has stationary field coils mounted inside a cantilevered section of the rotor. This machine is close cousin of the NADYNE machine but the latter design greatly reduces leakage. The cantilevered field poles also cause a substantial rotor overhang which seriously limits maximum peripheral speed. The maximum peripheral speed for this machine is on the order of 500 feet per second which is less than that required for the imposed application. It is rejected for this reason.

(c) Inductor-Lundell

The Inductor-Lundell design combines the features of a pure Lundell and an Inductor. The basic scheme can be seen from Figure 20.



(c) Inductor - Lundell



(d) Nadyne

Figure 20. Generator Principles

This type of machine has an inductor section at each end of the shaft, and a Lundell section in the center. At each end of the rotor, voltage is induced in the conductor by a magnetic flux alternating from a given value to zero. The plus-flux (or north pole) is on one end, and the minus-flux (south pole) on the other. At each end, the Inductor-Lundell also utilizes only half of the capacity of the magnetic steel. However, in the Lundell section, the voltage in the stator conductors is induced by a flux alternating from plus (north) to minus (south) and the magnetic steel is utilized to full capacity. Combining the Inductor and Lundell characteristics onto one rotor allows the relatively high leakage flux of the Lundell section to be utilized in the inductor section, and also eliminates parasitic air gaps. The major disadvantage of the design is that the poles are overhung, thus introducing more mass to be acted on by centrifugal force and the high losses associated with the long rotor and three stators. Its weight is somewhat less than an inductor but considerably higher than the NADYNE.

(d) NADYNE Machine (Synchronous Inductor)

The basic configuration of the NADYNE is shown in Figure 21. The solid rotor is a completely smooth cylinder of revolution containing both north and south poles separated by a nonmagnetic material.

The NADYNE machine generates voltage in the same manner as the conventional salient pole wound field generator. A magnetic field of alternate north and south polarity is rotated mechanically past the generator conductors, thus generating a voltage in the stator conductors by causing a change in the flux linkages of the conductors as a function of time, or a voltage introduced by the rate of cutting flux lines. The stator of the generator is of conventional design. The same design formulas useful for good stator design of synchronous generators is applicable as the method of generator output power is identical in both types of generators.

The magnetic circuit of the stator section of the generator is also identical to the conventional synchronous generator stator. The excitation magnetic circuit is different and is designed to remove all excitation coils from the rotor of the generator, the magnetic circuit, and flux path. The flux path, starting from the concentric gap of the right-hand pole, is across the gap and then axially towards the center of the rotor. It divides equally between the number of like-poles and then travels across the rotor pole gap to the stator iron. In the stator iron it has two possible return paths; one through the stator yoke to the opposite polarity rotor pole, and the other through the magnetic frame. As the rotor is turning during operation, the least resistant flux path is through the laminated stator yoke iron; the frame being solid offers higher reluctance to a changing flux than the laminated stator iron. Therefore, the flux path is through the stator yoke and across the air gap to the polarity rotor pole. The flux will then continue axially to the left end of the rotor and return through the concentric gap to the left field pole and then to the magnetic frame. In the magnetic frame the flux flows axially to the right-hand field pole completing its circuit in the pole at the concentric gap. The rotor flux rotates with the rotor and under steady-state conditions is of constant magnitude and unchanging. This is the same as the flux in the rotor of a wound field salient pole generator.

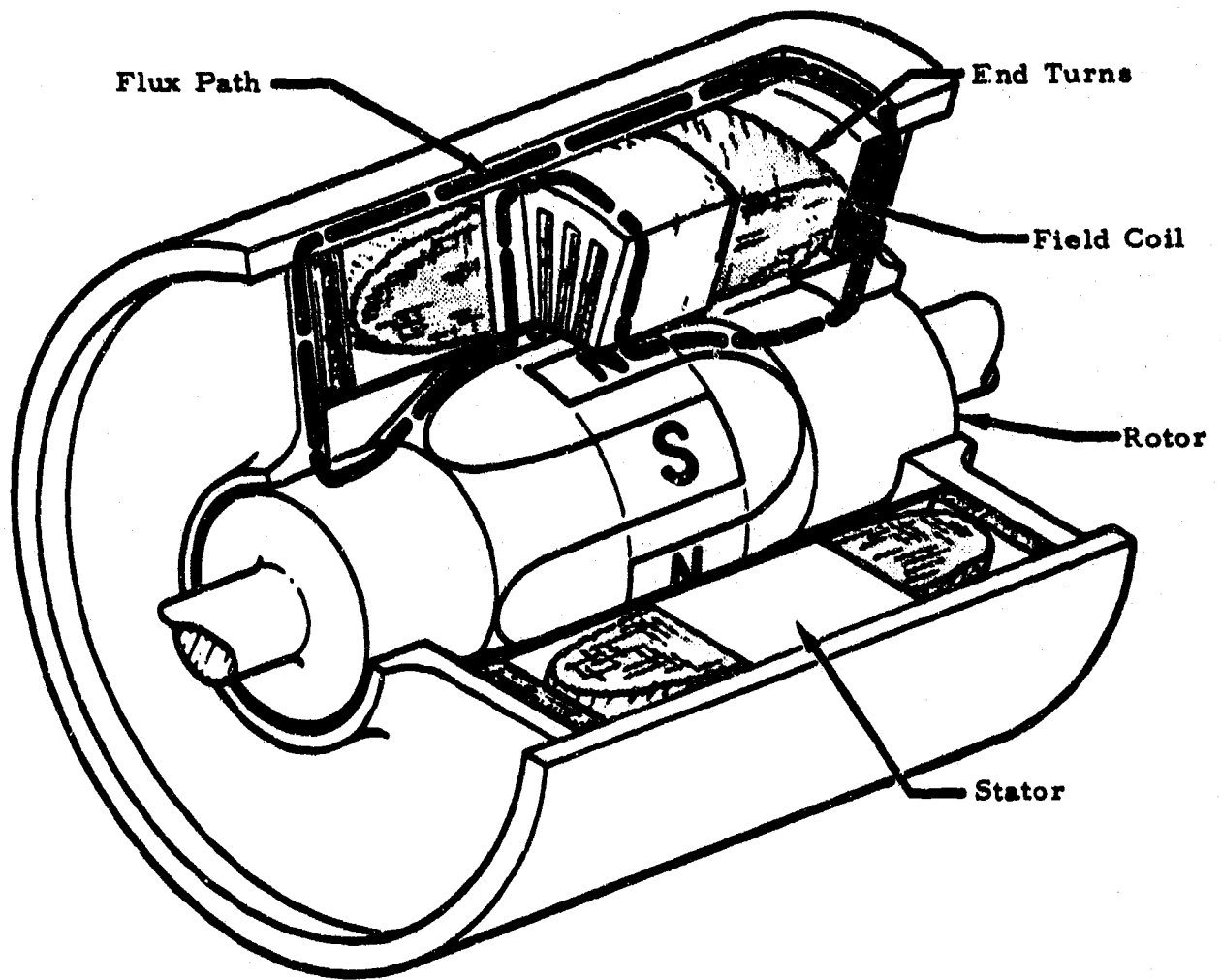


Figure 21. Nadyne Alternator Concept

The frame and pole flux under steady-state conditions is of fixed magnitude and unchanging in the poles and frame. The flux transition from rotating to non-rotating takes place at the pole annular air gaps. As the pole gap is concentric, the flux density is constant around the periphery of the rotor pole, and the rotor pole does not see a varying flux under steady-state conditions; therefore, a power loss is not induced in the rotor at the field gap. The magnetomotive force (MMF) is produced by a direct current flowing in the field coils located on each end as shown in Figure 21. One coil is used for each polarity and a single coil will excite the total number used for each polarity. The field coils are fixed to the stationary parts and do not rotate with the rotor. The poles and frame are made from magnetic material. The areas of the materials in a plane perpendicular to the flux path are designed sufficiently large to carry the total flux per magnetic polarity plus all leakage fluxes without saturating the magnetic materials. The flux distribution is such that the magnetic forces acting on the rotor poles are equal and opposite. Therefore, the magnetic forces cancel and do not impose unbalanced, mechanical forces on the generator bearings. This balanced condition exists regardless of the number of poles.

Table X is a qualitative summary of the four solid-rotor alternator types, using the NADYNE alternator characteristics as a base.

Figure 22 is a photograph of an 11 kW 80,000 RPM NADYNE alternator rotor. This rotor has been successfully spin tested to 130,000 RPM. The stator and housing are shown in Figure 23.

b. Power-Speed Trade Off Study

(1) Computer Program

There are many design factors which influence the alternator performance characteristics. Each of the factors which affect a given specification requirement must be considered in relation to its effects on other performance requirements. Table XI lists the important generator design variables together with a brief statement describing the generator or electrical system characteristic most affected by the design variable. For example, design variable number 12, radial gap, will have a strong effect on the value of X_d (Direct Axis Synchronous Reactance), no load pole face losses, the amount of field power required to excite the generator, and the amount of rotor leakage flux. Since the radial gap has a strong effect on the value of " X_d ", it also affects generator weight, efficiency, voltage regulation, short circuit and voltage transients. Each of these in turn has its own effects on design and performance. Since most of the design variables are interrelated like the illustration above, the determination of the effect of one variable on the others can only be accomplished with the aid of a comprehensive computer program. A North American Rockwell developed "NADYNE Epcode Program" is such a program and has been used to obtain the parametric data of this report.

Epcode is a generalized control program, designed specifically for machine design. It is equipped with its own command language and

TABLE X. PERFORMANCE SUMMARY

	<u>Nadyne</u>	<u>Inductor</u>	<u>Inductor Lundell</u>	<u>Lundell</u>
Stator Conductor Loss	1.0	1.5	1.6	1.0
Stator Iron Loss	1.0	1.7	1.5	1.1
Excitation Conductor Loss	1.0	1.5	1.5	1.7
Rotor Drag Loss	1.0	8.0	7.0	1.0
Rotor Pole Face Loss	1.0	1.5	1.3	1.2
Weight	1.0	1.8	1.6	1.2



0070

Figure 22. 11 kW Nadyne Rotor

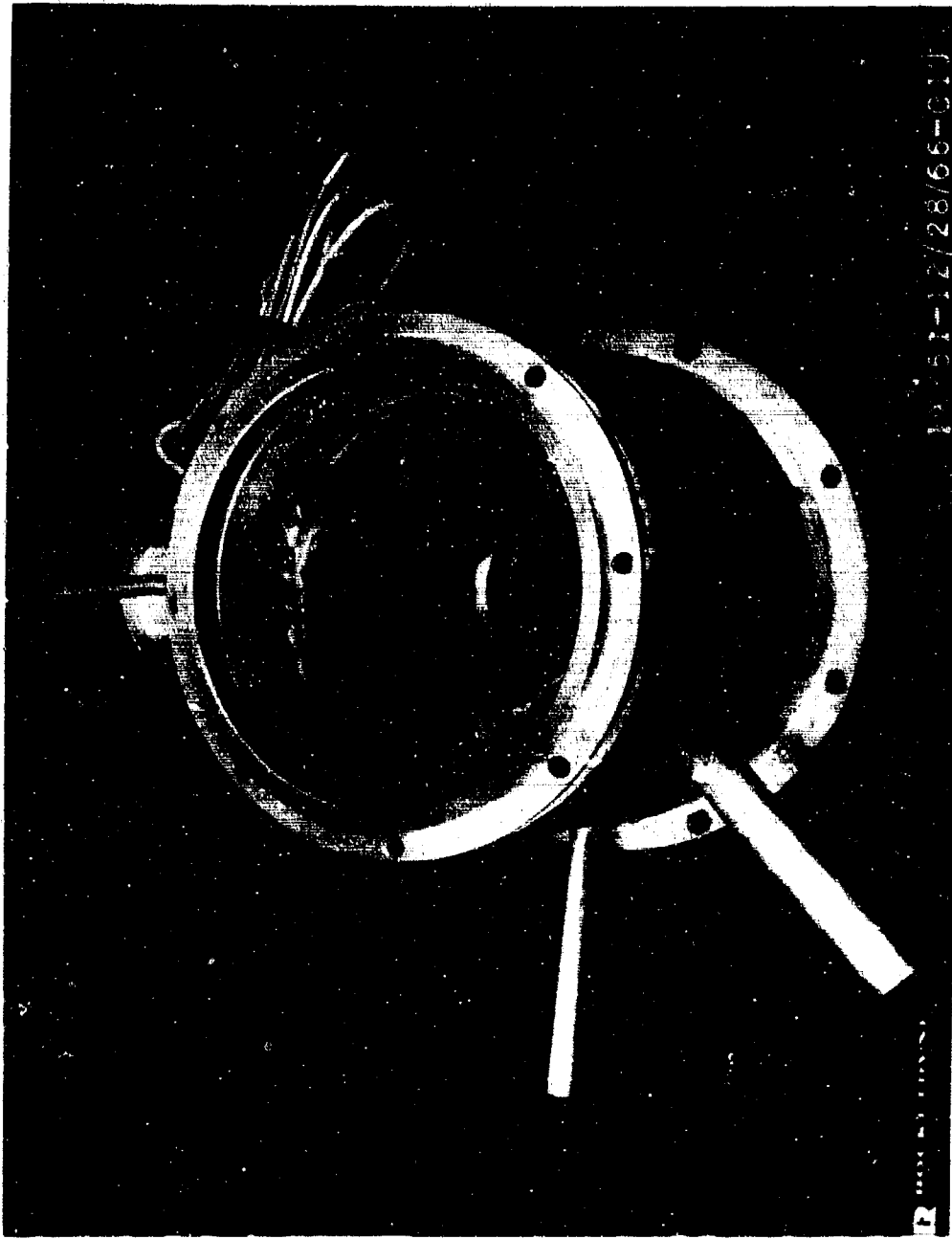


Figure 23. 11 kW Stator and Housing Assembly

TABLE XI. LIST OF PRIMARY DESIGN VARIABLES

<u>Design Variable</u>	<u>Primary Characteristics Affected</u>
1. Rotor Speed	Rotor stress, no-load and load pole face losses, windage loss, weight, efficiency
2. Frequency	Weight, efficiency, load pole face loss
3. Voltage	Insulation thickness, slot space factor, probability of voltage breakdown, corona, line current, weight, efficiency
4. Flux Densities	Weight, magnetic losses, field power
5. Current Densities	Conductor operating temperature, slot size, copper losses
6. Number of Poles	Direct axis synchronous reactance " X_d ," depth behind slot, magnetic force unbalance, length of end extension
7. Pole Embrace	Depth behind slot, stack length, useful flux ratio, rotor stress, amplitude of fundamental flux component, form factor
8. Rotor O. D.	Rotor stress, no load and load pole face loss, windage loss
9. Rotor Length	Rotor dynamics
10. Useful Flux Ratio	Weight, efficiency
11. Direct Axis Synchronous Reactance " X_d "	Load pole face loss, weight, efficiency, field power, voltage transients, voltage regulation, short circuit currents, parallel operation stability, voltage unbalance
12. Radial Gap	Direct axis synchronous reactance
13. Load Power Factor	Weight, efficiency, voltage regulation
14. Fractional Slot or Integral Slot Windings	Load pole face loss, electrical interference
15. Pitch Factor	Voltage harmonic content, weight, end extension length, efficiency
16. Slot Skew	Slot harmonic amplitude, load pole face loss, ease of development with rigid insulation systems

(continued)

TABLE XI. LIST OF PRIMARY DESIGN VARIABLES (concluded)

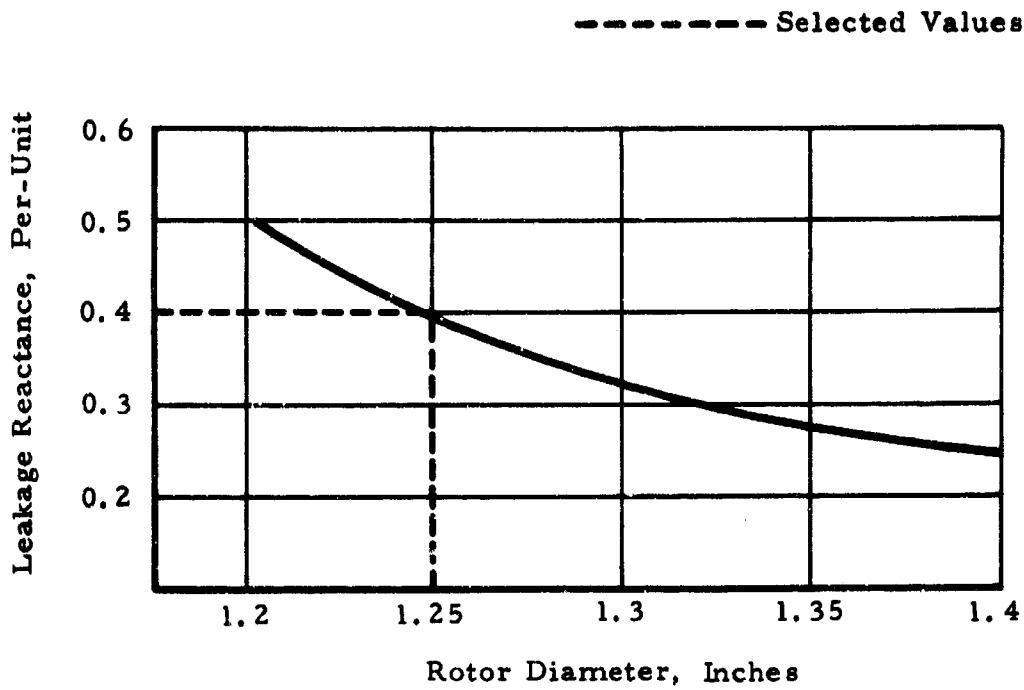
<u>Design Variable</u>	<u>Primary Characteristics Affected</u>
17. Open or Closed Slot	Leakage reactance, no load pole face loss, ease of inserting armature conductors
18. Slot Fill Factor (ratio of copper area to slot area)	Weight, rotor O. D., slot heat transfer
19. Conductor Insulation Thickness and Slot Cell Thickness	Slot space factor, probability of voltage breakdown, slot heat transfer
20. Phase Separator Thickness	Slot space factor, probability of breakdown, leakage reactance
21. Round or Rectangular Conductors	Slot space factor, field windage size
22. Degree of Phase Belts	Voltage wave form (harmonic content) weight, magnetic losses, load pole face loss
23. Ratio of Tooth Width to Slot Pitch	Stack length, weight, depth behind slot, no load pole face loss
24. Armature Stacking Factor	Stack length, rotor length, weight
25. Armature Lamination Thickness	Magnetic losses, stacking factor, ease of development handling
26. Flux Leakage Factor	Weight, copper loss, rotor length, leakage reactance
27. Field Winding Clearances	Weight
28. Resistivity and Permeability of Pole Face Material	No load and load pole face losses
29. Field Winding Thermal Conductivity	Field cooling configuration
30. Thermal conductivity of material in slot clearances or contact conductivity of slot insulation and armature magnetic material	Stator cooling configuration, conductor operating temperature
31. Thermal Conductivity of Armature Conductor	End extension cooling configuration, end extension hot spot temperature
32. Pole Face Losses	Rotor cooling configuration, ease of development
33. Material Properties (in general)	Feasibility, weight, size, losses, internal temperatures

designed for operating within the Fortran computer system. Basically, it relieves the machine designer of all computer programming chores once the basic arithmetic calculation routines are coded and checked-out. It is most effective in handling up to several hundred individual parameters which must each be iterated independently of one another to determine their effect on the entire design.

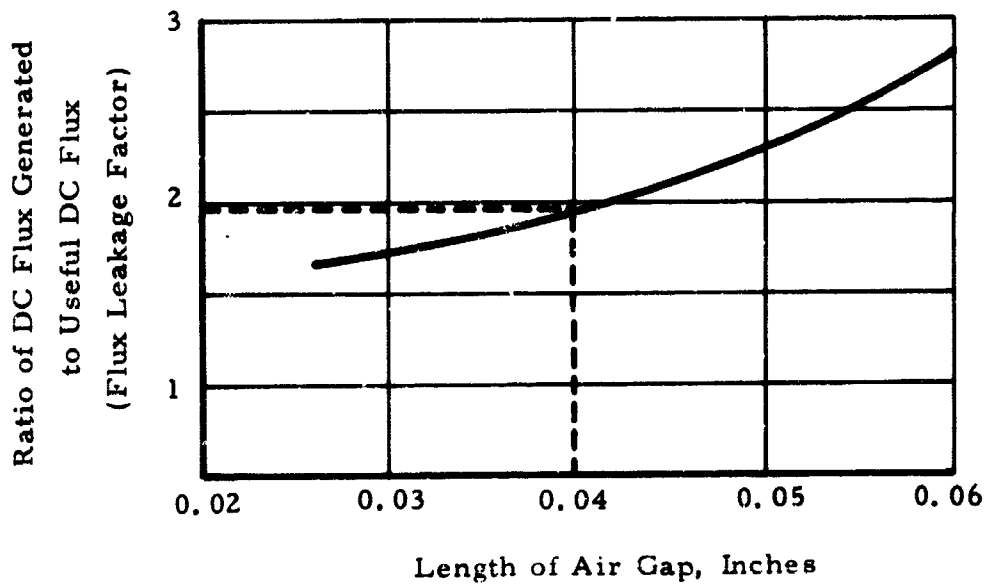
(2) Analysis Procedure

Using the Nadyne Epcode computer program, trade-off data for 5.5 kW, 8 kW, and 10 kW Nadyne alternators have been investigated as a function of speed. Machines were optimized for each power level above at 20,000 RPM increments starting at 60,000 RPM to obtain the curves shown in Figures 27 and 28. Many of the design variables shown in Table XI are held constant for each particular design such as material properties, pitch factor, pole embrace, etc. and others must be established by iterations. Four variables that most influence the size and performance of the design are the rotor diameter, stator air gap flux density, stator current density, and the ratio of field ampere turns to stator ampere turns. These parameters are individually iterated along with several others to obtain the optimum machine. Each machine selected to obtain the trade-off curves must not only be optimized for weight and efficiency but also for reactance, flux leakages, and saturation.

As an example, the design procedure followed to obtain the 5.5 kW, 2 pole alternator at 60,000 shown in Figure 27 will be discussed. Machine ratings such as power level, speed, frequency, voltage, etc. are established along with fixed Nadyne alternator parameters based on experience and past designs. The rotor diameter was iterated independently to establish its relationship to the stator leakage reactance. Too large a leakage reactance may result in saturation of the machine iron causing less than a rated power output. Figure 24A is a plot of the leakage reactance versus rotor diameter. From past experience, it was established that the leakage reactance should be less than .40 per unit. This requirement set the minimum rotor diameter at 1.25 inches. Larger rotor diameters produced more favorable leakage reactances but would also unfavorably increase the rotor drag losses. Figure 24B is a trade-off plot of flux leakage factor to air gap length. Smaller air gaps result in a lower more favorable flux leakage factor which is desirable in order to minimize the magnetic cross sectional areas of the machine and also minimize the heating losses of the field. The disadvantages of the smaller air gap however, are (1) larger synchronous reactance which reduces the amount of short circuit current for fault clearing and (2) increased rotor drag losses. As a compromise, the air gap was established at .04 inch. Stator current density and air gap flux density also greatly affect the size and performance of the alternator. Figure 25A shows the effect of stator current on weight and efficiency. Since efficiency for this application was of greater importance than weight, the optimum current density was selected at 4000 amps per sq. in. Current density below 4000 amps per sq. in. may have resulted in slightly higher efficiencies, however, the machine weight increased severely. Figure 25-B demonstrates that efficiency reaches a maximum at an air gap flux density of 40 K-lines per in.²; increasing the air gap flux



A



B

Figure 24. 5.5 kW 2-Pole Nadyne Alternator
Trade-Off Parameters

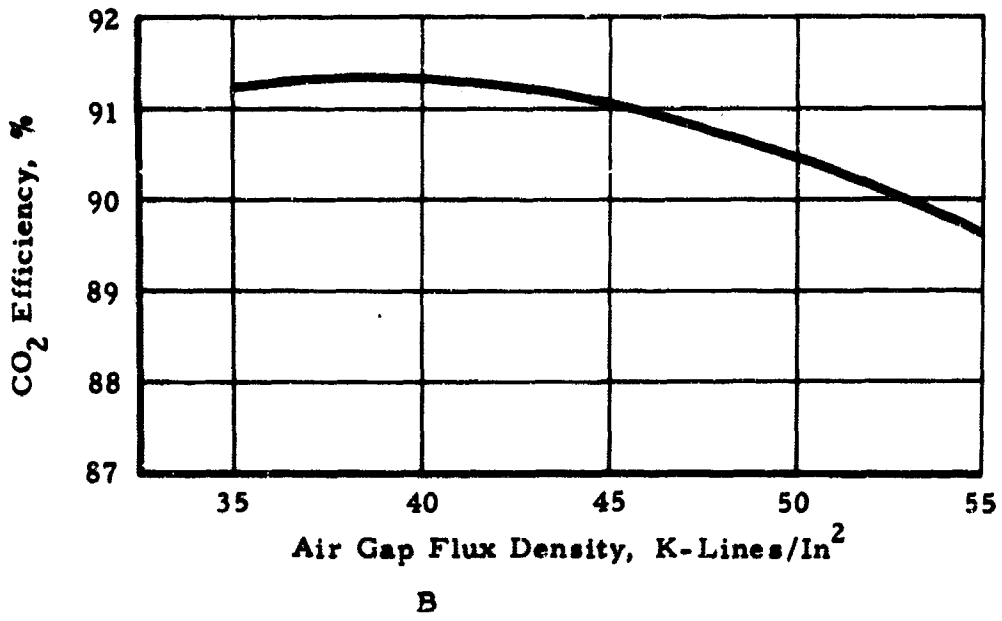
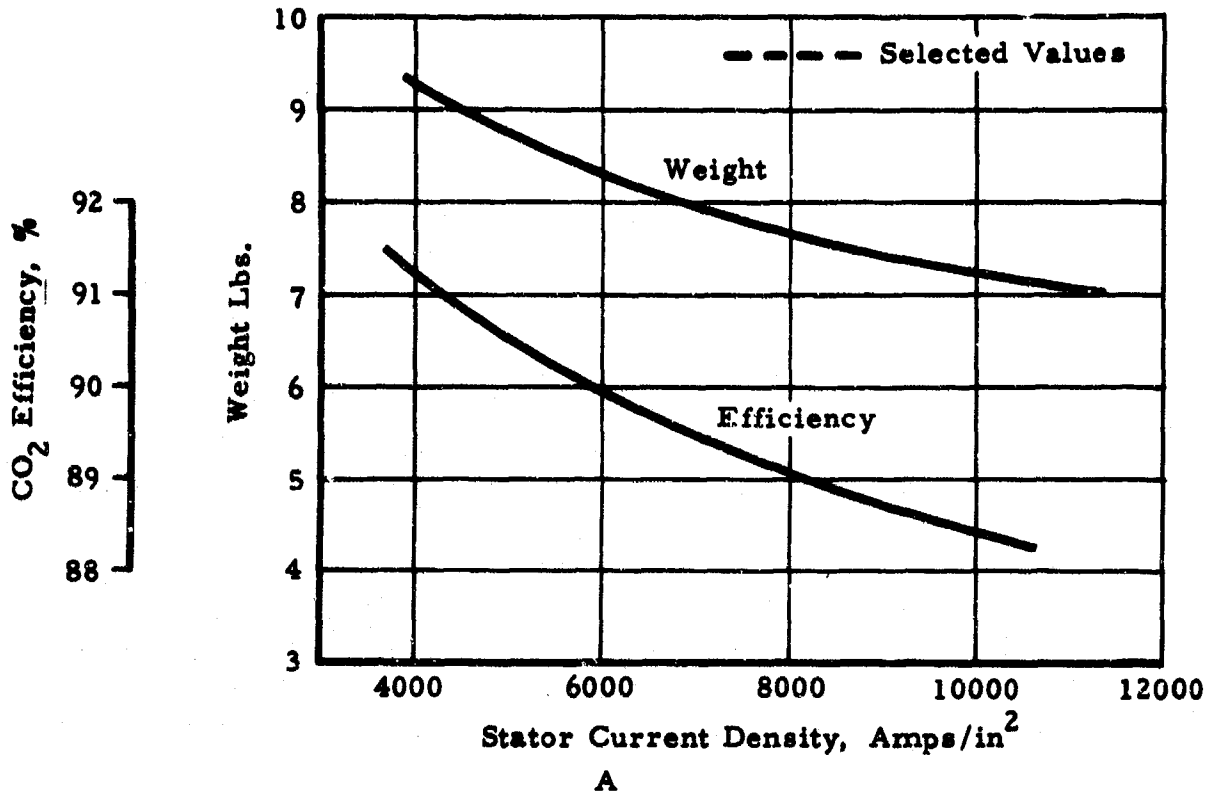


Figure 25. 5.5 kW 2-Pole Nadyne Alternator Weight-Efficiency Trade-Off

density further produced increased rotor pole face losses which lowered the efficiency.

These are a few of the most influential parameters that affect the alternator size and performance which must be evaluated before establishing optimum preliminary machines. This procedure was repeated at 80,000 RPM, 100,000 RPM, 120,000 RPM, and 140,000 RPM to obtain the curves shown in Figure 27.

(3) Alternator Pole Selection

Figures 27 and 28 show optimized two and four pole Nadyne alternators plotted as a function of speed. From these curves it can be seen that the two pole machines are between 2 - 3% more efficient than the four pole machines at all speeds. This is accounted for by (1) less hysteresis and eddy current losses resulting from lower frequencies and (2), less rotor drag losses resulting from smaller rotor diameters. The four pole machines however, are lighter than the two pole machines because the stator copper and iron operate with half the flux per pole as the two pole machine. Since efficiency in this application is paramount compared to weight, the decision was to favor the two pole alternators in lieu of four pole alternators. The 8 kW and 10 kW parametric data presented in this report were therefore based only on the two pole configuration.

(4) Rotor Drag Losses

In order to predict the efficiency of the Nadyne alternator operating in a high pressure high temperature CO₂ environment, an analytic drag loss equation has been developed by North American Rockwell, Corporation. The equation shown below has been developed over a span of time, primarily as a result of pump rotor experience, but it is perfectly applicable to alternator rotor drag computations. The equation is as follows:

$$\text{kW}_{\text{loss}} = \left[\frac{\mu_a^{.43} D_R^{3.57} N^{2.57} L_S \rho_A^{.57}}{G_S^{.43}} \right] 2.66 \times 10^{-15} +$$

$$\left[\frac{\mu_a^{.43} D_E^{3.57} N^{2.57} L_F \rho_A^{.57}}{G_F^{.43}} \right] 5.32 \times 10^{-15} +$$

$$\left[D_E^{4.6} \mu_a^{.2} \rho_A^{.8} N^{2.8} \right] 2.79 \times 10^{-16}$$

where μ_a = liquid or gas viscosity, lb/hr-ft
 D_R = rotor diameter under stator, inches

- D_E = rotor diameter under field pole, inches
 N = rotor speed, RPM
 L_S = length of rotor under stator, inches
 ρ_A = liquid or gas density, lbs/cu. ft.
 G_S = stator air gap length, inches
 L_F = length of rotor under field pole, inches
 G_F = field air gap length, inches

The first term in the equation accounts for the drag loss occurring in the stator air gap, the second term accounts for drag loss occurring in both field gaps, and the third term accounts for the drag loss occurring on both ends of the rotor. Note that in the first two terms, the air gap length G occurs in the denominator and must therefore be kept as large as possible to minimize the drag losses. The rotor diameters have also been minimized to reduce drag losses by selection of a high flux density magnetic rotor material (Hyperco 27).

A number of test rotor models (2, 3, and 6 inch diameters and 6 inches long) were tested in a number of fluids (water, methyl alcohol and Dow Corning 200 silicone oil) at room and near-freezing (32°F) temperature to verify this equation. Results for the 3 inch model with an 0.030 inch gap operating in water are shown in Figure 26 and are typical of agreement between predicted and test results which verify the validity of the analytic equation.

In each of the drag tests, the rotor model was accelerated to the drive speed by an electric motor (for the unpressurized tests) or hydraulic motor (for the pressurized tests), disengaged from the drive, and allowed to coast to a stop. The plot of rotor speed versus time during coast-down permitted the computation of rotor drag loss because of the presence of the fluid in the rotor cavity.

Additional tests in a pressure chamber were conducted using the 3 inch model in both methyl alcohol and the Dow Corning 200 silicone fluid. Drag losses were almost identical to losses experienced at atmospheric pressure. The effect of temperature on drag losses (due to changing viscosity) was more significant than the effect of pressure.

Although no drag tests were performed using high pressure CO₂, the drag formula has been successfully verified with liquids of various densities and viscosities. CO₂, however, at 400°F and 1800 psi behaves much like a liquid and should therefore provide valid analytical drag loss data. The CO₂ density and viscosity used in this study was 9.43 lb/cu. ft. and .0609 lb/hr-ft., respectively. The CO₂ drag losses will be determined by tests during phase II of this program.

The rotor-end drag losses have been included on all machines in this report.

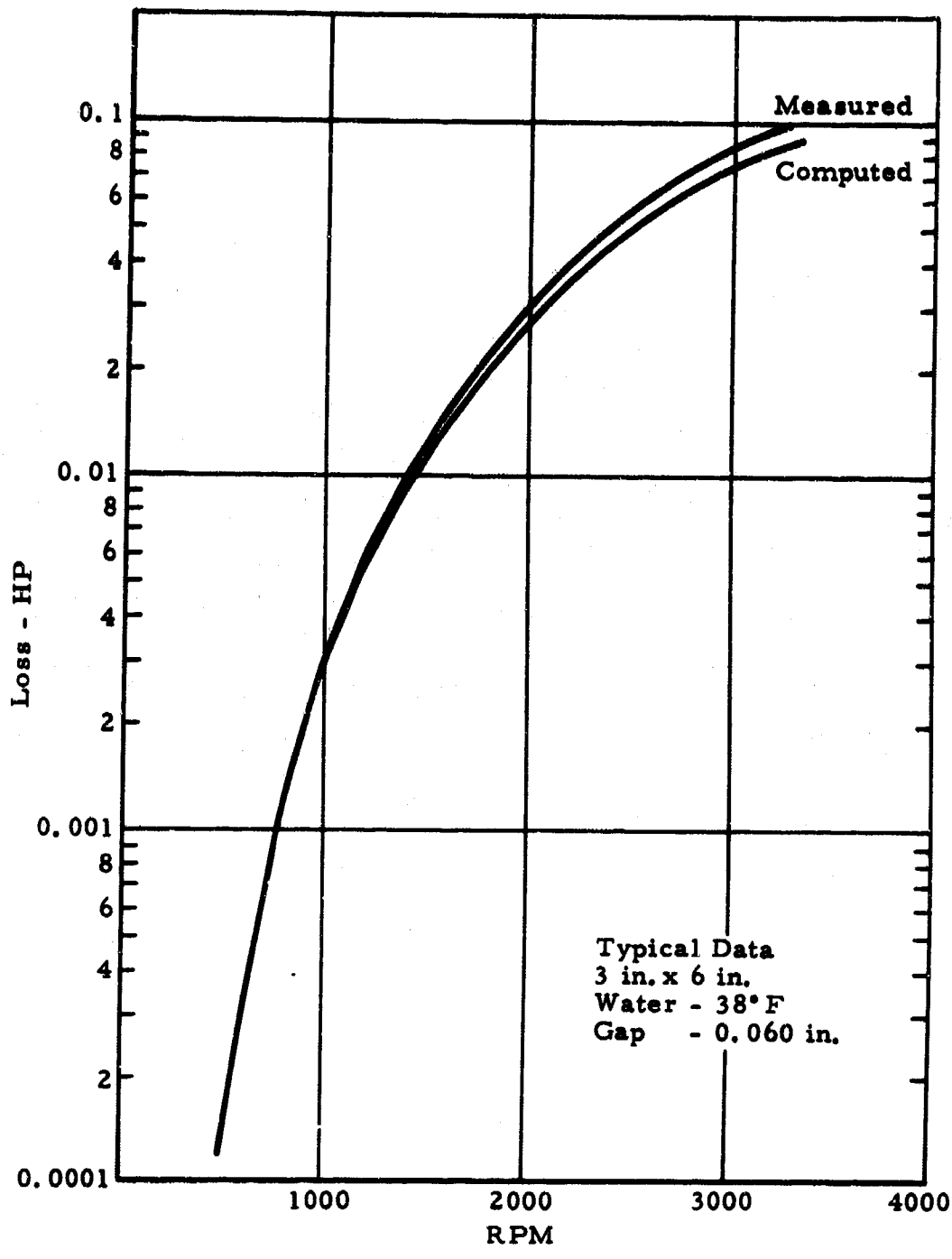


Figure 26. Fluid Churning Load Measurements

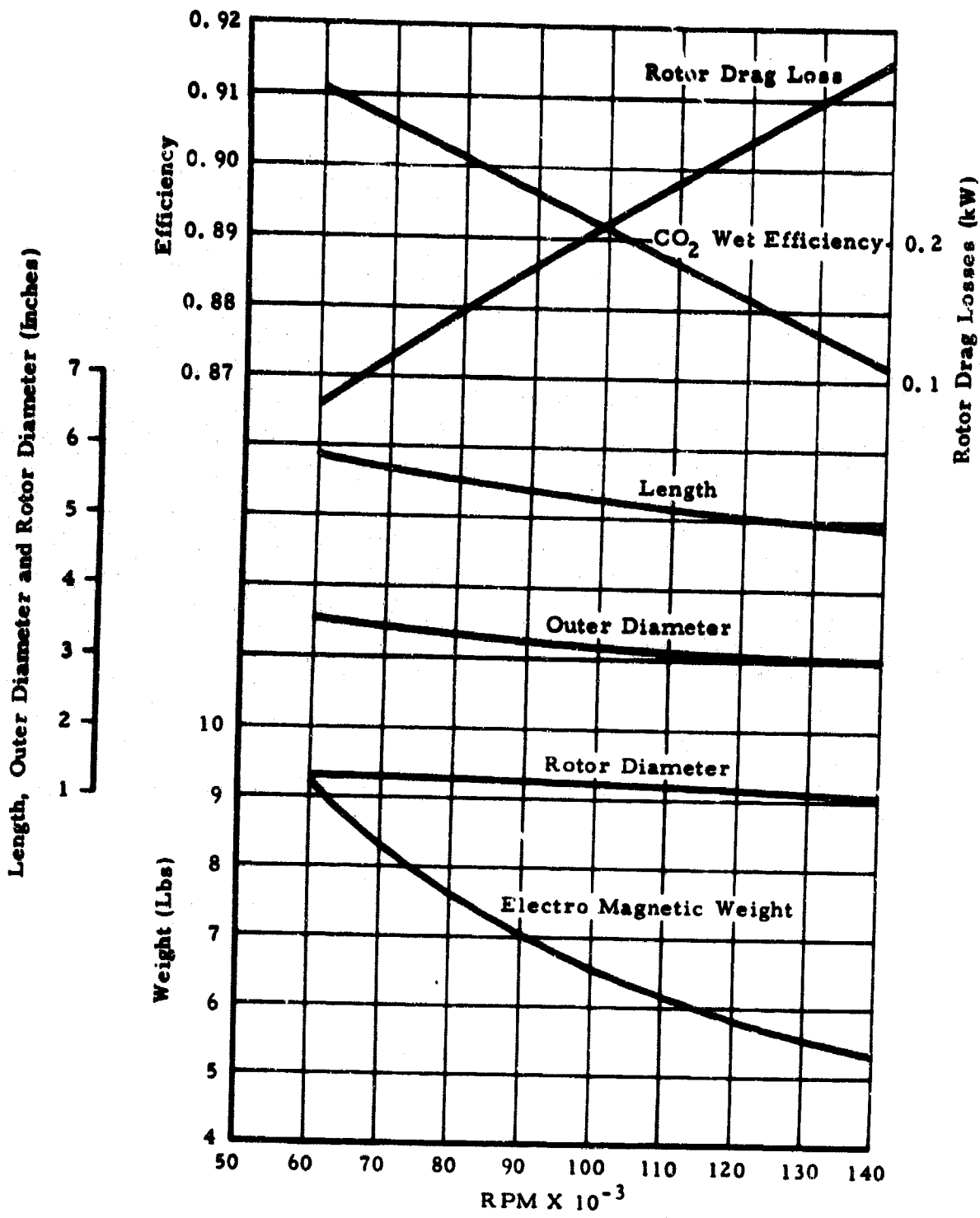


Figure 27. Parametric Data 5.5 kW Nadyne 2 Pole

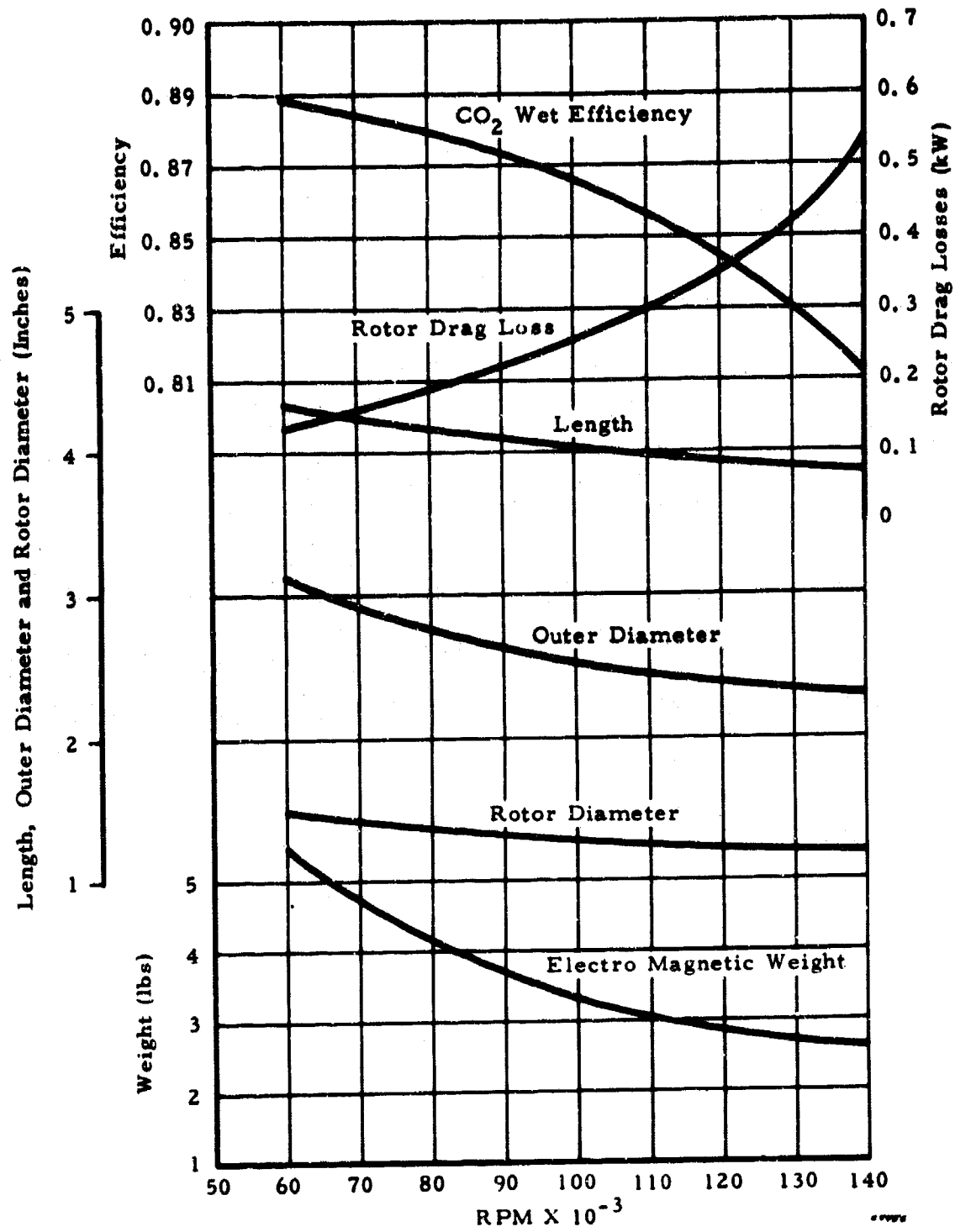


Figure 28. Parametric Data 5.5 kW Nadyne 4 Pole

c. Selected Preliminary Design

Figure 29 is a detailed layout of the preliminary 10 kW Nadyne alternator. The alternator is extremely compact. The length is 5.06 inches with an outside frame diameter of 6.5 inches and a total weight of 21.76 pounds. It was designed for a three phase 115 volt line-to-neutral output with a .9 power factor. A 2-pole machine was selected for maximum efficiency and rotor structural integrity. The rotor diameter flux densities and current densities and several other parameters have been selected as a result of extensive computer studies of hundreds of configurations to establish the optimum machine. Table XII is a tabulation of machine rating and performance parameters.

(1) Configuration Analysis

A weight breakdown of the preliminary design is given in Table XIII. It was established by McDonnell Douglas that the length of the alternator rotor should be as close to 5 inches in length as possible in order to avoid passing through a critical speed during acceleration to full load. The design procedure was to decrease the axial length of the field coil but maintain the same cross sectional area by increasing its mean turn length. As a result, the field poles, stator iron, and field coil weights were increased from the conventional Nadyne design. It should be noted that the tabulated weights are a compromise selection which may be altered during the final design of Phase II.

(2) Efficiency and Loss Analysis

The preliminary alternator design has been selected by computer analysis of hundreds of configurations varying all important parameters to achieve the maximum efficiency. Essentially, the design provides a small diameter short rotor with a completely smooth cylindrical surface to minimize the CO₂ drag losses. The small stator inside diameter and short stator stack provided lowest practical mean stator turn length to minimize the stator coil resistance. The shorter, larger diameter design allowed the stator back iron (yoke) area to be increased thus reducing the yoke flux density to provide the lowest practical eddy current and hysteresis losses. Finally, rotor pole face losses were minimized by utilizing semi-closed stator slots.

These provisions have resulted in the computed loss breakdown shown in Table XIV and a computed full load efficiency of slightly over 90 per cent.

(3) Fabrication and Material Selection

(a) Rotor Construction

The magnetic sections of the rotor will be fabricated of high strength high magnetic permeability steel. The interpolar or nonmagnetic section of the rotor will be fabricated from high-strength nonmagnetic material. The magnetic and nonmagnetic parts of the rotor will be machined

TEXT NOT REPRODUCIBLE

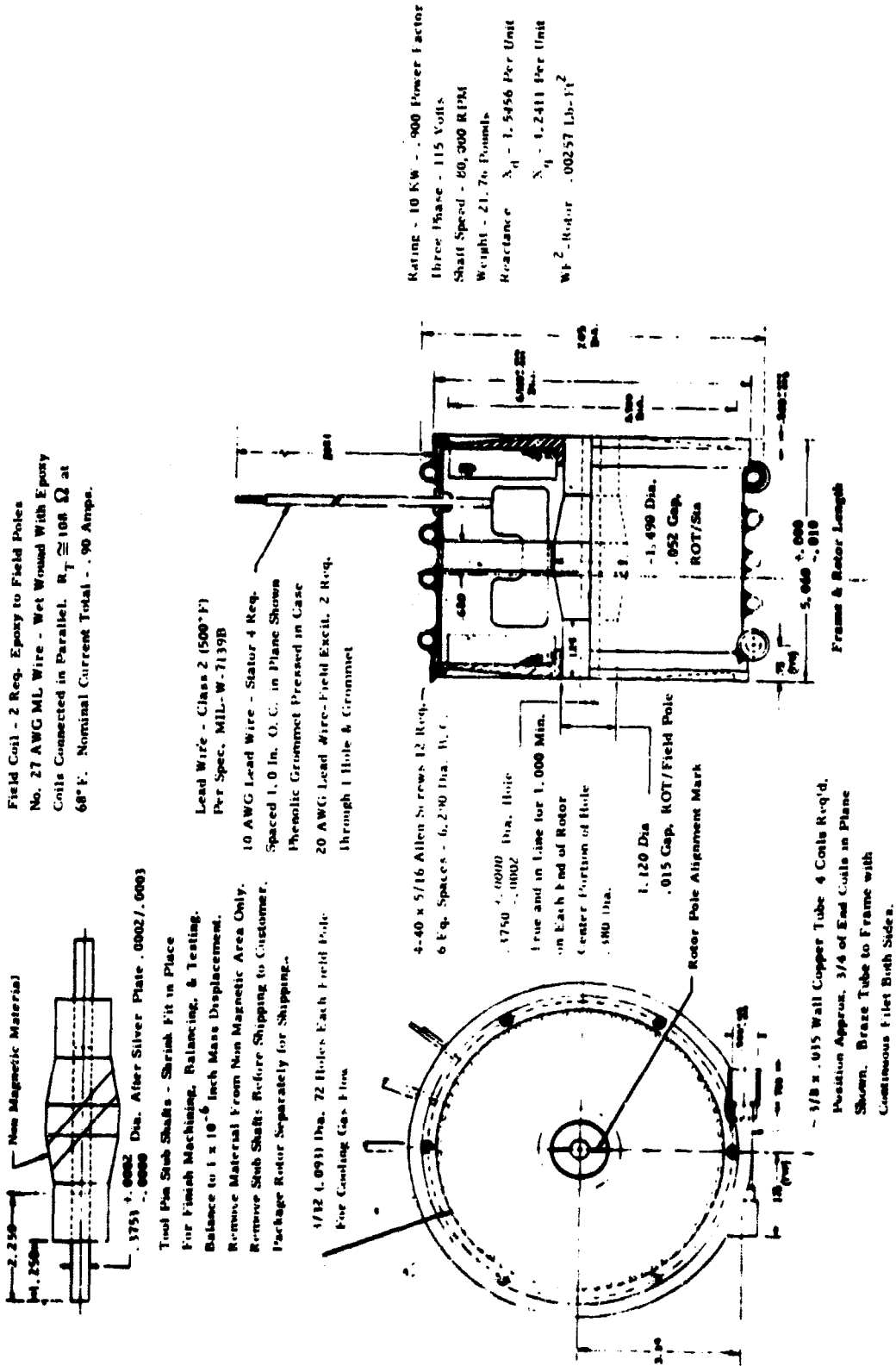


Figure 29. Generator - 10 kW Nadyne 80,000 RPM, 2 Pole

TABLE XII. MACHINE RATINGS AND PERFORMANCE PARAMETERS

Kilowatts	10
Voltage (RMS, L/N)	115
Current (RMS per phase, amps)	32.21
Frequency (Hz)	1333
Speed (RPM)	80,000
Phases	3
Poles	2
Power Factor	.9
Rotor Diameter (inches)	1.49
Frame Diameter (inches)	6.5
Length (inches)	5.06
Stator length (inches)	.63
Number stator slots	24
Rotor WK^2 (lb-ft ²)	.0025

TABLE XIII. WEIGHT BREAKDOWN

Frame	2.61
Stator	4.09
Rotor	1.60
Field Poles	3.24
Stator Coil	2.30
Field Coil	4.75
Cooling Tubes	2.75
Lead Wire	0.42
Total	21.76 Pounds

TABLE XIV. LOSS BREAKDOWN

Stator I^2R	.2959
Field I^2R	.1529
Stator Iron	.2295
Rotor Pole Face	.0126
CO ₂ Drag	.3150
Stray Load	.1000
	1.1059 KW

Efficiency = .9004

separately and intermeshed to form the complete rotor assembly. The individual parts will be bonded together by a proprietary high-strength bonding technique developed by North American Rockwell Corporation during a 2-year period. After bonding, the rotor will be machined and a .375 inch diameter hole will be bored axially through the center of the rotor as shown on the drawing of Figure 29. North American Rockwell will then shrink fit the rotor to a shaft. The rotor will then be precision dynamic balanced to 1×10^{-5} inches mass displacement for in-house testing. North American Rockwell's rotor shaft will be removed upon delivery of the alternator to McDonnell Douglas Corporation. It should be noted that the rotor shaft to be supplied by McDonnell Douglas Corporation may unbalance the rotor slightly and should therefore be corrected by balancing the entire system as a unit prior to testing at McDonnell Douglas Corporation. Note that after bonding of the individual parts, the rotor becomes symmetrical and the homogeneous mass is inherently balanced and cannot change during the life of the alternator.

The most critical aspect of the rotor construction is the bond between the magnetic poles and the nonmagnetic interpolar elements. Rotor strength characteristics depend completely on this bond and its integrity is vital. The study drew on the wealth of knowledge in metallurgy and structural fabrication available at North American Rockwell. Trial bonds by a number of different approaches have been evaluated and tested. Mechanical joining "trees," bolts, and stress bands have been studied and set aside as being unsatisfactory from either a strength or practical cost viewpoint. Brazing and casting methods have been abandoned because of insurmountable void problems. However, the approach finally selected has been highly successful in producing void-free high strength joints at a low cost. Although the materials and techniques used are proprietary, it can be stated that the joint results from an interdiffusion of material between the magnetic and nonmagnetic materials. The resulting bond is as strong as the weaker of the original materials and takes on the stress strain relationship of that material including its yield point. The composite material, once joined, can be heat-treated in a normal manner and again follows the heat treat characteristics of the weaker material. The structural characteristics of the bond have been established by structural specimen tests. Specimen tests have shown 0.2 offset yield points of 48,000 psi and ultimate tensile values of 96,000 psi in the annealed condition. Ultimate fracture usually occurs in the weaker material near the joint, but the joint itself does not exhibit an intermaterial fracture. The composite material is ductile and generally exhibits characteristics of the more ductile material.

(b) Rotor Material

Three candidate rotor materials have been investigated for the preliminary Nadyne alternator design, 4130, Silicon steel, Hiperco 27 Cobalt steel, and Hiperco 50 Cobalt steel. The importance in minimizing the rotor diameter to reduce the rotor drag losses is apparent from the previous sections. In order to minimize the rotor diameter and still carry rated flux in the rotor, the material must be capable of handling the maximum flux density permissible. It is evident from Figure 30 that Hiperco 50 is by far superior to any other magnetic material for maximum flux density capability,

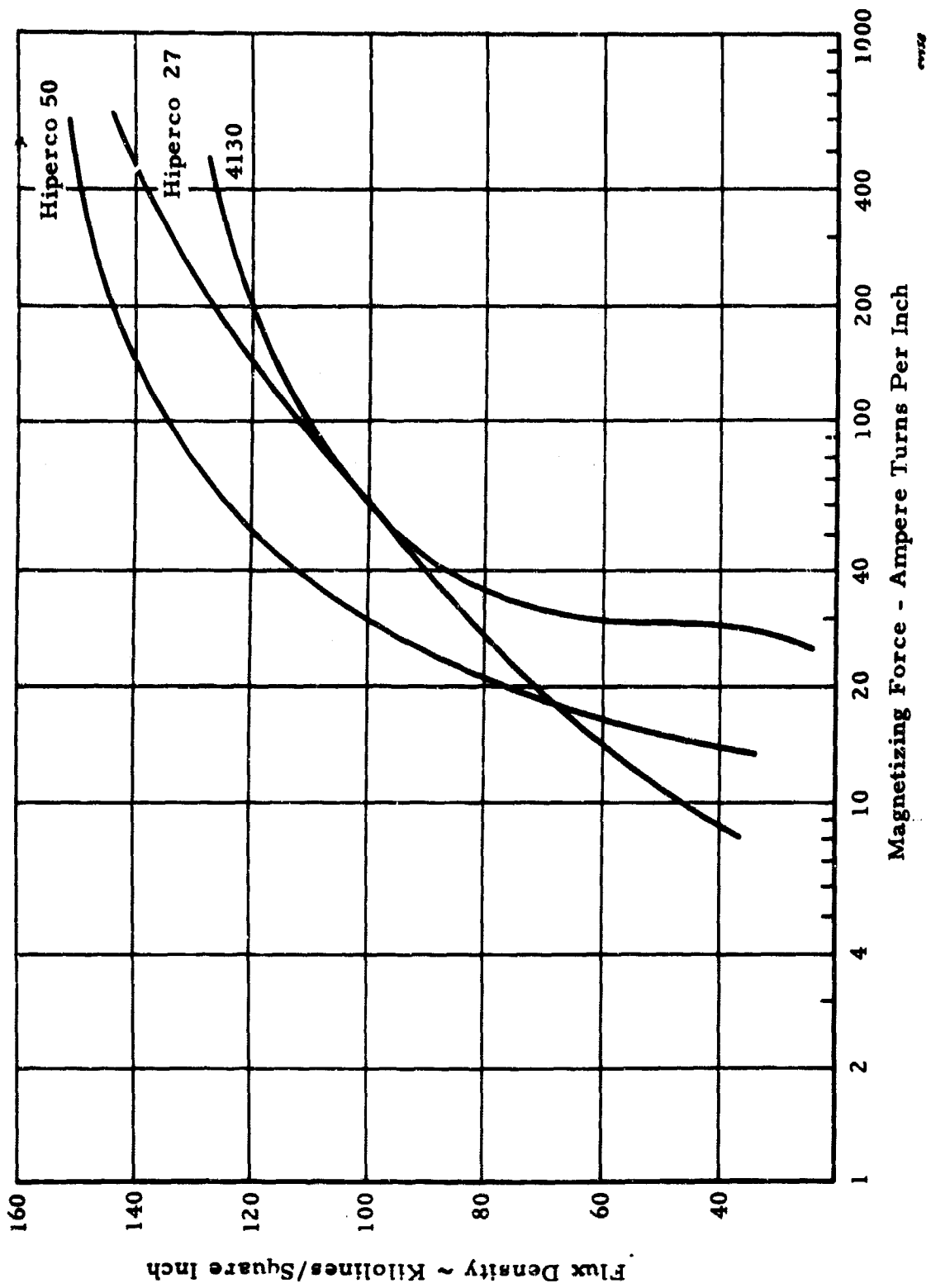


Figure 30. DC Magnetization Curves at Room Temperature

however, it was not selected, because of its inability to withstand the temperatures required during bonding the rotor. It is basically a two phase material which when heated above its second phase heat treat temperature, loses its high flux density capability.

Hiperco 27's magnetic properties however, are not affected by the high bonding temperatures and has therefore been selected for this application.

Hiperco 27, contains 27% cobalt and 1/2% chromium, in a soft magnetic alloy, which offers a high magnetic saturation value, high Curie temperature and greater ductility than normally associated with this alloy system. The addition of cobalt to iron raises the magnetic saturation value from 21,500 Gausses to 22,600 Gausses. The increased ductility of Hiperco 27 not only allows more conventional manufacturing processes to be used, but greatly facilitates bonding techniques. Rene 41 has been selected for the non-magnetic rotor material since it provides good strength and excellent physical properties for bonding to Hiperco 27.

(c) Frame and Pole Pieces

Both the frame and pole pieces are also to be made entirely from Hiperco 27. This high flux density material was selected for the field pole to minimize its cross sectional area adjacent to the rotor end diameter. Minimizing this area is necessary in minimizing the CO₂ drag losses occurring in the field gaps. This will also be fabricated of Hiperco 27 to provide high flux density capability.

(d) Stator Core

The stator core shall be fabricated with Hiperco 27 strips of .004 inch thickness to minimize the iron loss at the 1333 Hz design frequency. In addition, the high flux density capability of Hiperco 27 provides favorable stator tooth and slot geometries necessary in minimizing the stator slot leakage reactance.

(e) Cooling Coils

The cooling coils are to be made from copper and brazed to the frame by standard techniques.

(f) Insulation System

A basic Class H insulation system of ML magnet wire and glass mica will be employed in the stator windings and the field coils. The insulation system will consist of the following:

Magnet wire:	copper insulated with ML varnish
Slot liner:	glass mica
Winding separators:	glass mica

Coil ties: untreated glass tape
Encapsulation: ML varnish
Lead wire: per MIL-W-7139B

d. Thermal Analysis

A preliminary thermal analysis was performed to establish the philosophy to be used in controlling the temperatures. The losses within this alternator, although low as a percentage of output power, are quite appreciable compared with the small volume of the machine (about one tenth cubic foot). Also, the environment of the Nadyne is quite unusual since it is surrounded by carbon dioxide at 1825 psi and 300°F. These differences from conventional machines cause previous cooling experiences to be inadequate. The preliminary thermal analysis was performed as a substitute for this missing experience.

The specific aim of the analysis was to answer two questions - (1) Will a liquid cooling system be necessary to keep temperatures within limits? (2) Can internal cooling be accomplished with a reasonable flow of carbon dioxide?

In summary the following conclusions were reached:

1. Internal temperatures are quite uniform and satisfactorily low due to high convective coefficients.
2. The amount of carbon dioxide needed for internal cooling appears to be reasonable (about 0.05 pounds per second).
3. The external liquid coolant appears to be superfluous if the flow of the internal coolant (CO₂) is maintained sufficiently high, e. g., 0.05, to 0.10 pounds per second.
4. Elimination of the external coolant should be accompanied by thermal insulation or by other means of preventing or accounting for the heat which would otherwise enter from the external environment.

These are further discussed in the following paragraphs.

(1) Analytical Method

The tool used in this analysis was a computational program written specifically for a Nadyne machine, which contains scaling relations which permit varying the size of the machine.

(2) The Computational Program

The computational program was written for the IBM-360-65 digital computer. Heat balance equations are written for thirty principal elements within the Nadyne. These equations consider the electrical and

magnetic losses that occur at each particular location as well as the conductive, radiative, and convective coupling to each neighboring element. The heat transfer coefficients vary as functions of temperature and pressure where applicable. The appropriate areas for use with each coefficient are computed from a series of basic dimensions which are included in the input data for any particular machine. Provisions are made (1) for putting a gaseous coolant through the interior of the machine, (2) for a liquid coolant on the exterior, (3) for cooling by convection and radiation to the ambient, and (4) for cooling the ends of the rotor with lubricating oil. The resulting temperatures are determined by a method of relaxation.

(3) Limits of Applicability

1. The program has not been thoroughly checked-out for this regime of very high pressures.
2. No provision or account was made of the possible flow of hot gas through the center of the rotor.
3. The reported temperatures resulted from approximate but incomplete convergence of the relaxation method.
4. The maintenance of the temperature of the outer cylindrical casing (T7) was not examined in detail.
5. The end plates have radiant interchanges with objects both hotter and colder than the single environmental temperature used.
6. Flow was not considered through the clearance between the rotor and the end plates.

These factors, when examined in more detail would permit removal of the above restrictions.

(4) Input Data

Dimensions, electrical losses and other data for the alternator were taken from the printout of the results of the optimization program. This study is reported elsewhere in the report. Where dimensions have been varied slightly for practical considerations, the values from the drawings were used.

Temperatures and pressures of both the environment and the internal coolant were furnished by Mr. Ed Brass of the McDonnell Douglas Corporation.

e. Results

(1) Variation of Internal Coolant Flow

Figure 31 shows the temperatures which result from varying the flow of the carbon dioxide used as the internal coolant. Identification of the

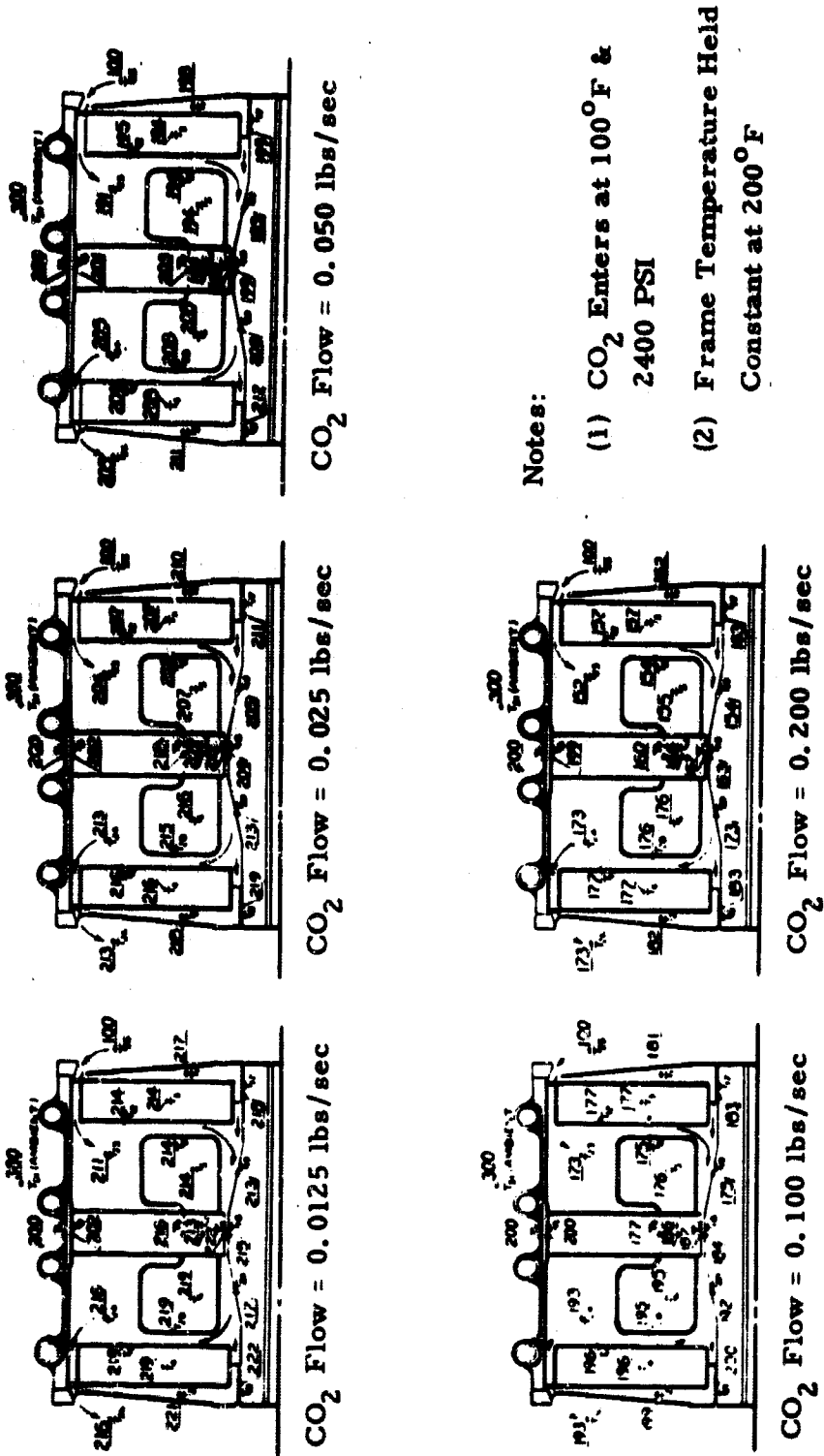


Figure 31. Temperatures (°F) Resulting From Various Flows of Carbon Dioxide

various parts of the alternator can be made by consulting the drawing shown in Figure 29 and from which this sketch was derived. The larger numbers are the temperatures in degrees Fahrenheit. Their locations are labeled with subscripted T's to facilitate cross-references. These locations are both specific and general. For instance, T5 and T6 are the bulk mean temperatures of the bundles of end turns, while T27 and T28 are their mean surface temperatures.

The temperatures shown in Figure 31 are quite uniform and well within the usual temperature limits of the materials. This is attributed to the high convective coefficients that result from both the high pressure (2400 psi) and the high rotational speed (80,000 rpm).

The two internal CO₂ temperatures, T23 and T24, are somewhat deceptive, as they were computed after they have absorbed their heats from the various components. In this regard, they can be considered as the coolants' temperatures as they leave their respective halves of the alternator.

The CO₂ absorbs much more heat in the upstream or right-hand chamber than it does in the downstream or left-hand chamber. Notice the relative increments from T25 to T23 and from T23 to T24. This phenomenon is attributed to two influences: (1) the leakage of heat from the hotter downstream chamber into the cooler upstream chamber, and (2) the transfer of heat from the liquid to the gaseous coolant. Of these, the latter is the more important. The potential for this transfer is much greater in the upstream chamber, as the carbon dioxide is entering at only 100°F and the frame is being held at 200°F by the liquid coolant. When the carbon dioxide reaches the downstream chamber, it is already about as hot as the frame, and the potential is much reduced. This phenomenon raises the question of the interrelation of the various coolants.

Figure 32 shows the heat flows to or from the composite machine. These include: (1) the heat to the external or liquid coolant, (2) the heat to the internal or gaseous coolant, (3) the heat to the ambient by radiation and convection from the end plates, and (4) the total of the other three. This total plots as a horizontal line in the fourth quadrant in accordance with the fact (from the first law of thermodynamics) that the net cooling must be equal and opposite to the electrical dissipation. Figure 32 is plotted in accordance with the familiar thermodynamic convention of heat into the machine being represented as positive and heat out (i. e., cooling) being represented as negative.

The curve for the external coolant becomes positive at a flow rate of about three pounds per minute or 0.05 pounds per second of carbon dioxide. As this curve extends upwards into the positive quadrant, the curve for the internal coolant must plunge farther into the negative quadrant in compensation. This trend leads to the superficial conclusion that the external coolant is doing more harm than good at the higher flows. The word "superficial" is used because Figure 32 does not tell the complete story. The external coolant also protects the machine by absorbing heat from its 300° environment as well as from its internally generated heat. The conclusion would be valid if the cooling jacket were replaced by a perfect thermal insulator.

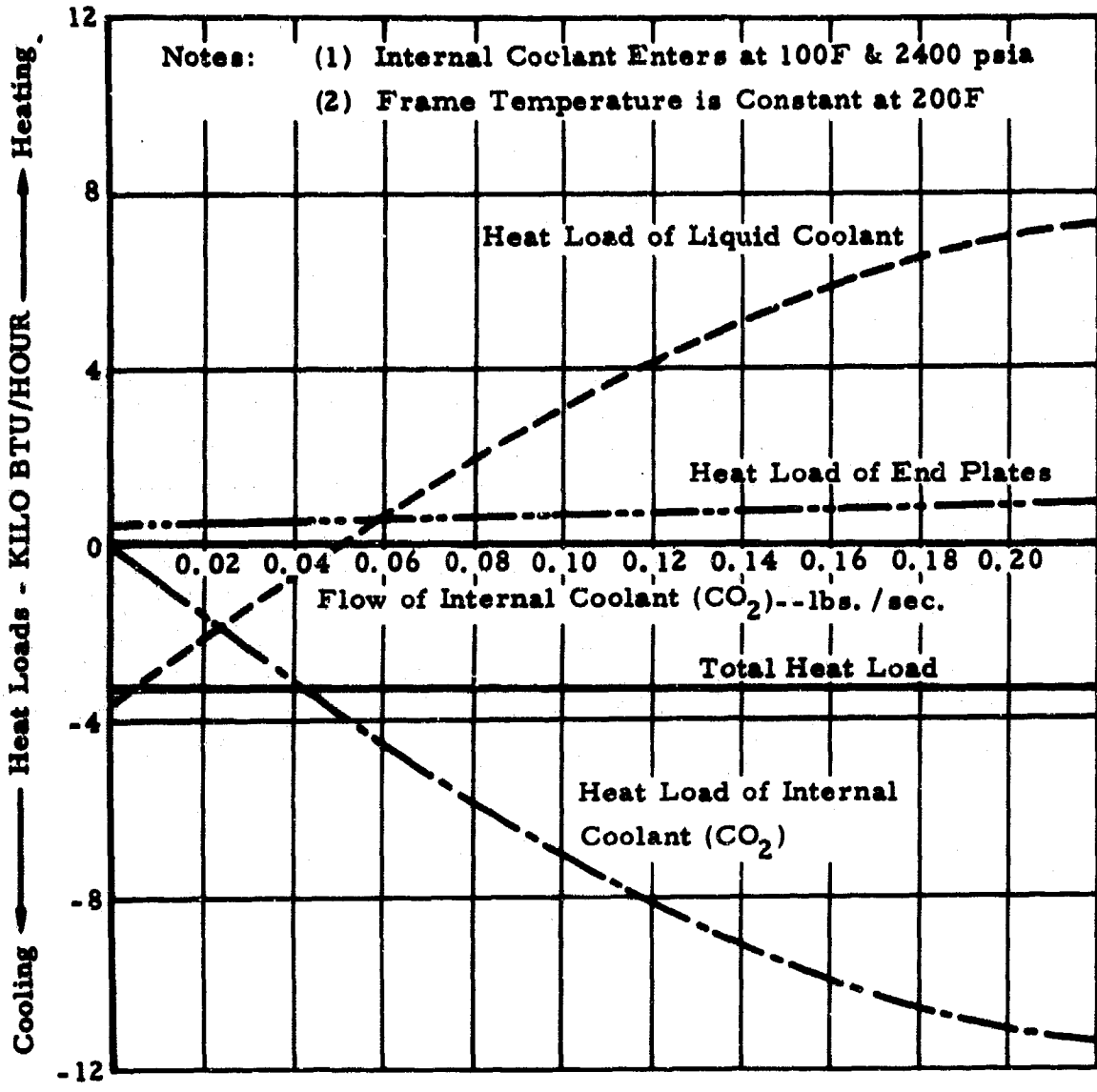


Figure 32. Effect of Flow of Internal Coolant (CO₂) on Heat Loads

If this were done, the temperature of the casing, T_7 , would adjust itself to the internal conditions, and there would be corresponding adjustment of the temperatures throughout the alternator. The external cooling liquid does act to lower the differentials of temperature between the warm and cool ends of the alternator.

(2) Frame Temperature Variation

Figure 33 is similar to Figure 31 except that the temperature of the casing or frame is varied instead of the flow of carbon dioxide. The latter is kept constant at six pounds per minute. This value was given by Mr. Brass as the flow that would cause no great penalties to the overall system.

The temperatures are within the usual limits for materials, and they are quite uniform. Again, this trend is attributed to the high convective coefficients.

Figure 34 is similar to Figure 32 except that the frame's temperature is used as the abscissa. As the frame's temperature increases, more and more of the cooling must be done by the carbon dioxide. The net influence of the external coolant changes from cooling to heating at about 155°F . Again, the interception of heat from the environment must be considered in evaluating the value of the external coolant.

f. Alternator Test Procedure

(1) Static Tests

The tests to be performed prior to the operating load calibration tests are to be as follows:

1. Perform 500 V insulation resistance test of each winding to case and between windings.
2. Perform 1500 V, 60 Hz, dielectric test of each winding to case and between each winding.
3. Measure and record the winding resistance of each winding with a Kelvin Bridge.

(2) Load Calibration Tests

Calibration of the generator for a load will follow MIL-STD-705 method 4105.0 as modified herein.

(a) Efficiency

The efficiency of a generator is calculated as follows:

$$\text{Generator efficiency (in percent)} = \frac{\text{kW output} \times 100}{\text{kW output} + \text{total losses}}$$

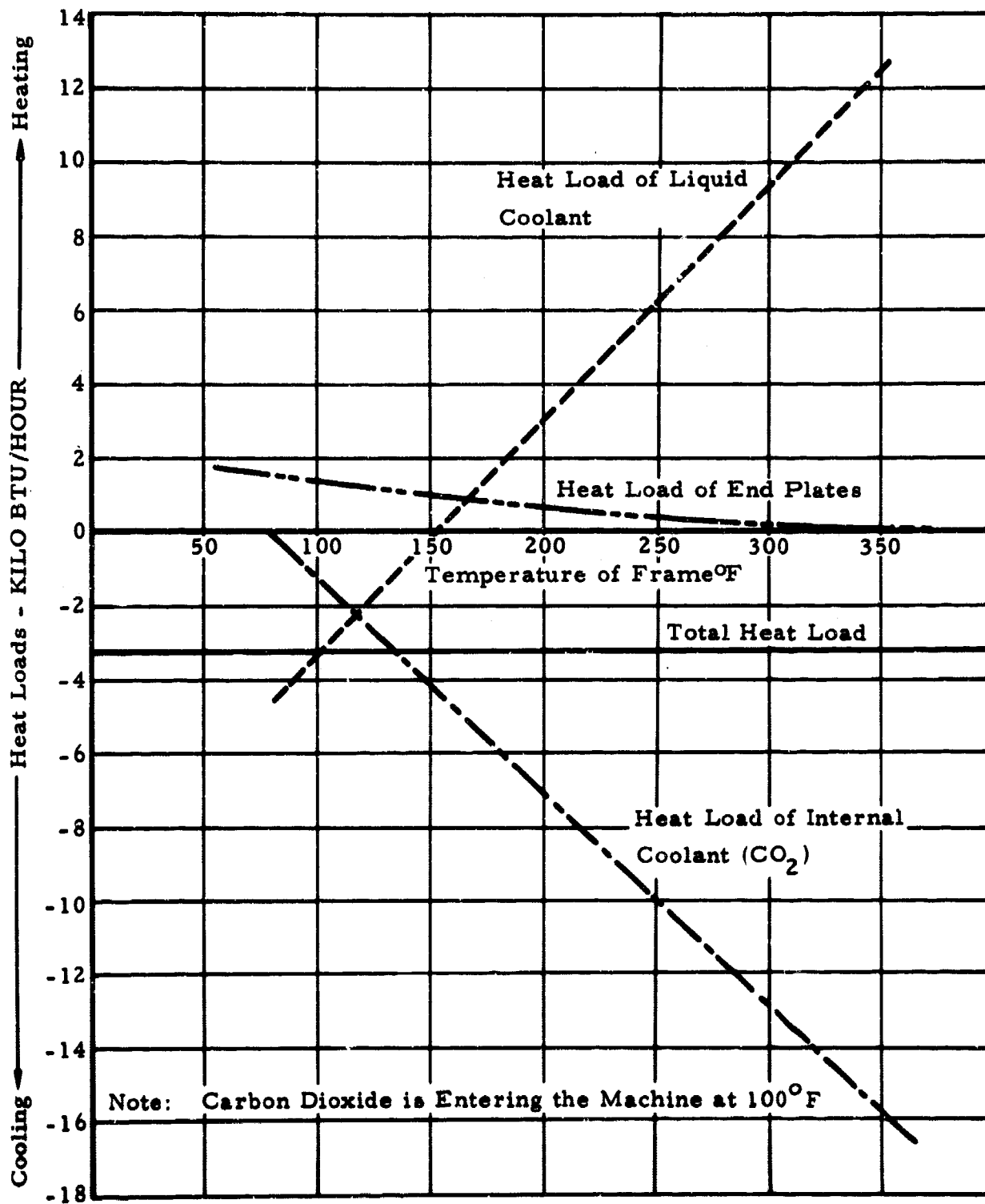


Figure 34. Effect of Frame Temperature on Heat Loads

Used as a load device, the load would be equal to the kW output plus the sum of the losses.

(b) Summing Losses

The total losses are equal to the sum of the following:

1. Bearing friction and windage loss at the rated speed.
2. Open-circuit core loss at operating voltage.
3. Armature I^2R loss at specific armature current and temperature.
4. Field I^2R loss as specific field current and temperature.
5. Stray load loss at specific armature current.

The total losses of the machine can not be measured directly. What is proposed is that the alternator design characteristics be verified and a set of curves be prepared to enable the losses to be derived through measurable electrical parameters. The alternator operating parameters, items 1 through 5, listed under the environmental load test paragraph will be sufficient to determine the load at any time. The load calibration tests are discussed in the following text.

(c) Bearing Friction

Obtained by operating the generator at speed without excitation and determining the horsepower losses. This will be accomplished by spindown tests in accordance with the following method. The rotor shall be motored to 120% of design speed by operating the NADYNE as an induction motor. A variable frequency dc to ac, 3-phase converter shall be used as the driving power supply. Upon reaching desired speed, the power shall be disconnected and spindown data taken.

(d) Open Circuit Core Loss

Obtained by driving the generator at rated speed without excitation until the bearings reach constant temperature and friction becomes constant.

By means of separate excitation, raise the applied voltage to the field to increase the field current in steps from zero to full field to give approximately 20, 40, 60, 80, 90, 95, 100, 105, 110, 120 percent of rated voltage.

Simultaneously read and record the field current, the generator terminal voltage and input to the generator for each step.

All readings must be taken with a rising field current.

From the generator input, subtract the bearing friction and windage loss to obtain the open-circuit core loss for each field current value.

Plot a curve of generator open-circuit core losses vs terminal voltage as shown in Figure 4.5.0-V, MIL-STD-705A.

The value of open circuit core loss at rated voltage shall be used in summation.

(e) Armature I^2R Loss

The armature I^2R loss is defined as the product of the square of the armature current under any specified load and the resistance of the armature at the operating condition.

The armature resistance shall be measured at room temperature with a Kelvin Bridge at room temperature and the reading corrected to 30°C. The temperature rise of the windings shall be determined at various operating conditions in the environmental tests which follow. Thermocouples imbedded in windings shall be used to sense the winding temperatures. The following formula shall be used to determine the armature resistance.

$$R_c = \frac{R_o(234.5 + T_r)}{234.5 + T_o}$$

where R_c is the corrected resistance

R_o is the measured resistance

T_r is the stabilized temperature rise ~ degrees F

T_o is the temperature of the windings at the time R_o is measured ~ degrees F.

Calculate the armature I^2R loss by squaring the armature current, multiplying by R_c obtained above, then tripling the figure for the 3-phase value.

The resistances obtained by calculation shall be compared to values obtained with a Seely Bridge.

(f) Field I^2R Loss

The field I^2R loss is defined as the product of the square of the field current under any specified load condition and the resistance of the field at the operating condition.

The resistance of the field shall be determined at various operating conditions during the environmental tests by use of the voltmeter, ammeter method.

To calculate the field resistance, divide the field voltmeter reading by the field ammeter reading. Calculate the field I^2R loss by squaring the operating field current, then multiply by the appropriate field resistance obtained above.

(g) Stray Load Loss

These losses are obtained by operating the generator short circuited at rated speed.

Adjust the excitation for approximately 125 percent of rated current. Decrease the excitation in steps to obtain approximately 100, 75, 50, and 25 percent of rated current flow in the armature.

At each of the above steps, readings of the generator current, generator input power and speed shall be recorded.

From these values, subtract the bearing friction and windage loss and the armature I^2R loss to obtain the stray load loss.

Plot a curve of stray load loss vs armature current.

(h) Environmental Load Tests

A full load heat run shall be performed at rated power factor and speed in ambient temperatures of 100°F, 200°F, 300°F, and 400°F. Instrumentation shall be provided to measure the following.

1. Input torque
2. Speed
3. Field current and potential
4. Armature output, voltage, current and watts
5. Temperature of windings, frame, bearing and ambient air (12 thermocouples)
6. Armature resistance by Seely Bridge method.

Armature and field resistance values will be established for various operating conditions to be used in determining the I^2R losses. Tests at other loads will be performed as required to determine the above resistance values.

(3) CO₂ Tests at Douglas

The alternator shall be immersed in CO₂, pressurized at 2000 psi and run at 120% of design speed to obtain spin-down data for bearing friction and windage loss data. NAA shall provide the power supply, instrumentation, and other support as required. The alternator shall then be connected to the turbine and a full load heat run made. During this test, winding temperatures shall be monitored with a Seely Bridge. Selected stator winding, core, bearing, and frame temperatures shall be monitored by the thermocouple

method. The total number of thermocouples shall not exceed 12. Alternator and pump windage and heating losses shall be calculated for the CO₂ environment.

(a) North American Rockwell Test Setup

The test setup on the NADYNE generator shall include the following:

1. Prime mover: TSC 15870
2. Gear Box: 14 hp., 8,000 RPM input, 100,000 rpm output. To be purchased as part of contract.
3. Support cradle for generator torque input determination.
4. DC to AC, 3 Φ converter; modify existing unit by paralleling transistors and replacing Zener diodes.

(b) Douglas Test Support

The test equipment provided to Douglas in support of the system test shall include a variable frequency converter for motoring turbine up to speed.

6. TURBINE DESIGN

The principal components of the turbine section are the sub-base, inner and outer scroll shells, and the exhaust diffuser center body. These components are shown in Figure 35 along with adjoining parts such as the turbine bearing housing, rotor assembly, and the pressure containment cylinder.

a. Sub-base

The sub-base will either be cast, or constructed as a weldment from several machined details, depending on comparative fabrication costs of the two methods. The material selection is strongly influenced by the need to minimize thermal strains induced at the bolted interface between the hot sub-base and the much colder turbine bearing housing. For this reason, INCO 713C or M252 bar will be used; providing a material with a low coefficient of thermal expansion and very good high temperature physical properties. Additional precautions adopted to avoid dangerous thermal strains between the sub-base and connecting components will be described under Design Integration. The primary functions of the sub-base are to support the turbine components and to duct the process fluid to and from the turbine. In addition, the sub-base will provide the only ground connection to the primary CRU structure (composed of the two bearing housings and the interconnecting housing), and will serve as the hot end closure for the pressure containment cylinder. The advantages of using a sub-base in this manner are as follows:

1. An axisymmetrical duct to the turbine inlet scroll can be provided to avoid thermal distortion difficulties that might result from a single, off-center entry.
2. The turbine discharge duct center body can be provided as a separate component thereby eliminating the need for narrow, rough surface, cast channels.
3. The external piping that joins the turbine to the heat source heat exchanger and recuperator connects to the sub-base rather than to the turbine structure proper. This will protect the close tolerance turbine components from distortion due to structural loads imposed by the piping.
4. The sub-base will afford convenient instrumentation locations to measure fluid temperature and pressures.
5. Access to the CRU components is greatly facilitated in that removal of the pressure containment cylinder exposes the entire unit without disturbing the attachment of the primary CRU structure.

b. Scrolls

The use of separate components to form the turbine inlet passage greatly facilitates the thermal isolation of this area. Furthermore, thermal and attachment strains are more manageable in these thin-walled toroidal

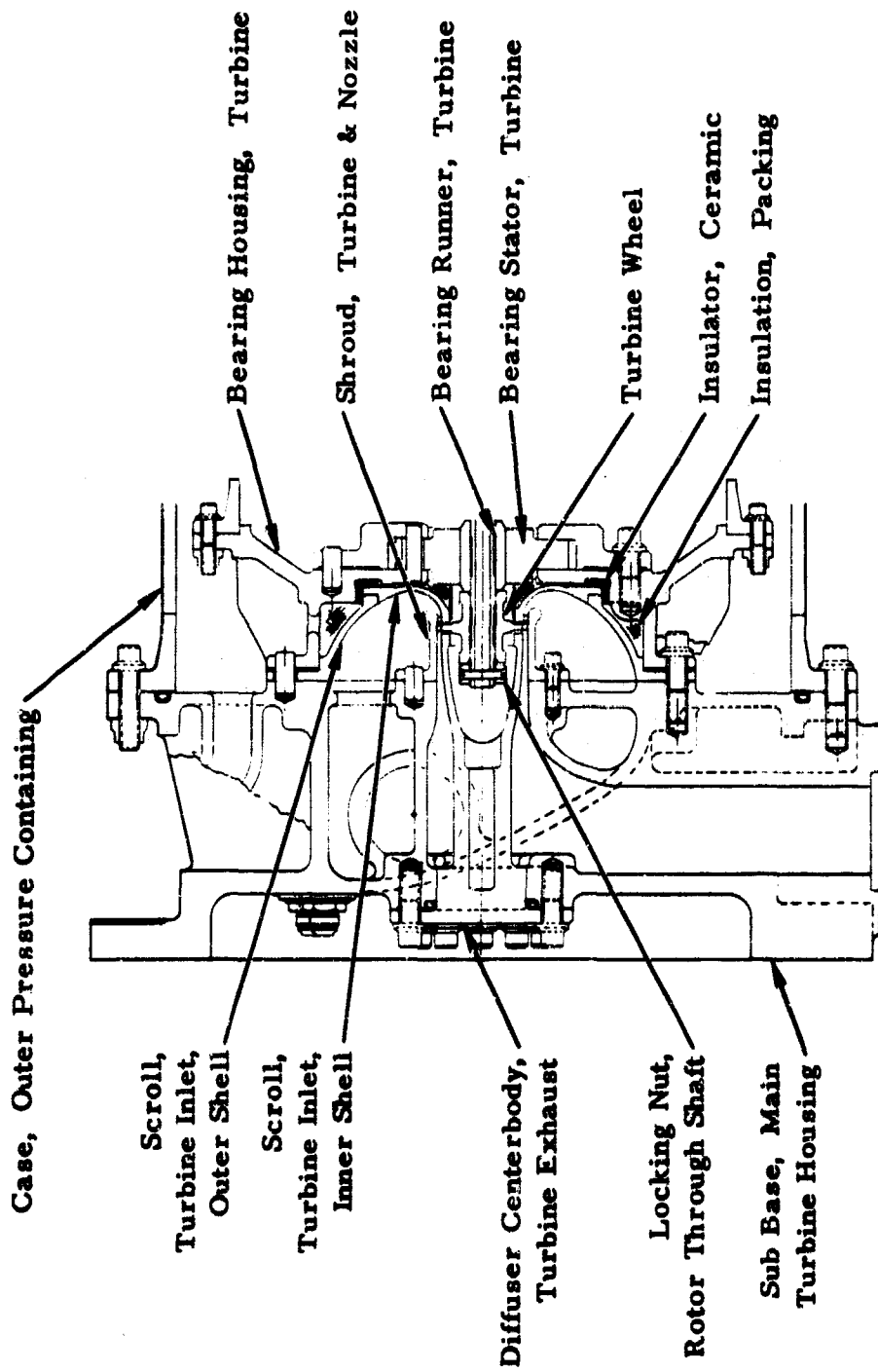
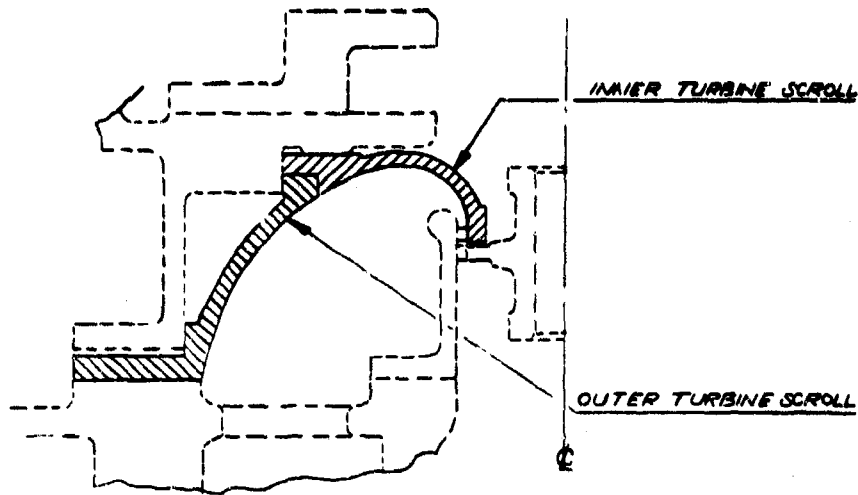


Figure 35. Turbine Section

shells. The outer shell is bolted to the sub-base at the same bolt circle that mounts the turbine bearing housing. The outer scroll contains the approximate 400 psi differential that exists between the turbine inlet and CRU ambient pressure. The small diameter end of the outer scroll is radially constrained by the turbine bearing housing. The inner scroll large diameter end is also radially constrained at this location, and is positioned axially between the outer scroll and the turbine bearing housing. The turbine nozzle vanes are electrical discharge machined (EDM) into the small diameter end of the inner scroll. The turbine nozzle outer shrouding is provided by allowing the turbine shroud to extend over the nozzle vanes. Although a slip-fit at assembly, operating pressure and temperatures will result in an interference fit-up condition between the nozzle vanes and the turbine shroud. The outer shroud will be machined from M252 bar stock to obtain the benefit of the low coefficient of thermal expansion material, particularly beneficial at the bolted attachment to the sub-base. The inner shroud will be machined from INCO 718 bar stock. The higher coefficient of thermal expansion of INCO 718 will provide the desired interference fit between the turbine shroud and nozzle vanes under operating conditions. The thermal coatings that will be applied to both shrouds will be described below under Thermal Considerations. Well known analytical methods are available for computing boundary forces, stresses, and deflections of toroidal shells. A typical procedure, with sample calculations, are shown in Figure 36.

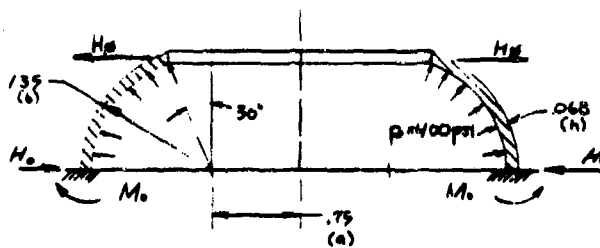
c. Shroud

The design of the turbine shroud is of considerable importance to the general problem of maintaining minimum rotor tip clearance. The shroud must be dimensionally accurate and as concentric to the rotor as possible; not just at assembly, but during operation. The turbine shroud is provided as a separate detail in order to make this component essentially expendable and easily replaced to effect a change in tip clearance. The turbine shroud is secured to the main turbine housing as shown in Figure 37. The turbine bearing support also attaches directly to the main turbine housing. The design provides the turbine shroud, sub-base and turbine bearing housing as a matched set with the final grinding of the shroud inner diameter registered directly from the turbine bearing housing. Figure 37 shows a summary of an analytical investigation into the deflections that might occur at the turbine due to forced axisymmetric deflections at the shroud attachment. Recognizing that the sub-base might undergo unpredicted thermal deflections, it is desirable to isolate that portion of the turbine shroud which is over the turbine from diametral disturbances at the attaching flange. This can be achieved by exploiting the ability of shell structures to localize forced deflections so that rapid attenuation occurs at distances removed from the loaded section. The rapidity of the attenuation is influenced by the basic physical shell properties as well as by the length of the shell. The results shown in Figure 37 were calculated from the general expressions developed by Levy (Ref. 15). The attenuation, shown as a ratio of deflection at the turbine to the deflection at the main housing attachment, is plotted vs. the shell thickness for both the fully fixed and pinned attachment circumstance. As can be seen from the curves, a shell thickness of approximately 0.07 inches will provide essentially perfect attenuation of any axisymmetrical attachment deflections in the



REFERENCES: GALLETLY "EDGE INFLUENCE COEFFICIENTS FOR TOROIDAL SHELLS OF POSITIVE GAUSSIAN CURVATURE" ASME 59 PPT 2
 GALLETLY "EDGE INFLUENCE COEFFICIENTS FOR TOROIDAL SHELLS OF NEGATIVE GAUSSIAN CURVATURE" ASME 59 PPT 3

OUTER TURBINE SCROLL



$$b/h = \frac{1.35}{.68} = 2.0$$

$$r = r/b = \frac{.75}{1.35} = .56$$

EXTRAPOLATED COEFF.			
	$E b \delta$	$E b \delta_0$	$E \delta$
M_0	.830	-.160	.6
M_1	-.25000	.830	-.6
M_2	.66	-.68	.80
M_3	-.53	-.90	.75

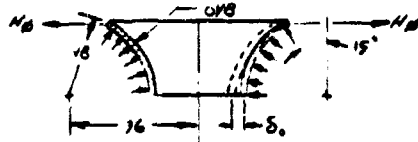
$$\begin{aligned} \therefore 830 H_0 - 25000 M_0 + 66 M_1 - \frac{9.3(400)(1.35)^2}{2} &= 0 & M_0 &= 1.23 \frac{p b^2}{17} \\ -160 H_0 + 830 M_0 - 6.8 M_1 - \frac{60(400)(1.35)^2}{2} &= 0 & H_0 &= 3.04 \frac{p b}{17} \\ 6 H_0 - 6.8 M_0 + 80 M_1 - \frac{17.5(400)(1.35)^2}{2} &= 0 & M_1 &= .80 \frac{p b^2}{17} \end{aligned}$$

$$\left. \begin{aligned} M_0 &= 1.23 \frac{p b^2}{17} \\ H_0 &= 3.04 \frac{p b}{17} \\ M_1 &= .80 \frac{p b^2}{17} \end{aligned} \right\} \begin{aligned} \sigma_b &= \frac{6(1.23)}{(.068)^2} = 1600 \text{ PSI} \\ T &= \frac{90}{.068} = 1030 \text{ PSI} \end{aligned}$$

O. B. A. DENOTES MARVELL "PARTS"

INNER TURBINE SCROLL

CHECK THE RADIAL DEFLECTION OF THE TURBINE NOZZLE:



$$b/h = 10 \quad r = 2$$

	$E b \delta$	$E b \delta_0$
M_1	-.97	-.35
M_2	-.400	.26

$$M_0 = \frac{400(400)(.48)^2}{2(.97)} = 190 \text{ lbs/inch}$$

$$E b \delta_0 = \frac{26(400)(.48)^2}{2} - 190(.35) = 1800 - 66.5 = 1733.5$$

$$\therefore \delta_0 = \frac{1733.5}{30 \times 10^4 (.48)} = 0.00037 \text{ inches} \leftarrow \text{negligible}$$

Figure 36. Turbine Scroll Analysis

TEXT NOT REPRODUCIBLE

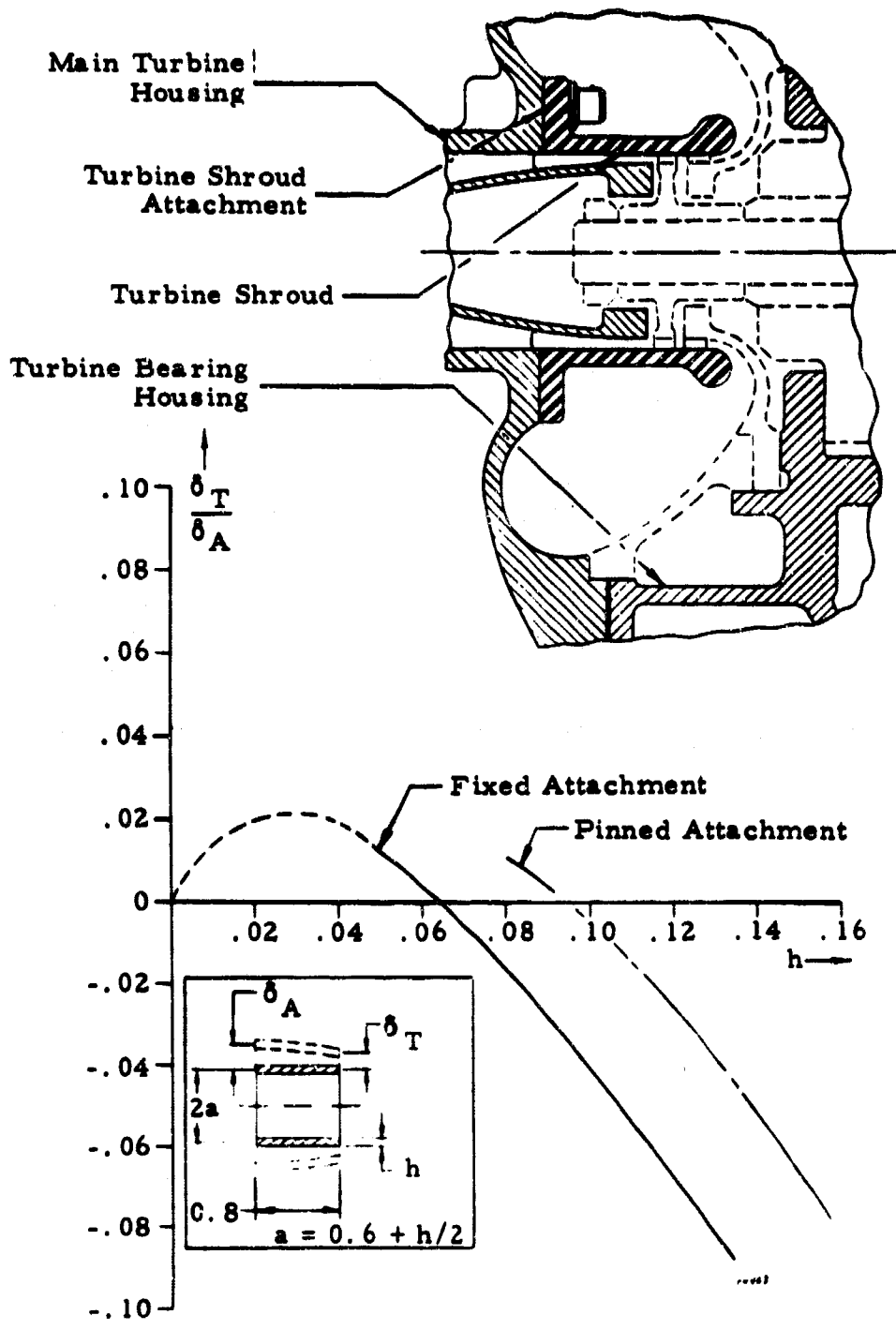


Figure 37. Turbine Shroud Deflection

vicinity of the turbine. Considerable care will be necessary to ensure that the main turbine housing will be free of all circumferential thermal gradients which would result in a rotation of the turbine shroud attachment structure. With this in mind, all turbine components have been made as axisymmetric as possible. The shroud will be machined from M252 bar stock.

d. Thermal Considerations

The general problem of preventing large heat flux losses from the turbine section is greatly eased by the compactness of the Supercritical (Feher) cycle components. The surface area of the inlet scroll and shroud is perhaps 10 to 15% of the area of comparable components used in conventional low fluid pressure turbines of similar power class. This low heat transfer area feature makes the containment of the heat within the turbine section relatively easy to manage. The sub-base will be externally insulated so that heat losses to ambient will be virtually eliminated. The sub-base will stabilize at a temperature of about 1100°F. The heat flow into the turbine exhaust fluid is restricted by the fluid film heat transfer resistance and the use of a very low conductivity metal coating (Zirconium Oxide) on the walls of the exhaust flow channel.

Note: The Zirconium Oxide (ZrO_2) coating is a MDC-Astropower development and is being used as thermal insulation in many high temperature applications. The coating is generally applied as a sprayed-on plasma of about 75% solidity. The ZrO_2 is line stabilized with 4-5% Calcium Oxide (CaO).

The heat transfer from the turbine inlet fluid to the scrolls is inhibited by the poor conductivity of the low velocity fluid film, and the use of the ZrO_2 coating on the scrolls. The overall heat transfer coefficient is expected to be about 15 Btu/hr-ft²-°F so that for a heat flux flow rate of 200 watts, the temperature of the scrolls would be approximately 430°F below fluid temperature, or approximately 1000°F. Radiation and conductive heat flow between the scrolls and the turbine bearing housing is prevented by packing these cavities with insulation such as Johns-Manville's MINK2000. This material, with an effective thickness of 0.2 inches, has an overall thermal conductivity of approximately 1.8 Btu/hr-ft²-°F, so that if the turbine bearing housing is maintained at 450°F, the heat flow through the insulation would amount to about 20 watts. Considerably more heat transfer can be expected at the mechanical interfaces between the scrolls and the turbine bearing housing, particularly at the high unit pressure surface created at the outer scroll bolting diameter. However, the heat transfer at these junctions is restricted by using as low a clamping pressure as possible and using a ceramic insulator (Boron Nitride) between the scroll and the turbine housing. The advantages of using the ceramic insulator are that the combination of high hardness, low density and low thermal conductivity greatly restricts the heat flow across a mechanical interface (Ref. 16). Furthermore, two mechanical interfaces in series result from the use of the insulator. The effectiveness of the insulator will be enhanced by applying the hard ZrO_2 coating to the metal components at the contact surfaces. On this basis, the overall

heat transfer coefficient between the scrolls and the turbine bearing housing can be estimated at about 10 Btu/hr-ft²-°F. This corresponds to a heat flux rate of approximately 180 watts.

The turbine bearing housing will be maintained at 450°F by rejecting the 200 watts of heat transferred by natural convection from the turbine scrolls into the ambient process fluid surrounding the turbine housing. If the ambient fluid temperature is 250°F, and a natural convection heat transfer coefficient of 4 Btu/hr-ft²-°F is assumed, the required heat transfer area is 120 square inches. Each fin on the turbine bearing housing has a one-side area of about 1.2 square inches, so that a fin density of about 3.5 per inch of circumference is required.

In order to verify the estimated heat flux losses, (as well as component temperatures and thermal strains) all the turbine section stationary components (including the turbine bearing housing) will be assembled and instrumented. The fluid passages will be flooded with hot water maintained at a temperature of 200°F so that actual heat transfer coefficients can be established.

e. Turbine Flow Losses

The cavity behind the turbine inner scroll will be charged by the pressure that exists downstream of the nozzle. This pressure is nominally 1950 psi but will likely be somewhat less due to the centrifugal pumping action of the rotor operating against the end of the scroll. This cavity will also receive leakage from the turbine bearing hydrostatic loading pocket which will be maintained at about 2100 psi. In order to keep the bearing fluid leakage from entering the turbine flow channel, the cavity will be vented to the CRU ambient (1850 psi) so that the cavity pressure will remain slightly below 1950 psi.

7. PUMP DESIGN

The major components of the pump section are the rotor, diffuser, and rotor seal. In addition, the pressure container end closure and the pump bearing support are used to provide the pump porting, as well as the pump diffuser discharge plenum chamber. The pump components, ports, and plenum chamber are identified in Figure 38.

a. Rotor

The pump rotor is made integral with the rotor through-bolt by welding the machined pump detail to the hollow shaft, after which the through-bolt pilot diameters are finish ground and polished. The integral pump shroud is electron beam welded to the pump vanes. The pump rotor assembly will be fabricated from Ti-6Al-4V alpha-beta alloy. The main advantage of using this alloy for the pump rotor is that the extremely low thermal conductivity of the alpha-beta metals discourages the passing of heat flux into the pump inlet fluid and the detrimental effect on pump performance that

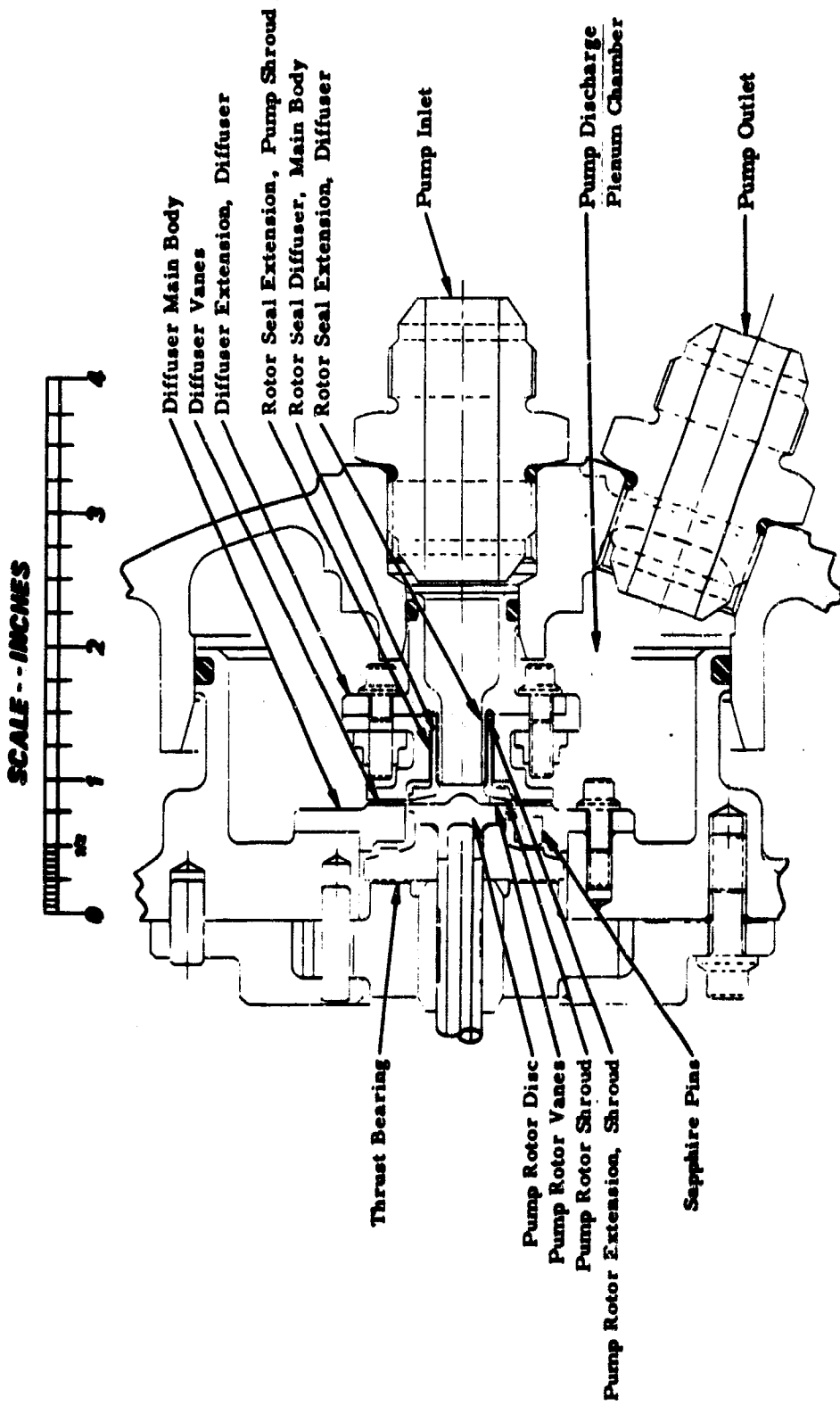


Figure 38. Pump Section

increased pump inlet temperature would have. The low modulus of elasticity of titanium is also beneficial in establishing suitable room-temperature fit-ups between the pump rotor and other components of the rotating assembly which are necessary to ensure proper piloting of the components at operating conditions. In addition, the rotor critical speed is higher due to the use of the lightweight titanium alloy.

b. Diffuser

The diffuser will be machined from 321 stainless steel in two sections joined together by electron beam welding the outboard extension of the diffuser to the diffuser vanes. The diffuser assembly is mounted directly to the pump bearing support with provisions for axial shimming the diffuser in order to obtain precise axial alignment of the diffuser flow channel with the pump rotor passage. The close structural coupling of the diffuser mounting and the rotor thrust bearing (see Figure 38) will serve to maintain the axial positioning control during operation.

c. Seal

The pump rotor discharge is sealed from the pump inlet by a capillary seal formed by a cylindrical extension machined integral with the pump rotor shroud which sandwiches between the diffuser and a mechanically joined extension of the diffuser, as shown in Figure 38. The leakage past the seal is readmitted at the pump inlet parallel to the normal flow so that direct and secondary losses from the leakage are minimized. If the average clearance on each side of the rotating cylinder is 0.0006 inch, and an eccentricity of 0.0003 inches is assumed, the leakage through the seal, Q , is as follows:

$$Q = \frac{\Delta P \pi R h^3}{6 \mu (2L)} \times K_{\text{eccentricity}} = \frac{240 (\pi) (.2) (.0006)^3}{6 (8.5 \times 10^{-9}) (2 \times .5)} \times 1.375$$

or, approximately 2.5% of the total pump volume flow.

The viscous drag loss in the seal is

$$M = \mu r A \frac{V}{h} = \frac{8.5 \times 10^{-9} (.2) (2\pi) (.2) (2 \times .5) (2\pi) (.2) (80,000)}{60 (.0006)}$$

= 0.006 in-lbs, so that,

$$\text{power loss} = \frac{MN}{63,000} \times 746 = \frac{0.006(80,000)}{63,000} \times 746 = 5.6 \text{ watts}$$

The only path from the pump rotor discharge to ambient is through the thrust bearing, with leakage having to flow against the centrifugal head developed by the thrust bearing fluid film. Normally, virtually no leakage would occur; however, in order to maintain the fluid film temperature at about 150°F, a small leakage through the thrust bearing is promoted by providing small radial grooves through the thrust bearing face.

Further discussion of the pump design will be found below under Design Integration with particular reference to the assembly procedure, concentricity of the pump rotor, and descriptions of the pump bearing support and the pressure container end closure.

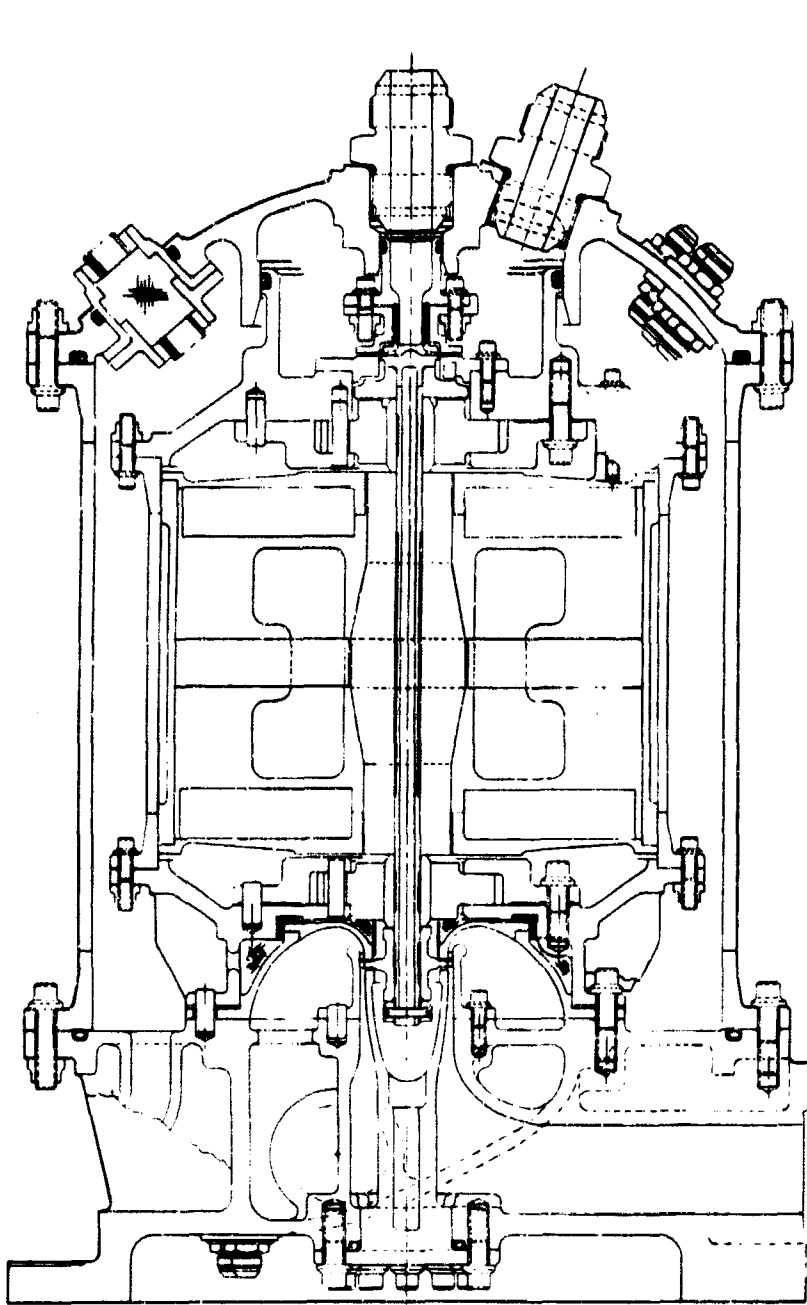
8. DESIGN INTEGRATION

a. General Arrangement

Although most of the preliminary design effort concentrated on the conventional CRU arrangement, i. e., radial bearings just outboard of the alternator rotor with the turbine and pump cantilevered from either end, other schemes were investigated. The most attractive of these other arrangements had a close-coupled turbine-pump unit (turbo pump) driving the alternator with a flexible shaft. The alternator would be mounted on oil lubricated rolling element bearings so that a high pressure shaft seal would be necessary to separate the oil environment from the process fluid. The primary advantage of this arrangement was that the turbo pump and alternator development would be completely independent of each other so that interface problems and program risk would be minimized. Furthermore, although the turbo pump would use process fluid bearings, the design of the bearings would be greatly facilitated by the lighter turbo pump rotor compared with the CRU rotor. The principal drawback to the turbo pump approach was that the test configuration would not be an optimum arrangement for an operational unit. This presented the distinct difficulty of applying test configuration results to the conventional CRU construction, thereby decreasing the utility of the proposed test evaluation program. After consulting with the AF Project Office, a decision was made to proceed with the conventional CRU arrangement as shown in Figure 39. Major components are identified in Figure 40.

The alternator rotor is supported by radial bearings located just outboard of the alternator assembly. The turbine and pump are cantilevered from either end. The CRU is mounted on a sub-base that in turn, is attached to the permanent facility structure. The rotor centerline will be vertical with the turbine end of the machine up. The vertical installation is desirable in that the radial bearings will be unloaded at start-up; and the rotor will be free of the normal thrust bearing reaction surface, resting against sapphire pins provided for this purpose. Furthermore, the vertical installation will prevent natural convective heat transfer from developing objectionable circumferential thermal gradients in the components. Locating the turbine end up will help in containing the turbine section heat flux in the hot section of the unit.

The CRU is enclosed by a cylindrical shell, which in combination with the sub-base and end closure, contains the CRU ambient pressure of approximately 1850 psi. At the pump end of the CRU, the pump bearing housing is "O" ring sealed to the end closure to form a pump discharge plenum, and the pump inlet passage. These cylindrical "O" ring seals permit axial freedom of the CRU with respect to the end closure to accommodate build-up tolerances and thermal effects.



FEMER CYCLE COMBINED ROTATING UNIT
10KWE TEST MODEL XFCTAP 01 - 01

Figure 39. CRU Layout

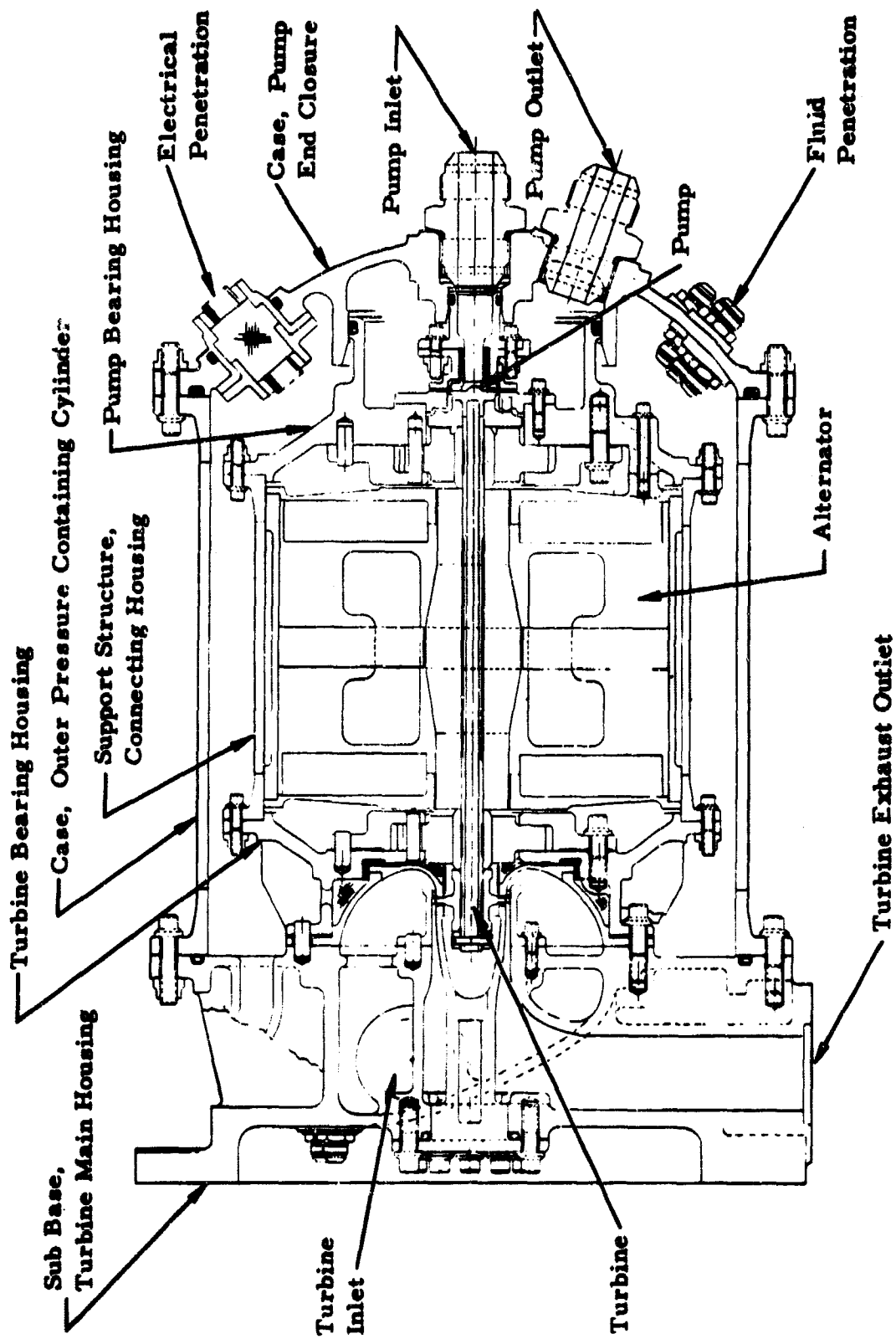


Figure 40. Feher Cycle Combined Rotating Unit
10 kWe Test Model XFCTAP 01-01

b. Principal CRU Structure

The principal CRU structure is provided by the two bearing housings, and the connecting housing as shown in Figure 41. All inertial loads will be reacted by this rigid, close-coupled supporting structure. With the exception of the pump discharge plenum, the CRU structural components do not contain significant differential pressures. However, a moderate axial load is imposed on the CRU structure as a result of the turbine inlet passage and pump discharge plenum pressure effects. The basic conical form of the bearing housings was adopted for effective handling of the axial load.

A major design difficulty exists at the attachment of the turbine bearing housing to the sub-base due to the wide temperature disparity between these two components. As previously described under Turbine Design, the bulk of the sub-base is expected to come to an equal equilibrium temperature of approximately 1100°F. This would indicate a sub-base local temperature of about 1000°F in the vicinity of the turbine bearing housing attachment. The turbine bearing housing bulk temperature is expected to be 450°F, which suggests a temperature of about 650°F at the sub-base attachment flange, since most of the 200-watt heat flux from the scroll is introduced into the turbine bearing housing at this location. In order to effect a reasonable thermal match at the attachment, a low coefficient of thermal expansion material was selected for the sub-base (M252 or INCO 713) in combination with a 302 turbine bearing housing material which provides a relatively high coefficient of thermal expansion. If more detailed analysis (using the results of the heat transfer tests) indicate that unacceptably high thermal strains will exist at this location, it will be necessary to revise the turbine bearing housing (and in particular, the fin configuration) to promote higher temperatures at the sub-base attachment flange. In addition, minor changes to the turbine bearing housing will allow for more elastic accommodation of the induced thermal strain by allowing deformation of the cylindrical portion of the turbine bearing housing that joins the sub-base attachment flange to the main portion of the turbine bearing housing. This will require changing the axial fins to circumferential fins.

The cylindrical shell that connects the two bearing housing will be at a mean temperature of about 275°F. This part will be machined from either 304 or 321 pipe. The pump bearing housing will be at an average temperature of approximately 120°F and will be machined from 302 bar stock.

c. Alternator Installation

The alternator stationary components are assembled into a single, self-sufficient structural unit. The assembly is mounted on the pump bearing housing with six bolts that axially fix the alternator. Radial constraint is provided by close-fitting the alternator outer housing within the CRU structure interconnecting housing.

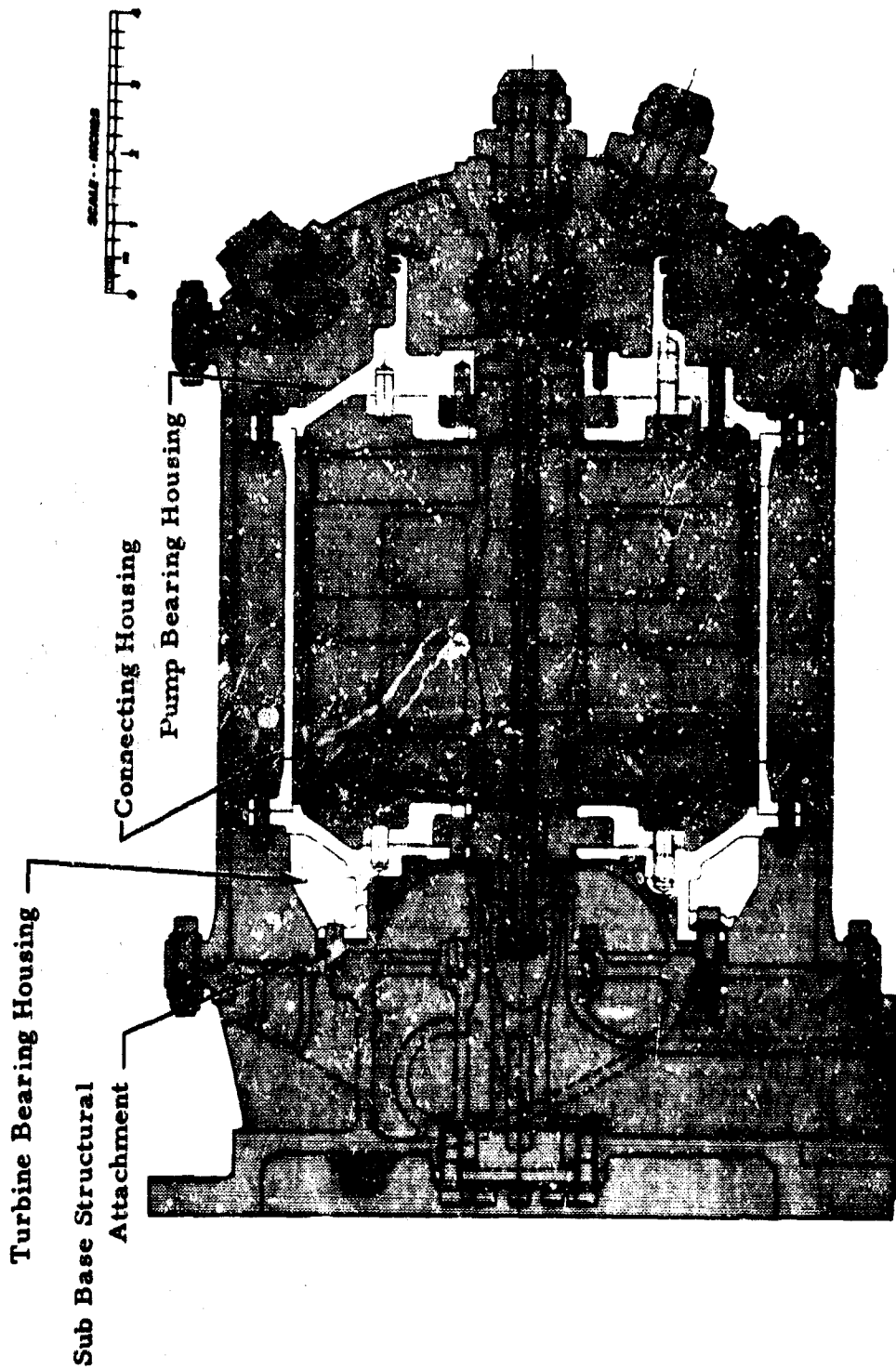


Figure 41. Feher Cycle Combined Rotating Unit
10 kWe Test Model XFCAP 01-01

d. Rotor Design

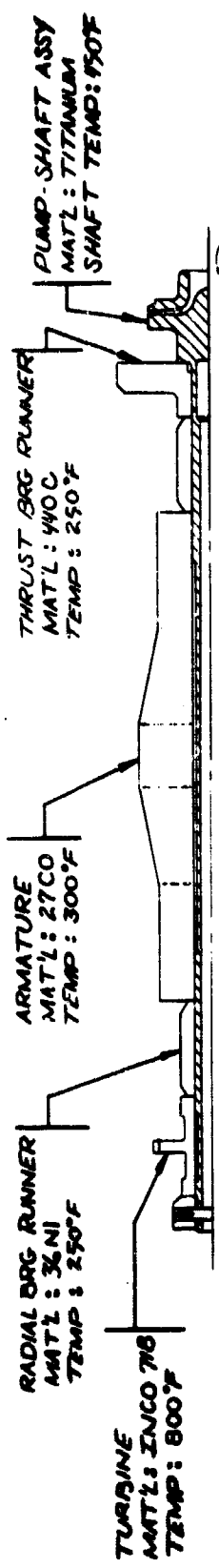
The rotor construction features a titanium through bolt made integral with the pump rotor. The thrust bearing runner, radial bearing runners, alternator rotor, and turbine rotor are assembled on the through bolt and locked in position by a shaft nut. There seemed to be a possibility at least, of using a solid alternator rotor with stub extensions from both ends on which to assemble the bearing runners, turbine and pump rotors. However, the decisive advantages of the through-bolt design include:

1. The alternator subcontractor is relieved of the problem of providing highly critical bearing and turbomachinery mounting features resulting in a much simpler inter-face definition and hardware implementation effort.
2. The radial bearings can be isolated from thermal and rotational strains in the alternator rotor, which might otherwise adversely affect the bearing performance.
3. The pump can be made integral with the through shaft thereby avoiding a difficult mounting and clamping problem.
4. The heat flow from the hot end of the unit to the pump end through the rotor is reduced by the mechanical coupling of the rotor components and the use of a thin-walled, low conductivity material, through shaft.
5. It is possible to use a very low coefficient of expansion radial bearing runner material (in conjunction with a low coefficient of expansion bearing stator material) in order to minimize the dimensional effects of off-design bearing component temperatures.
6. The use of a low modulus of elasticity material for the through shaft facilitates the use of shrink fits at assembly which will maintain interference fits under operating conditions.

A preliminary check of the rotor design was completed to establish fit-up requirements between the rotor components and the through-bolt to ensure that under operating conditions (temperature and inertial deformation) the components were in radial contact with the through-bolt, and that the axial clamp load remained sufficient to transmit the turbine torque by friction coupling of the adjoining parts. This calculation, and sample results, are shown in Figure 42.

e. Bearing Construction

The radial bearings consist of a runner which is part of the rotor assembly and a stator which is pinned to the bearing housing. In order to



SHAFT LENGTH: PRE-LOAD OF 36,700 LBS = 60,000 PSI SHAFT STRESS $\Delta L = 32,700 \times 10^{-6}$ IN
@ TEMP, NET AL = 380(5.10⁻⁶ - 180) - 730(9.10⁻⁶)(10) - 190(3.10⁻⁵)(2) - 230(5.65⁻¹⁰)(5) - 180(6.2⁻¹⁰)(6) = 1000⁻¹⁰ IN

SHAFT DIAMETER: CHANGE DUE TO AXIAL LOAD = $\frac{60,000}{16 \times 10^6} (3 \times 375) = -4.10 \times 10^{-6}$ IN
CHANGE DUE TO TEMP = $380(5.10^{-6})(375) = + 712 \times 10^{-6}$ IN
CHANGE DUE TO ROTATION = $\frac{180(10)(10)}{2(165 \times 10^3)} (375) = + 17 \times 10^{-6}$ IN

RATIO OF THE DEFLECTION X DISTANCE FROM A RADIAL PRESSURED SECTION TO THE DEFLECTION UNDER THE APPLIED PRESSURE: $\frac{1}{2} S_0 = e^{-\frac{2x}{R}} (2.07x + S_{in} 2x)$
WHERE $\frac{2x}{R} = \frac{3(9)}{(130)(0.6)} = 146$

DEFLECTION UNDER A PRESSURE $P = \frac{2(70) P \sqrt{100} (12)(91) - 2(307) P (13)(06)(12)(91)}{2(85 \times 10^3)(146)^2 (146)^2} = \frac{.191 \times 10^{-6} P}{(146)^2}$

BORE DIAMETERS:

	TEMP.	ROTATION	ROOM TEMP FIT	SHAFT HOOP STRESS	STRESSED WHEN-
TURBINE	2460 × 10 ⁻⁶	41 × 10 ⁻⁶	- 1742 × 10 ⁻⁶	76,500 PSI	NOT OPERATING
RAD DRG RUNNER	202 × 10 ⁻⁶	41 × 10 ⁻⁶	0	2,300 PSI	OPERATING
ARMATURE	488 × 10 ⁻⁶	176 × 10 ⁻⁶	0	3,000 PSI	OPERATING
THRUST DRG RUNNER	417 × 10 ⁻⁶	490 × 10 ⁻⁶	- 176 × 10 ⁻⁶	7200 PSI	NOT OPERATING

6 3087

Figure 42. 10 kWe CRU Rotor Assembly Check

minimize the effect that temperature will have on the design point bearing operating clearances, both the runner and stator will be made from very low coefficient of thermal expansion materials. The runner will be made from a 36% nickel-iron alloy (Invar) and graphite will be used for the stator. The graphite stator would also appear to have the advantage of being tolerant of momentary surface contacts in the bearing (as might occur during start-up) without resulting in seizure or serious bearing damage. The graphite stator design conditions were reviewed by the Pure Carbon Company of St. Marys, Pennsylvania. Their recommendation was to use Purebon 3310 compound. They expressed a high degree of confidence that the (dry) CO₂ environment and 500°F local temperatures will not be a problem to the graphite.

The bearing stator cannot be fixed rigidly to the bearing housing because at operating temperature, the disparity between the two coefficients of thermal expansion would produce prohibitively high thermal strains. In order to overcome this difficulty, the pins that position the stator to the housing pass through radially elongated holes in the stator as shown in Figure 43. In this manner, the radial position of the stator is closely controlled by the pins, but symmetrical thermal changes in the two parts are unconstrained.

The high pressure fluid used to hydrostatically load the radial bearings (see above, Bearing Analysis) is transported between the bearing housing and stator by a tube located on the periphery of the stator. The tube runs circumferentially for approximately 120° before terminating in radial sections that are cemented to the stator and housing. This arrangement for the high pressure supply tube will permit unhindered movement of the stator relative to the housing. A radial passage through the stator transports the high pressure fluid to the loading pocket located on the bore of the stator opposite the load supporting arc of the bearing.

f. Pressure Containment

The pressure containment cylindrical housing will be fabricated from 7075-T6 aluminum alloy. The housing will be thermally insulated on the outside so that the housing metal temperature will be approximately 250°F. The temperature at the sub-base attachment flange is expected to stabilize at 300°F. The thermal strain induced by the rigid attachment of the housing to the sub-base will produce a hoop stress in the shell of about 25,000 psi. This stress is well below the yield strength of the material; including the 50% reduction in yield strength that results from a 1000-hour exposure to 300°F. (Ref. 17). At 290°F, the 1000 hour degradation is only 80%, so that the pressure containment stress of about 35,000 psi will not present any difficulty. The end closure will be machined from 7075-T6 plate. All penetrations through the end closure are reinforced, so that stress levels throughout the end closure are maintained at moderate levels.

In order to restrict the heat flow from the sub-base into the cylindrical housing at the attachment flange, the sub-base contacting surface will be given a relatively thick coating (.06 inch) of the ZrO₂ thermal coating. The contacting surface of the aluminum housing will be hard anodized. In addition, the flange of the housing will be relieved outboard of the metallic

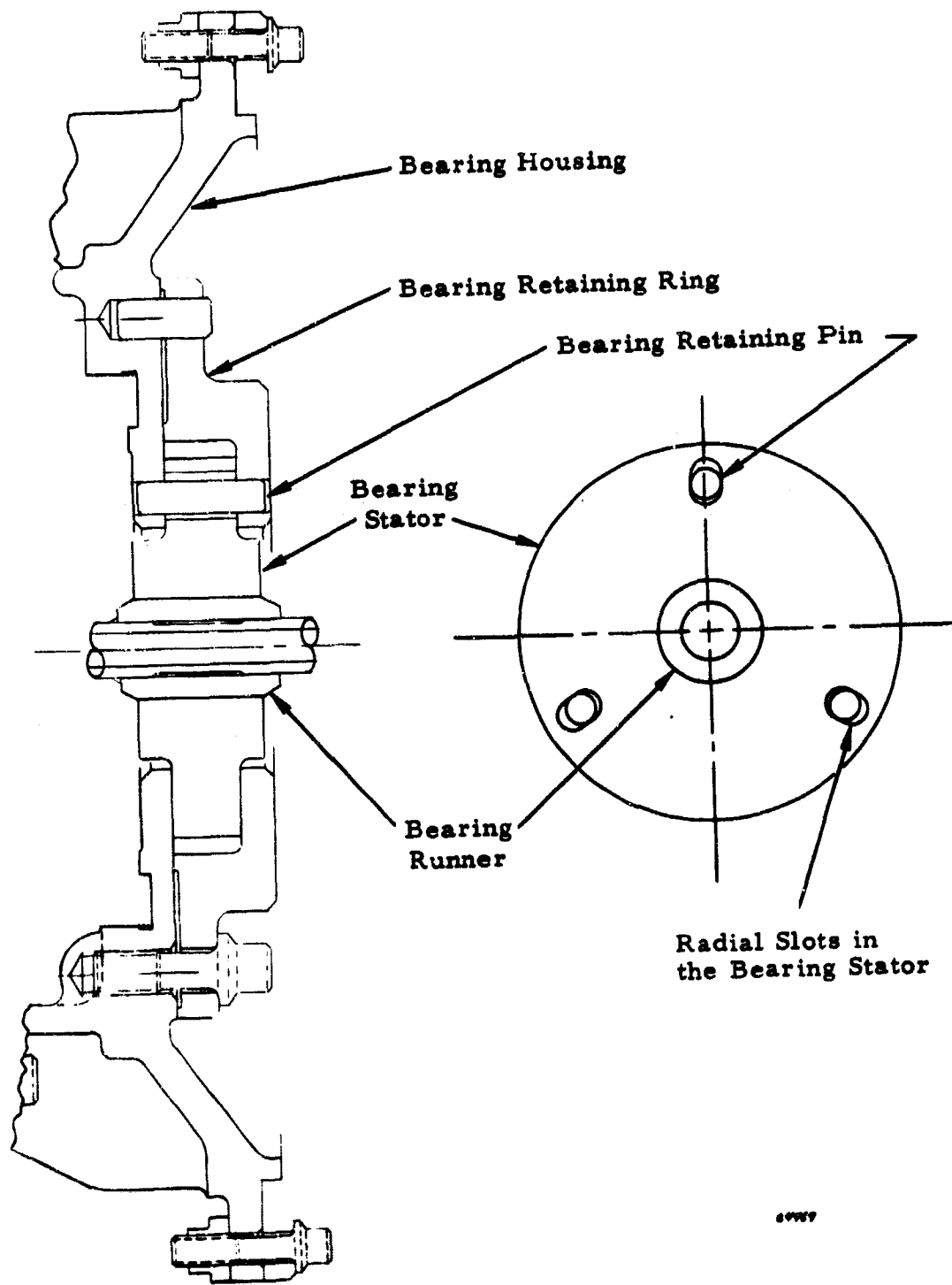


Figure 43. Bearing Attachment

"O" ring seal so that the actual contact area between the two parts will be minimized. Should it be found that these precautions are inadequate to restrict the heat flow to an acceptable level, there would be no difficulty in using multiple layers of ceramic thermal insulators between the clamped surfaces.

The ambient fluid surrounding the CRU will be continually circulated (introduced through the end closure and discharged through the sub-base) to maintain design point pressure and temperature.

9. TURBINE FABRICATION

Since the salient purpose of the 10 kW Feher cycle CRU test program is to demonstrate predicted turbomachinery performance, the fabrication quality of these components, and particularly the turbine, is of utmost importance.

The opinion that was available prior to the investigation concerning the producibility of the small, dimensionally exacting, turbine blades required for the Feher cycle 10 kW turbine was rather negative. However, it became apparent that this judgment was based on superficial considerations and very little actual experimentation with different manufacturing approaches. In order to obtain a high degree of certainty that the turbine quality necessary to demonstrate the predicted efficiency could indeed be produced in a reasonable time and at an acceptable cost, the drawing of a representative turbine shown in Figures 44 through 46, was prepared. The drawing reflects a quality somewhat better than that which would be considered as the minimum acceptable level with respect to blade contour control, surface roughness, fillet radii, and positioning allowances. The drawing describes a welded construction using individually produced blades inserted into gear teeth slots on the hub periphery to form the bladed assembly. However, all the vendors that were contacted were encouraged to consider and propose integral fabrications (blades and hub produced from a one-piece blank) as well as alternative welded or brazed construction.

In all, the drawing was reviewed by 20 vendors as well as Douglas manufacturing specialists. Of these, six contacts including five vendors, will be reported on in some detail since these responses have been responsible for the high degree of confidence that exists on the feasibility of producing the required turbine.

Specific permission to release quotation data from each of the five vendors has not been obtained. Therefore, all five vendors will be referred to by pseudonym in the description of their quotations. The vendors involved are as follows, but not in the order of the following descriptions:

Mechanical Specialties, Inc.
Los Angeles, California

Furno Company
Pomona, California

TEXT NOT REPRODUCIBLE

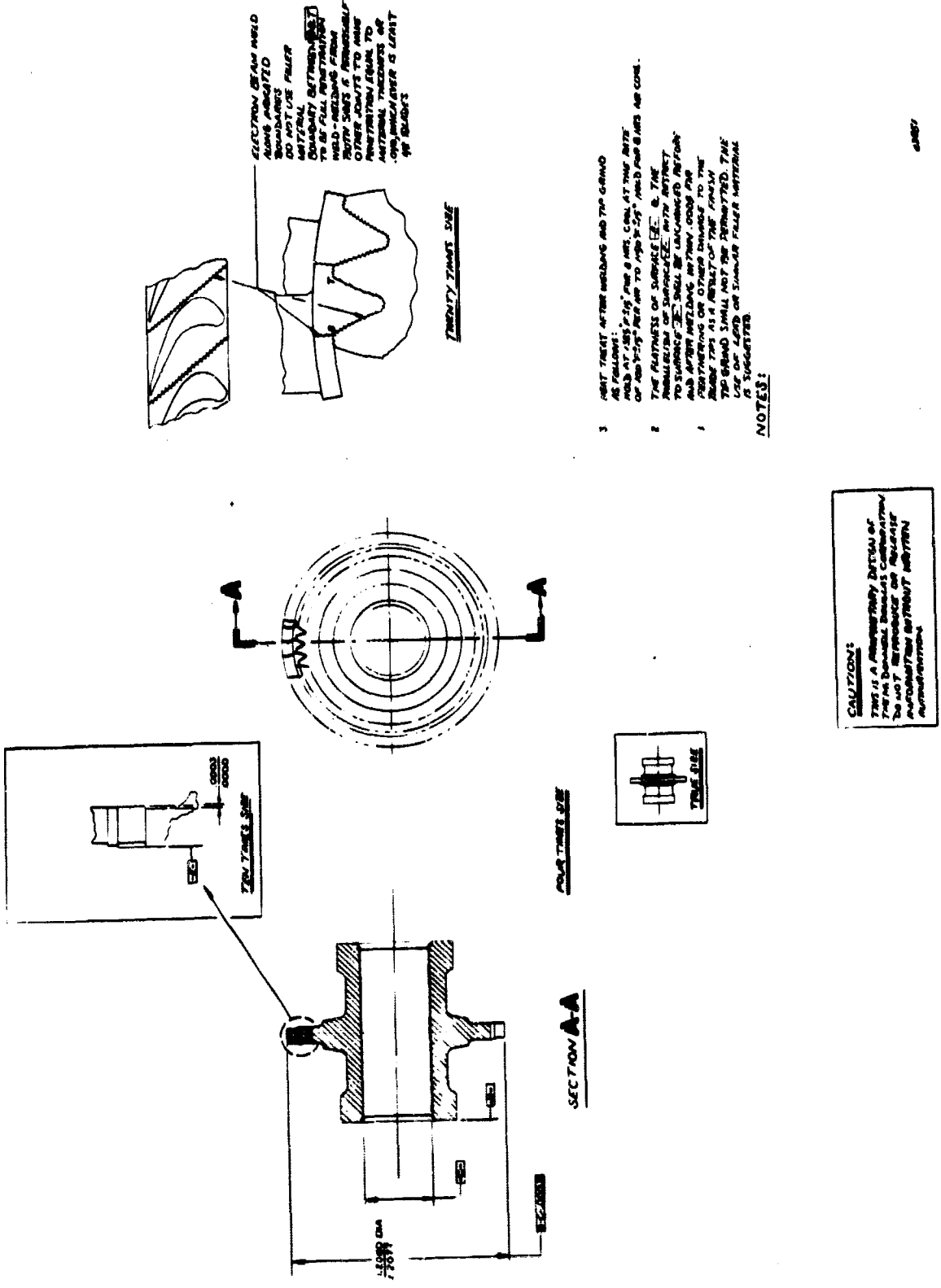


Figure 44. Turbine Assembly 10 kW Feher Engine

Genie Enterprises
Van Nuys, California

Jet Gamma Research and Manufacturing Company
Gardena, California

Metem Corporation
Parsippany, New Jersey

a. Douglas Company Welding Facility
Santa Monica, California

The electron beam welding process for attaching individual blades to the rotor hub was reviewed by Douglas welding experts. Douglas operates a modern Sciaky unit at Santa Monica for both manufacturing research and limited production. For the most part, electron beam welding technique has advanced to the present SOA through the efforts of the few large aircraft manufacturers who have perfected the process for their requirements. In reviewing the CRU turbine, the Douglas welding specialists recommended several minor revisions to the drawing and on this basis, submitted the following ROM estimates:

One turbine assembly	\$1000
Five turbine assemblies	1200

There is a high confidence that the electron beam welding operation will be successful although some risk exists on the ability to satisfactorily fixture all the blades. This uncertainty stems primarily from the fact that locating the blades accurately to the hub and to each other represents a new problem. However, it does appear that the self-positioning feature of the gear tooth root attachments in conjunction with a circumferential clamping ring will satisfy the blade location requirements.

b. Company A

Company A considered the welded construction too costly to be practical and as a result, their efforts have been directed at producing an integral blade and hub fabrication from a one-piece blank by the electrical discharge machining (EDM) process. Their initial offer was to use conventional EDM technique using a solid electrode that produces the pressure side of one blade and the suction side of the adjacent blade simultaneously. They proposed a best-effort arrangement so that manufacturing quality would not be guaranteed. After reviewing this proposal, it was decided that the chances for obtaining a high quality turbine fabrication by this method was too slight to justify the risk of a best-effort procurement. A suggestion was made to Company A to consider a hollow electrode so that both sides of the blade could be produced simultaneously. The vendor undertook a low budget in-house exploratory effort and developed a broaching technique to produce a hollow brass electrode. This electrode was then used to produce a fairly good facsimile of the required blade contour on a steel hub. With these

encouraging results, Company A has now submitted a quotation for the turbine assembly as follows:

One turbine assembly	\$5300 ea
Two turbine assemblies	4150 ea
Five turbine assemblies	3460 ea

c. Company B

Company B is interested in producing the turbine either as a weldment or as an EDM integral unit. After a detailed review conducted at Astropower with representatives from Company B, it was concluded that their confidence of being successful was higher with the one-piece fabrication, and that the welded design would only be less expensive in an easier machining material.

Their objection to the welded design, although intuitive rather than specific, concerned the fixturing of the blades during the welding process. Since Company B would subcontract the welding, they seem disinclined to become overly involved in an unfamiliar area. Their approach to the EDM technique is to use a hollow graphite electrode machined in two pieces and then pinned together. Company B's confidence in being able to produce the turbine is extremely high. Their firm quotation for the completed turbine assembly is:

One turbine assembly	\$3925 ea
Two turbine assemblies	2860 ea
Five turbine assemblies	2200 ea

d. Company C

Company C is confident of being able to machine the individual blades and hub per drawing but express concern for tool life in machining INCO 718. As a result, their quotation reflects a factor of 2 to cover this uncertainty and their bid is qualified to allow for still more tooling costs. Their quotation is as follows:

One turbine assembly w/o welding	\$2605 ea
Two turbine assemblies w/o welding	2385 ea
Five turbine assemblies w/o welding	2355 ea

e. Company D

Company D is highly specialized in pantograph milling of miniaturized precision components. They expressed a high confidence in being able to produce individual blades to print. Their quotation is as follows:

One turbine assembly w/o welding	\$2045 ea
Two turbine assemblies w/o welding	1222 ea
Three turbine assemblies w/o welding	912 ea

f. **Company E**

Company E has been highly successful in producing a variety of complex, intricate components for the aerospace and turbomachinery industries. Due to a lack of familiarity with INCO 718, the following quotation was submitted based on a 321 or 316 type material:

One turbine assembly w/o welding	\$1228 ea
Two turbine assemblies w/o welding	833 ea
Five turbine assemblies w/o welding	578 ea

As a result of the turbine producibility survey, the following conclusions have been reached:

1. The best EDM technique is to machine the blades integral with the hub from a one-piece blank using a hollow electrode. Cost for two turbine assemblies would be \$2960 each;
2. The approximate cost for two welded assemblies in INCO 718 would be \$1875 each, and approximately \$1200 each in a 321 or 316 type material;
3. The confidence of being able to produce a satisfactory turbine assembly in either manner is very good. The integral design warrants a higher confidence rating in view of the potential blade fixturing problem in the welded construction.

Therefore, a cost-effective course of action would be to:

1. Initiate the procurement of five welded turbine assemblies fabricated from 321. These turbines would be used for air turbine tests and initial CRU operation at reduced turbine inlet temperatures; as well as limited time at full temperature. This would allow for low-cost turbines during the phase of the program when the risk of losing turbines due to mechanical failure is relatively high. Furthermore, if the need for basic design changes becomes evident as a result of the early test work, the lower cost turbines will minimize replacement cost.
2. Procure two EDM turbines when,
 - (a) the turbine design is judged satisfactory and suitable for extended testing, or when

- (b) turbine availability becomes the pacing item for the test program due to fabrication problems with the welded construction; whichever occurs first.

10. INSTRUMENTATION

a. Purpose of Instrumentation

The CRU instrumentation is shown in Figure 47. The purpose of this instrumentation can be divided into four major categories as follows:

1. to generate sufficient data for the evaluation of turbo-component performance, and to enable the cause of any discrepancies between observed and expected performance to be determined,
2. to generate sufficient data from which overall CRU system performance can be calculated, and to allow for a detailed accounting of all fluid and energy flows within the CRU,
3. to provide data from which the thermal profile of the structural members of the CRU can be studied, and
4. to give warning of potentially dangerous conditions that could cause damage to the CRU.

b. Measurements Required and Methods

For evaluating turbine performance, the measurements required will be inlet and outlet temperatures and inlet and outlet pressures. Similar measurements will be required on the pump to allow evaluation of pump performance. Because the differences between inlet and discharge temperatures will be small, especially at the pump, direct measurement of these temperatures will require a very high degree of accuracy to obtain high quality performance data. After consulting with instrumentation specialists, it has been determined that each of these measurements can be obtained with acceptable accuracy by the use of a differential thermocouple circuit, together with a high accuracy deviation amplifier and a potentiometer recorder. By using this technique, the voltage difference between the two junctions can be directly measured. This direct measurement of a relatively small difference voltage will be intrinsically of higher accuracy than the independent measurement of two large absolute voltages and the interpretation of a temperature difference from them. Great care will be required in making each of the thermocouple installations in a differential pair as identical as possible, especially in the case of the turbine. There will be heat flowing from the gas to the thermocouple and out the thermocouple stem to the surrounding ambient. This heat flux will be a result of temperature gradients and will cause a difference between the temperatures of the gas stream and the thermocouple junction. The use of good insulation will help considerably to prevent this heat flux. If the physical thermocouple installation is similar on the turbine inlet and outlet, the error due to thermal gradients is also

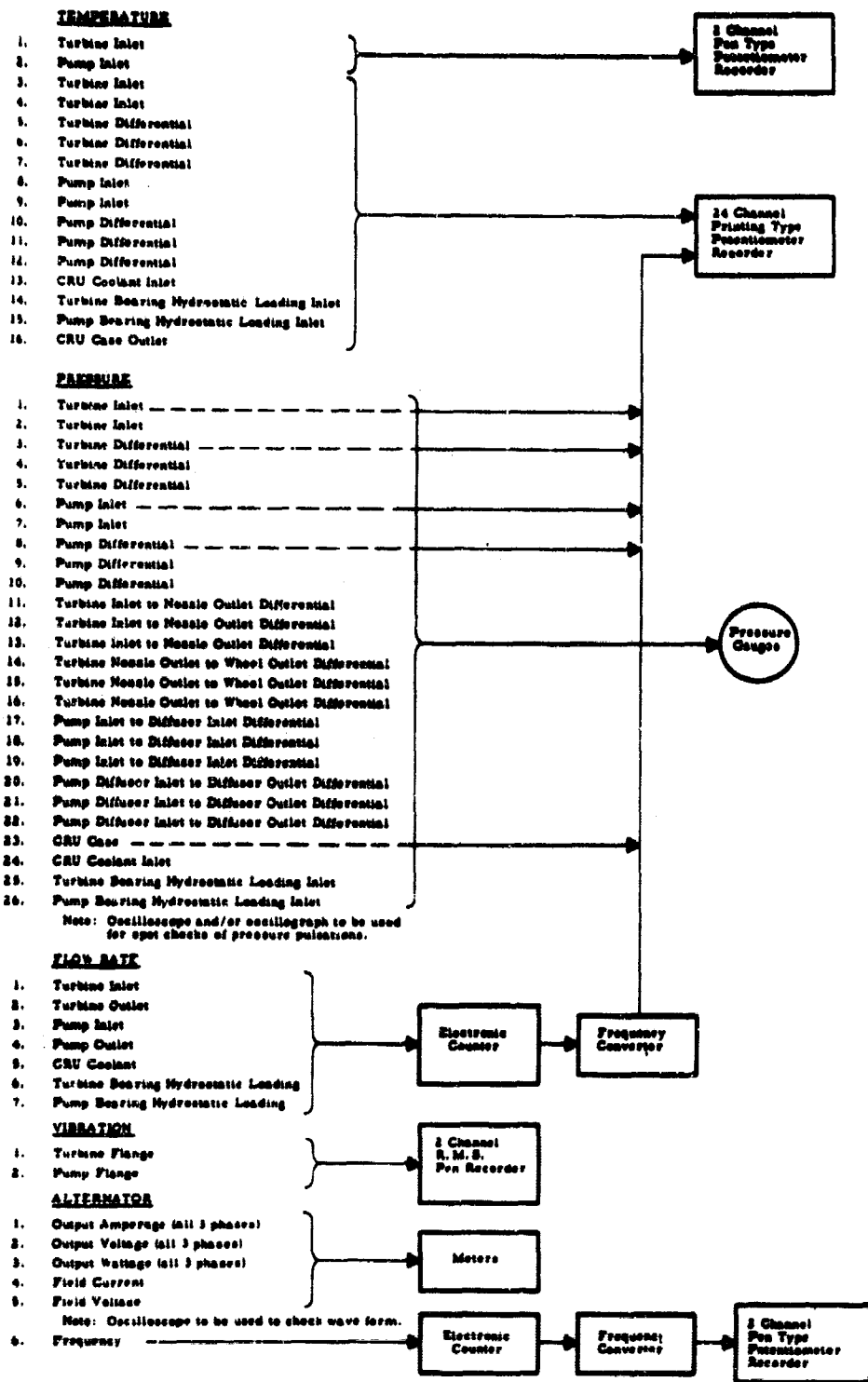


Figure 47. CRU Instrumentation Schematic

similar and the net error in measuring the temperature differential will be small. Using a deviation amplifier, such as the Honeywell Model 80521, the pump and turbine differential temperatures will be recorded with an accuracy of $\pm 2\%$. The absolute temperatures will be sensed with thermocouples and recorded on multipoint potentiometer recorders with an accuracy of $\pm 1\%$.

A similar measurement philosophy will be adopted for the pressure measurements required. One of the end pressures on each turbomachine will be measured directly using a high accuracy, calibrated bourdon-type pressure gage, and the other end pressure will be obtained by measuring the difference between the two end pressures. The absolute and the differential pressures will each be accurate within $\pm 1/2\%$ using this technique.

In addition to determining the overall performance of each of the turbomachines, it is desired that the internal flow conditions be compared and these compared with the design conditions. This will be done by measuring the static pressure profiles along the turbomachine flow paths. To attain the required degree of accuracy, the pressures defining these profiles will be measured with differential pressure gages relative to another pressure within the flow system. The turbine inlet to nozzle outlet and the nozzle outlet to wheel outlet differential pressures will provide data for calculating the degree of turbine reaction. The pump inlet to diffuser inlet and the diffuser inlet to diffuser outlet differential pressures will allow for calculating diffuser pressure recovery. Three measurements will be made at each location to show the circumferential flow distributions and to provide data reliability through redundancy.

To provide a permanent record, certain pressure measurements that completely define the operating status of the test assembly will be sensed by pressure transducers and permanently recorded. However, these recordings will not provide the degree of accuracy attainable with the pressure gauges and will therefore not be used for performance criteria.

The alternator electrical power output will be measured with an accuracy of $\pm 1\%$ using a voltmeter, ammeter and wattmeter on each of the three phases. Electrical output frequency will be determined with an accuracy of ± 1 Hz on an electronic counter. This measurement will also determine the rotor rotational speed, since the alternator is synchronous. Approximately six thermocouples will be located in the alternator assembly to measure the temperature at various points within the stator and the field windings. These measurements will be necessary for computing the alternator I^2R losses. A hermetically sealed thermocouple wire bulkhead connector will pass the thermocouple wires through the pressure enclosure as shown in Figure 40.

The turbine, pump and alternator instrumentation as described will permit evaluating the performance of these components separately. To establish a more complete understanding of the relationships between these components, and to determine the magnitude and source of leakages of fluid, thermal energy or both, within the CRU as a whole, it will be necessary to add other instrumentation. Each journal bearing will be supplied with a

stream of pressurized working fluid that will provide a stabilizing force upon the journal and will also supply fresh cool fluid to the bearing film. An additional flow of pressurized working fluid will flow over the alternator and turbine bearing support structure. This flow will collect the thermal loads resulting from the alternator electrical and windage losses and will also cool the turbine casing and help to establish the desired temperature distribution in the structure connecting the turbine to the alternator. The cooling flow and the two bearing flows will be mingled within the CRU outer case and then extracted through a single port. The temperature pressure and flow rate of each of the three injected streams and of the co-mingled exit stream will be measured. These measurements, together with the turbine, pump and alternator measurements already described, and additional measurements of the turbomachine flow rates will enable an overall energy balance to be made for the entire CRU. This will then permit estimates to be made of the internal leakage flows that are not directly measured and of the windage losses attributable to the rotor and bearings. Flow rates will be sensed with turbine type flow meters and read on electronic counters with an accuracy of 1%. The a. c. output signal of the flow meters will also be converted to a proportional d. c. signal and be recorded with an accuracy of $\pm 2\%$. The bearing hydrostatic loading flow rates will be measured with a laminar flow meter of the type manufactured by National Instrument Laboratories, Inc. These flow meters have the capability of measuring liquid flow rates in the order of 0.05 gallons per minute with an accuracy of $\pm 1\%$.

In addition to the primary performance temperature measurements shown in Figure 47, approximately 20 additional secondary temperature measurements will be recorded throughout the CRU structure from which the thermal profile and internal heat flows of the CRU can be studied. The main purpose of these measurements will be to determine the degree of symmetry of these heat flows and to monitor radial and thrust bearing temperatures. Some of these measurements will also assist in accounting heat energy flows within the CRU. Others will serve to indicate excessively asymmetrical temperature distributions or excessive temperature levels that could result in damage to the CRU if allowed to continue or worsen.

Two other additional measurements will be taken that will monitor the operation of the bearings and of the rotating assembly in general. Pump and turbine bearing vibration will be sensed by mounting accelerometers externally on the CRU outer case flanges. After consulting with vibration specialists, it was determined that an accelerometer mounted externally on the outer case turbine end flange would also be able to detect a hit of the turbine blades against a small pin located in the turbine wheel shroud. Approximately eight small diameter pins constructed from a soft metallic material will be positioned around the circumference of the turbine wheel shroud. Using a shroud so equipped, that will also be dimensioned to give a relatively large turbine blade tip clearance, initial testing will be carried out that will determine the amount of any thermal distortion occurring in the turbine shroud and its support structure without risking severe damage to the turbine wheel. After running such tests and solving any thermal distortion problems that may arise, it will be possible to reduce the operating turbine blade tip clearance to the design value of .001 inch and proceed with the

performance testing program. Accelerometers and charge amplifiers such as the Endevco Models 2271A and 2713B will be used. With the expected low level of background noise, this equipment should give a definite indication of metal to metal contact of either the bearings or the turbine blade tips striking the shroud pins.

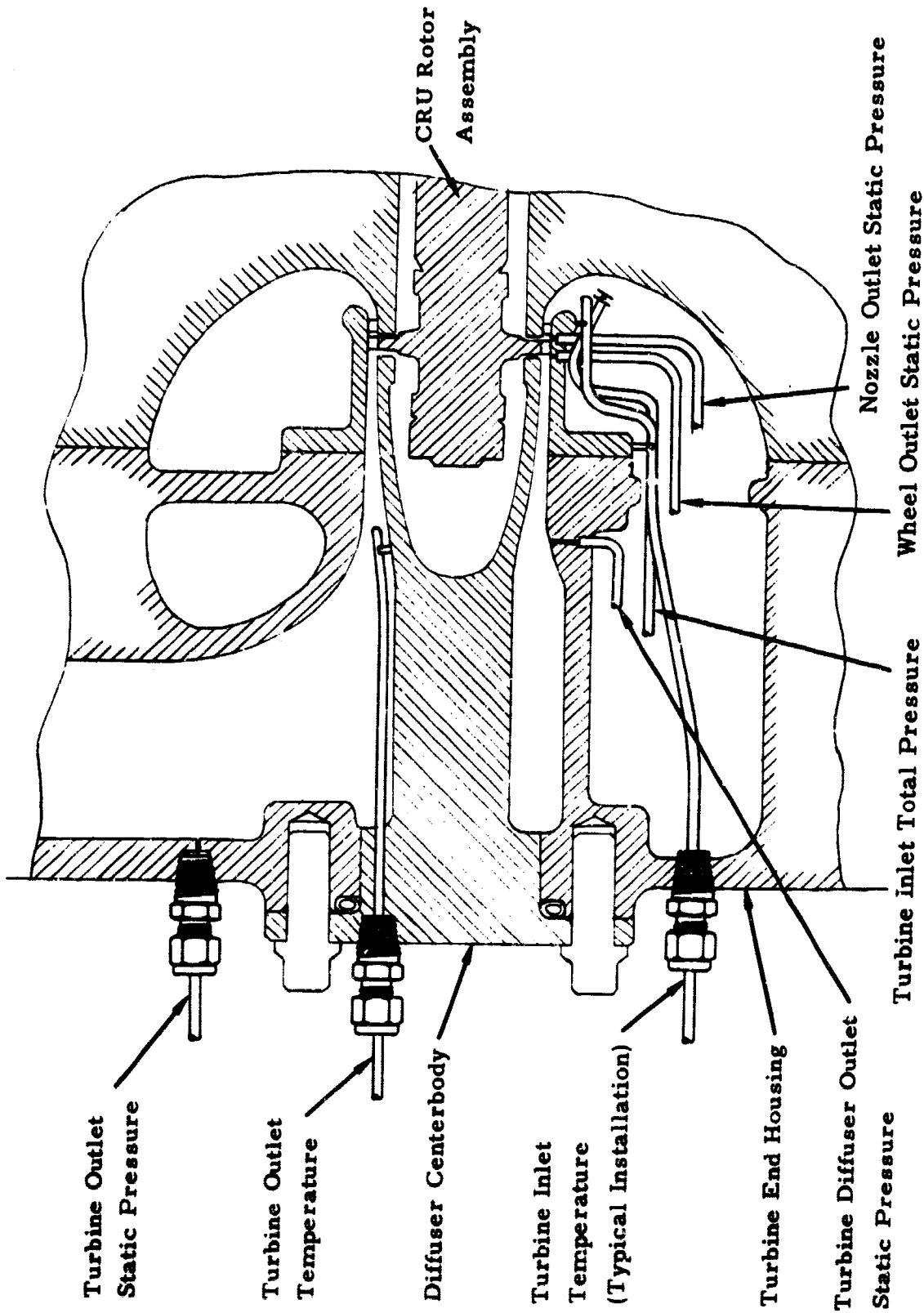
c. Turbine and Pump Instrumentation Assemblies

The majority of the instrumentation to be used is conventional and therefore presents no particular problem to a competent technician. The small dimensions of the pump and turbine assemblies and the large number of measurement taps desired has resulted in considerable study of the problems involved. The following represents the results of this study and defines in specific terms the methods that will be used to construct and install the more difficult of the instrumentation probes required.

Figure 48 is an enlargement of the turbine section of the CRU assembly as shown in Figure 39. All temperature probes and pressure tubes shown for the turbine will be 1/16-inch outside diameter. The turbine outlet temperature probes will be installed on the diffuser centerbody assembly. A typical thermocouple probe will be fully sheathed and sealed into the wall with a Swagelok compression fitting. The thermocouple end will be supported in the turbine exhaust gas stream by a small bracket spot welded to the thermocouple sheath and to the centerbody surface. This will ensure accuracy of position and resistance to vibratory forces. Flow area blockage will be minimal. All of the probes will be mounted on the centerbody and checked prior to the installation of the complete assembly in the turbine end housing.

The turbine outlet static pressure tap holes will be machined through from the turbine inlet plenum. Small tubes welded or nickel brazed to the turbine end housing will connect the pressure tap holes to fittings accessible on the outer wall of the turbine end housing.

The turbine wheel outlet and the nozzle outlet static pressure tap holes will be connected to tubes nickel brazed into countersunk recesses in the outside surface of the turbine shroud. This brazing operation will be performed prior to the final machining of the shroud inside surface to ensure dimensional stability and accuracy of the shroud bore. The turbine inlet temperature and total pressure probes will be attached to the outside of the turbine shroud with small brackets resistance welded in place. Upon assembly of the turbomachine, the shroud with its instrumentation will be bolted to the turbine end housing. Each of the tubes and thermocouples attached to the turbine shroud will be sealed through the outer wall of the turbine end housing by a Swagelok compression fitting. These leads will have excess length that will be coiled within the turbine inlet plenum. The extra length will allow repeated assembly and disassembly of the turbine shroud. Each time it is required to remove the shroud, it will only be necessary to cut off a short length of each of the instrumentation lead including the compression fitting ferrule with which is swaged to the lead. On reassembly, a new ferrule will be installed and each lead will be pulled through a little further than before.



17790

Figure 48. Turbine Instrumentation

Figure 49 is an enlargement of the pump section of the CRU assembly as shown in Figure 39 of the design section of this report. All the temperature probes shown for the pump will be 1/32 inch, outside diameter. The pump outlet temperature probes will be seal bonded through the wall of the pump end bearing support, as shown. The thermocouple ends will be supported by small brackets from the diffuser assembly after the diffuser is attached to the pump end bearing support. The thermocouple wires will pass through the outer case pump end cover by means of a hermetically sealed thermocouple wire bulkhead connector. Excess thermocouple wire is left within the cavity to allow for repeated assembly and removal of the cover.

The pump inlet temperature probes will be seal bonded through the wall of the pump inlet plenum. The thermocouple ends of the probes will be supported by a spider type bracket bonded to the probes. This bracket will be a slip fit in the pump inlet passage. The inlet plenum and the temperature probes can therefore be installed as a unit into the pump inlet duct.

The pump diffuser assembly and pump end bearing support will be ported to sense the pump diffuser inlet and outlet static pressures. For each port, an "O" ring seal is provided at the interface between the diffuser assembly and the pump end bearing support to prevent leakage to or from the pump outlet plenum. A 1/16-inch outside diameter tube is seal bonded into each of the counterbores at the end of the ports in the pump end bearing support. The tubes are then fed through a Swagelok fitting in the outer case pump end cover. Excess length of tubing is left within the end cover cavity to allow for repeated assembly and disassembly of the CRU.

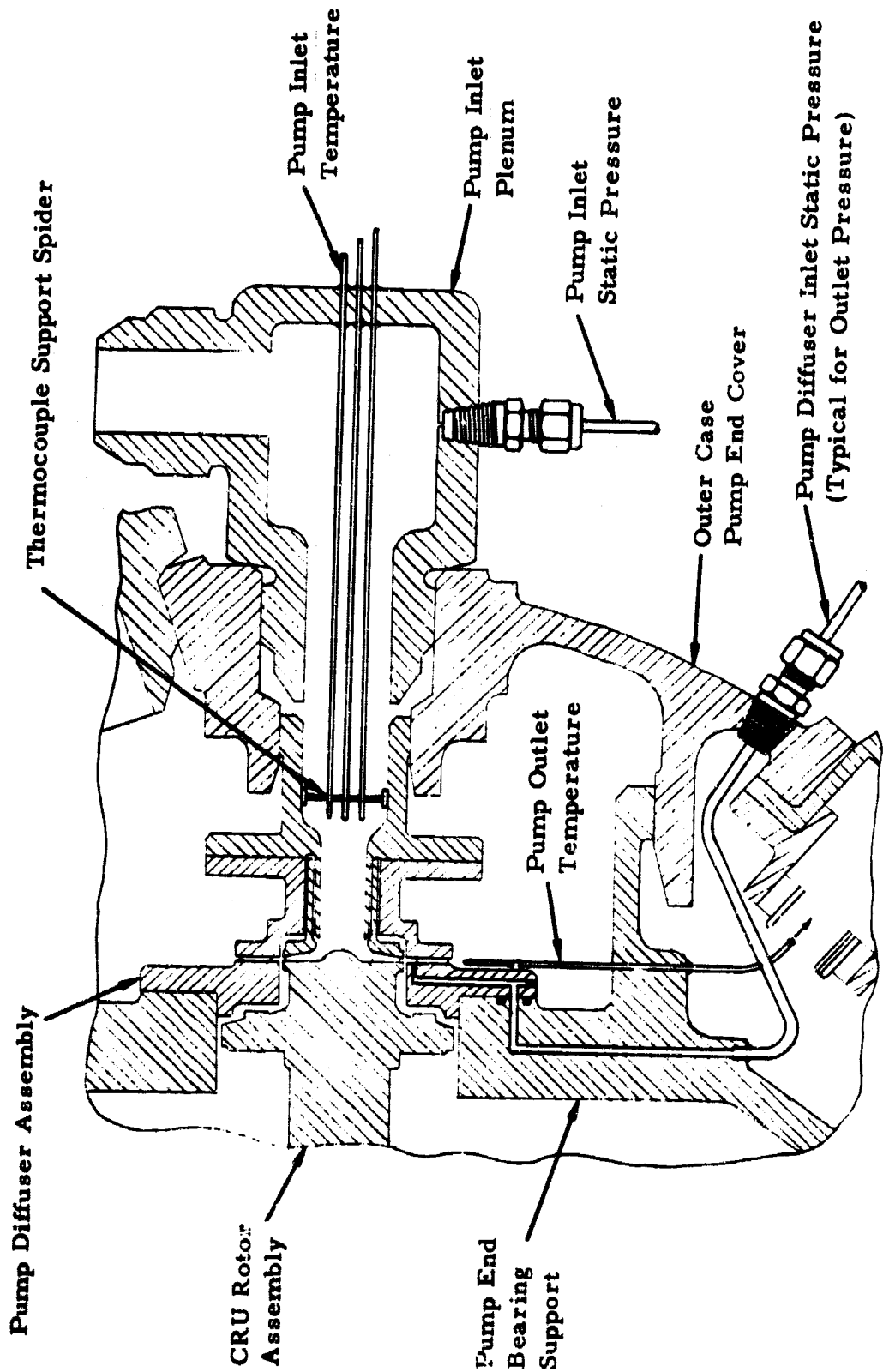
A slight modification of the CRU outer case is contemplated that would lengthen the cylindrical part of the CRU outer case at the pump end by about two inches. This would enable all of the internal instrumentation to be connected through the cylindrical wall of the case instead of through the outer case pump end cover. The result would be a simplification on instrumentation installation because of the increase in accessibility. However, full-strength reinforcement of spherical cut-outs are more readily managed.

d. Data Error Analysis

A preliminary examination has been made of the CRU system and of its subcomponents to determine the effects of measurement inaccuracies upon performance estimation. This is considered essential to the program in order to establish the limits of likely error in the calculated performance figures and to assure the design and procurement of instrumentation that is wholly adequate for the desired purpose.

The following is an example of how the methods of error analysis can be applied to testing for the determination of turbine efficiency by shaft power estimation. It shows the effect that the instrumentation error can have on the accuracy of the desired result.

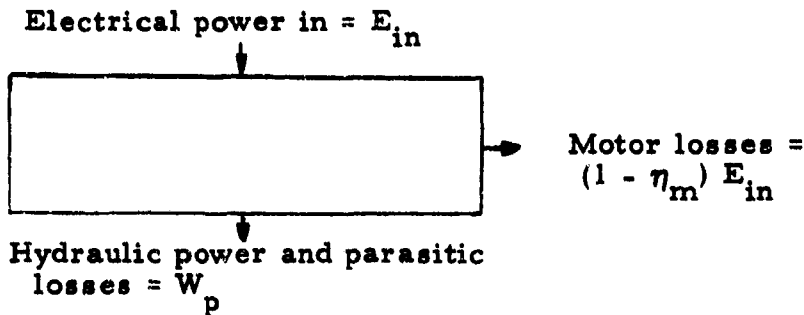
The testing is conducted in two phases. The first test consists of motoring the pump with the alternator in the CRU at the design pressure and



CW7

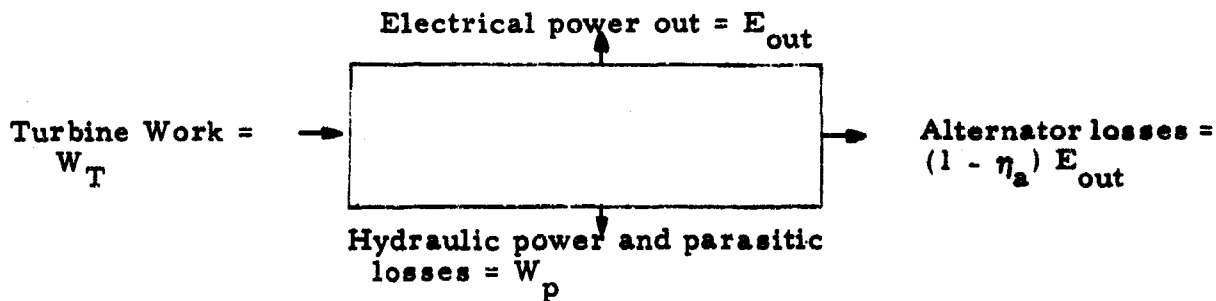
Figure 49. Pump Instrumentation

temperature and flow conditions. The turbine wheel is removed from the rotor. The division of power is as shown below



and $W_p = \eta_m E_{in}$

The second test consists of operating the complete CRU at rated power. The division of power is now as shown.



and $W_T = \frac{E_{out}}{\eta_a} + W_p$

By combining the results of the two tests

$$W_T = \frac{E_{out}}{\eta_a} + \eta_m E_{in}$$

The turbine isentropic differential enthalpy can be shown to be approximated by:

$$\Delta H_{(is)} = C_p \chi T_{in} \text{ (BTU/lb)}$$

where

$$\chi = \left[1 - \left(\frac{P_{out}}{P_{in}} \right)^{\frac{\gamma - 1}{\gamma}} \right]$$

- and C_p = Mean specific heat at constant pressure of the working fluid during the expansion process. (BTU/lb °F)
- P_{out} = Turbine outlet pressure (psia)
- P_{in} = Turbine inlet pressure (psia)
- γ = Effective ratio of specific heats = $\frac{C_p}{C_v}$
- C_v = Specific heat at constant volume
- T_{in} = Turbine inlet temperature (°R)

Recognizing that C_p is a function of temperature only at the turbine operating temperatures and can be handled as a constant, the turbine ideal work,

$W_{T(is)}$, is

$$W_{T(is)} = K F T_{in}$$

where F = Working fluid flow rate (lb/sec)

and $K = (1.055) C_p \chi$

and 1.055 is constant of conversion from BTU/sec to kW

and, Turbine efficiency = $\eta_t = \frac{W_T}{W_{T(is)}}$

or
$$\eta_t = \frac{\frac{E_{out}}{\eta_a} + \eta_m E_{in}}{K F T_{in}}$$

For the cycle pressure ratio and turbine operating temperature shown in Turbo-component Analysis section of this report, the following table lists typical values for the variables and their respective variations.

	<u>Value</u>	<u>Variation</u>	<u>% Variation</u>
E_{out}	10 kW	0.10 kW	1.0
E_{in}	5.4 kW	0.05 kW	0.927
η_a	0.9	0.01	1.1
η_m	0.5	0.02	4.0
F	1.06	0.01 lb/sec	0.943

K	0.00955 $\frac{\text{Kw sec}}{\text{lb OF}}$.0002 $\frac{\text{Kw sec}}{\text{lb OF}}$	2.1
T _{in}	1900°R	19°R	1

Each of the factors in the above table have been assigned a percentage variation which are considered to be possible during the actual test circumstance. The amount of the variation has been set so that a 95% certainty (2 σ) exists that the actual value will be within the stated variation.

The possible variations in the resulting component efficiencies will therefore have a 95% certainty that the true component efficiency will indeed be within the indicated range.

Having established a statistical variation in the values for the various quantities used to compute the component efficiency, it remains to determine the variation in the result.

From Schenck (Ref. 18) it is shown that the following relationship exists.

$$\left[\epsilon (R) \right]^2 = \left(\frac{\partial R}{\partial X_c} \right)^2 \left[\epsilon (X) \right]^2 + \left(\frac{\partial R}{\partial Y_c} \right)^2 \left[\epsilon (Y) \right]^2 + \dots$$

where R = f (X, Y)
 $\epsilon (R)$ = Variation in R
 $\epsilon (X)$ = Variation in X
 $\epsilon (Y)$ = Variation in Y
 X_c = Correct value of X
 Y_c = Correct value of Y

Using this relationship and the above equation for turbine efficiency,

$$\left[\epsilon (\eta_t) \right]^2 = \left(\frac{1}{\eta_a K F T_{in}} \right)^2 \left[\epsilon (E_{out}) \right]^2 + \left(\frac{E_{out}}{\eta_a^2 K F T_{in}} \right)^2 \left[\epsilon (\eta_a) \right]^2 +$$

$$\left(\frac{E_{in}}{K F T_{in}} \right)^2 \left[\epsilon (\eta_m) \right]^2 + \left(\frac{\eta_m}{K F T_{in}} \right)^2 \left[\epsilon (E_{in}) \right]^2 + \left(\frac{E_{out} \eta_m E_{in}}{K^2 F T_{in}} \right)^2$$

$$\left[\epsilon (K) \right]^2 + \left(\frac{E_{out} \eta_m E_{in}}{K F^2 T_{in}} \right)^2 \left[\epsilon (F) \right]^2 + \left(\frac{E_{out} \eta_m E_{in}}{K F T_{in}^2} \right)^2 \left[\epsilon (T_{in}) \right]^2$$

Substituting in the variables and variations from the above table gives,

$$\text{Variation in } \eta_t = \epsilon(\eta_t) = .0367$$

and substituting the variables in,

$$\eta_t = \frac{\frac{E_{\text{out}}}{\eta_a} + \eta_m E_{\text{in}}}{K F T_{\text{in}}} = \frac{\frac{10}{.9} + (.5)(5.4)}{(0.00955)(1.06)(1900)} = .712$$

$$\text{and percentage variation} = \frac{[\epsilon(\eta_t)]}{\eta_t} = \frac{.0367}{.712} = 5.16\%$$

This resulting accuracy in the determination of turbine efficiency could be improved somewhat as some of the variations listed in the table are on the conservative side.

Section IV

AIR TURBINE PRELIMINARY DESIGN

1. DEFINITION OF AIR TEST CONDITIONS

Dimensional analysis applied to turbomachines shows for kinematic similarity any selected fluid velocity vector, V , must remain in the same proportion to a corresponding machine velocity vector at all geometrically similar points within the flow system. Relating all fluid velocities to the turbomachine tip velocity U , this requirement may then be expressed by $V/U = \text{constant}$. Relating these velocities to the flow capacity Q and diameter D of the turbomachine, the expression becomes

$$\frac{Q/D^2}{N D} = \text{constant} \quad \text{or}$$

$$\frac{Q}{N D^3} = \text{constant.}$$

If the assumption is made that the only forces acting on the fluid are inertial forces, the relation between these forces and the fluid velocities under similar flow conditions is

$$\frac{F}{a} = P = \text{const } \rho V^2$$

Now, $\frac{P}{\gamma} = H = \text{const } \frac{V^2}{g}$ and since $\frac{V}{U} = \text{constant}$,

then $\frac{2gH}{U^2} = \text{const.}$

Again relating the velocity to the diameter of the turbomachine, the expression becomes

$$\frac{2gH}{N^2 D^2} = \text{constant} \quad \text{or}$$

$$\frac{H}{N^2 D^2} = \text{constant.}$$

These two basic relationships completely define similarity for turbomachines operating with a perfect, inviscid, incompressible fluid.

For a real compressible fluid, consideration must also be taken of viscous and elastic forces existing within the fluid. The viscous forces can be correlated by considering a turbomachine Reynolds Number which can be expressed as

$$R_e^* = \frac{U D \rho}{\mu}$$

This Reynolds Number allows a direct comparison between geometrically similar machines, but the quantities used in its derivation do not express, except in the broadest terms, the nature of the flow within the turbomachine passages. In order to better define this flow, it is more accurate to consider the Reynolds Numbers of the stator and of the rotor separately. The rotor Reynolds Number R_{e_r} is expressed as

$$R_{e_r} = \frac{w_{2rel} \cdot C \cdot \rho_2}{\mu_2}$$

where w_{2rel} = gas inlet velocity vector relative to rotor

C = rotor blade chord

ρ_2 = rotor inlet density

μ_2 = rotor inlet viscosity

Test data shows that a decrease of rotor Reynolds Number below 3×10^5 can be correlated with an increase in various turbomachine loss coefficients. In order to assure that such viscous effects are held to small proportions, it is recommended that the rotor Reynolds Number be 3.5×10^5 or greater.

Working fluid compressibility effects can be correlated by considering the turbomachine Mach Number

$$M^* = \frac{U}{C_s}$$

This Mach Number expression allows a comparison between geometrically similar turbomachines, but does not represent the true flow Mach Numbers existing within the turbomachine passages. These are better expressed by the nozzle exit Mach Number.

$$M_1 = \frac{V_1}{C_{s_1}}$$

where V_1 = nozzle exit velocity

C_{s1} = acoustic velocity in the nozzle exhaust flow.

or the rotor exit Mach Number

$$M_3 = \frac{w_3}{C_{s3}}$$

w_3 = rotor exit velocity relative to rotor

C_{s3} = acoustic velocity in the rotor exhaust flow

The Mach Number also correlates the changes in volumetric flow rate through a turbomachine system for a compressible fluid, and thereby correlates the velocity triangles throughout a turbomachine operating with a compressible fluid. For low Mach Numbers, the changes in volume flow are small, and some variation of turbomachine Mach Number can be tolerated without causing excessive distortion of the velocity triangles.

Summarizing the foregoing discussion for the case in which a turbine of given design and dimension is to be tested using a different compressible fluid from that for which it was designed, the required similarity criteria reduce to

$$\frac{Q}{ND} = \text{constant}$$

$$\frac{H}{N^2 D^2} = \text{constant}$$

$$\frac{Np}{\mu} = \text{constant}$$

$$\frac{N}{C_s} = \text{constant}$$

The third and fourth expressions can be used to define the temperature and pressure conditions under which the test fluid flow is identical with the design point fluid flow, and also the rotational speed at which the turbomachine should be operated. From the definition of speed, the volume flow and head conditions to be applied are determined from the first and second expressions.

a. Establishment of the Air Test Conditions Equivalent to the Turbine Design Point

The following parameters can be extracted from the turbine design and design point flow conditions.

$$\begin{aligned} N &= 80,000 \text{ RPM} \\ C &= .106 \text{ inch} \\ D &= 1.20 \text{ inch} \\ H_{ad} &= 17.126 \text{ Btu/lb} \\ T_{out} &= 1399.44^\circ\text{F} \\ P_{out} &= 1850 \text{ psia} \\ w &= 1.064 \text{ lb/sec} \end{aligned}$$

The following outlet fluid properties can be derived

$$\begin{aligned} \mu_{out} &= .0988 \text{ lb/hr ft.} \\ \rho_{out} &= 3.85 \text{ lb/ft}^3 \\ C_{s out} &= 1686 \text{ ft/sec} \\ Q &= .2765 \text{ ft}^3/\text{sec} \end{aligned}$$

Assuming that the test turbine is to be operated with dry air and that the turbine exhaust static temperature is 75°F , the relevant properties of the air are

$$\begin{aligned} \mu_{air} &= .045 \text{ lb/hr ft} \\ C_{s air} &= 1134 \text{ ft/sec} \end{aligned}$$

Using the relationships previously defined

$$\frac{N_{air}}{N_{CO_2}} = \frac{C_{s air}}{C_{s CO_2}} = \frac{1134}{1686} = .6726$$

$$N_{air} = 80,000 \times \frac{1134}{1686} = 53807 \text{ RPM}$$

$$\begin{aligned} \rho_{\text{air}} &= \rho_{\text{CO}_2} \times \frac{N_{\text{CO}_2}}{N_{\text{air}}} \times \frac{\mu_{\text{air}}}{\mu_{\text{CO}_2}} \\ &= 3.85 \times \frac{1}{.6726} \times \frac{.045}{.0988} = 2.605 \text{ lb/ft}^2 \end{aligned}$$

$$\begin{aligned} Q_{\text{air}} &= Q_{\text{CO}_2} \times \frac{N_{\text{air}}}{N_{\text{CO}_2}} \\ &= .2765 \times .6726 = .1860 \text{ ft}^3/\text{sec} \end{aligned}$$

$$\begin{aligned} H_{\text{ad air}} &= 17.126 \times \frac{N_{\text{air}}}{N_{\text{CO}_2}} \\ &= 7.75 \text{ Btu/lb} \end{aligned}$$

Reducing these density and isentropic head requirements to pressure and temperature values, the cold air test conditions which will exactly simulate the hot CO₂ turbine performance will be

$$\begin{aligned} P_{\text{in}} &= 634.3 \text{ psia} \\ T_{\text{in}} &= 99^\circ\text{F} \\ P_{\text{out}} &= 515 \text{ psia} \\ N &= 53,800 \text{ RPM} \end{aligned}$$

Under these conditions the turbine should flow .485 lb/sec of air. Assuming an adiabatic efficiency of .75, it should develop 3.99 HP, equivalent to a measured torque of 4.67 lb-inch.

b. Review of the Equivalent Air Test Conditions

Although the air test conditions established will accurately simulate the design point flow and performance conditions, it is apparent that they still involve elevated pressures and in particular require an air supply of considerable magnitude. This is a common characteristic of such testing, and an economic accommodation is usually reached by testing at low pressure, provided that the simulation of flow conditions is not seriously in doubt. In most turbomachinery cases, the design point Reynolds Numbers are extremely large, and legitimate testing can be done at much smaller Reynolds Numbers without serious discrepancy. The case under examination is no exception, but a check of the turbomachine design point Reynolds Number (R_e^*) shows

that this is 6.4×10^6 . This is very low relative to turbomachines in general, and indicates that the rotor Reynolds Number (which is usually an order of magnitude lower than the turbomachine Reynolds Number for this class of machine) is not far above the critical value below which the viscous fluid forces can be expected to seriously affect the turbomachine flow characteristics. A more detailed examination confirms that the design point Rotor Reynolds Number is 4.68×10^5 . Although this is good from the standpoint of predicting the flow within and the performance of the turbine at its design point, it severely limits the reduction in air test pressure level which can be made without impairing the evaluation of the turbomachine's performance. To hold the Rotor Reynolds Number to the desired minimum of 3.5×10^5 would permit a reduction of the air test condition pressure levels to minimums of 475 psia inlet and 385 psia outlet.

One possible way of reducing these pressure levels would be to test at an increased turbomachine Mach Number. For instance, doubling the head and increasing the turbomachine speed 41.4% would result in very similar dynamic and kinematic conditions, but would increase the Rotor Reynolds Number by about 45%. This would permit a decrease of the air outlet pressure to about 265 psia but still require a 400 psia inlet pressure. It is apparent that the decrease in pressure level is not of significant proportion as far as the provision of an air supply is concerned. Also, the required air test turbine speed has risen to 76,100 RPM, and the pressure differential across the turbomachine has increased, thereby further aggravating an already difficult axial thrust load situation.

Accordingly, it has been decided to test the turbine using cold air at the correct Mach Number and velocity ratio conditions and at a Reynolds Number condition which will assure validity of the test data. It should be pointed out that the same turbine tested in the CRU would be expected to show a design point performance slightly better than that achieved in these air tests due to the more favorable Reynolds Number conditions.

c. Air Test Conditions.

$$P_{in} = 475 \text{ psia}$$

$$T_{in} = 99^{\circ}\text{F}$$

$$P_{out} = 385 \text{ psia}$$

$$N = 53,800 \text{ RPM}$$

$$W = 0.363 \text{ lb/sec}$$

2. DESIGN INTEGRATION

The air turbine testing will be done with a modified Vortec Model 20.020 dynamometer. Although Vortec has ceased operations, the Clayton Manufacturing Corporation of Los Angeles is expected to continue the Vortec

dynamometer product line. Furthermore, the McDonnell Douglas Corporation (major stockholder of Vortec) has access to a complete set of drawings and numerous components so that a special build of the unit could readily be accomplished, if necessary.

The air turbine test setup is shown in Figures 50 and 51. The air is passed through a straightening section before entering the nozzle. The turbine discharge consists of an axial diffuser, followed by a constant velocity, axial-radial passage into a plenum chamber. The flow from the plenum chamber is controlled by a variable pressure differential regulating valve mounted directly on the main turbine housing.

The air turbine section construction consists of the main turbine housing, an inner turbine housing, and an air seal assembly on the discharge side of the turbine rotor. The dynamometer shaft has been modified to provide sufficient extension so that the multiple labyrinth air seal could be used as well as the actual turbine with its extended hub. An aluminum seal ring is clamped to the inlet side of the turbine rotor to provide a peripheral seal against circulatory flow within the closed cavity from affecting the normal flow into the turbine.

Both the main and inner turbine housings will be machined from aluminum bar stock. The turbine nozzle vanes will be machined integral with the inner shroud from free-machining brass bar stock. The outer shroud will be interference fitted over the nozzle vanes and fixed in place by .018 inch diameter steel pins in radial holes through the shroud into the nozzle vanes. The labyrinth seals are fabricated from leaded phosphor bronze sheet metal strips alternated with copper spacer rings which are fused together to form the seal assembly. The rotor shaft under the labyrinth seals will be electroless nickel plated and polished.

After bolting and dowelling the dynamometer and main turbine housing to the common sub-base, the principal locating diameter in the main turbine housing will be finish ground in assembly to ensure proper concentricity between rotor and housing.

The two questionable features of the air turbine test configuration were:

1. possible rotor dynamic problems, and
2. dynamometer bearing difficulties due to the relatively high thrust load imposed by the pressure differential across the turbine rotor.

a. Rotor Dynamics

A full length model of the rotor is shown in Figure 52 together with a graphical presentation of the EI characteristic over the length of the rotor. The critical speed model shape was assumed to be of the form,

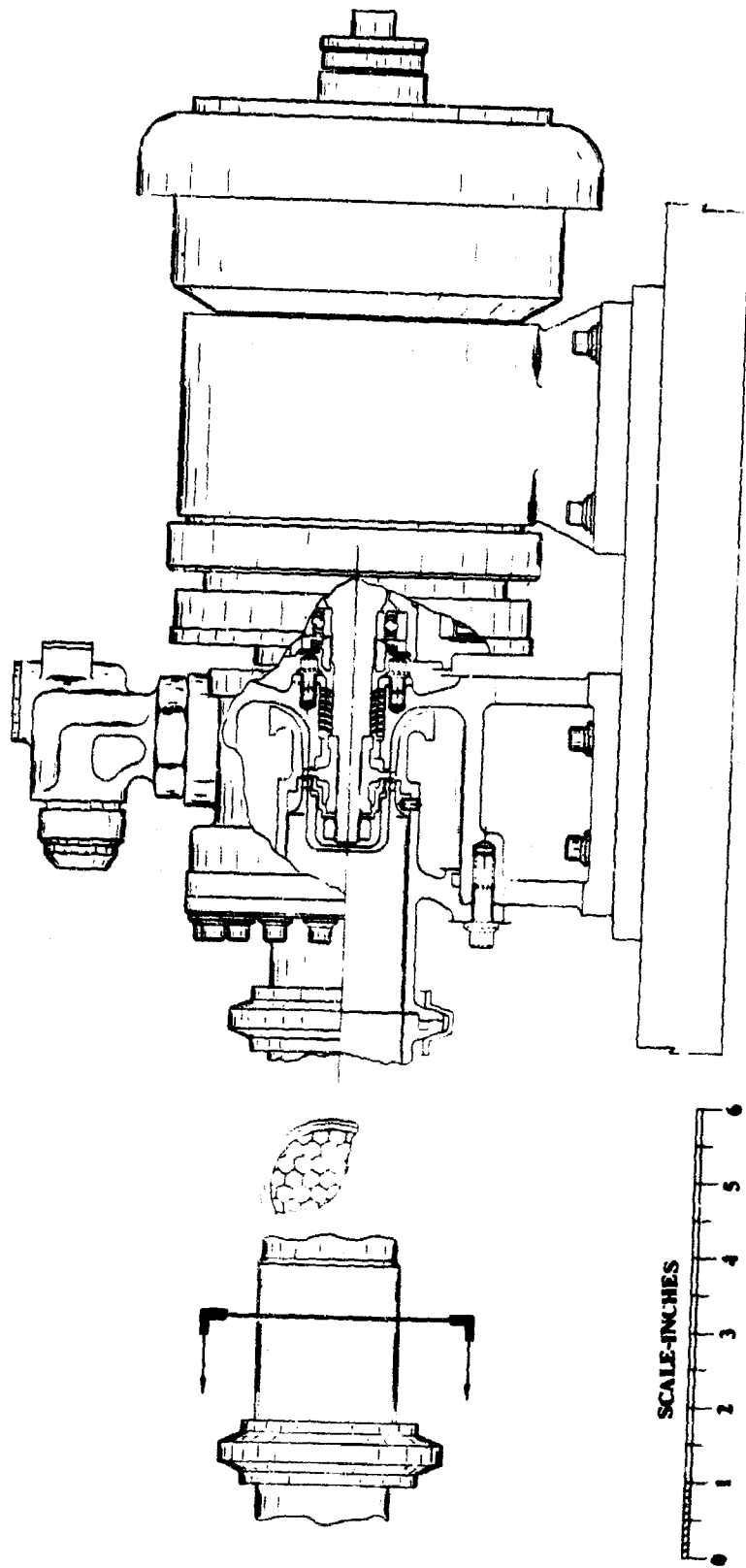
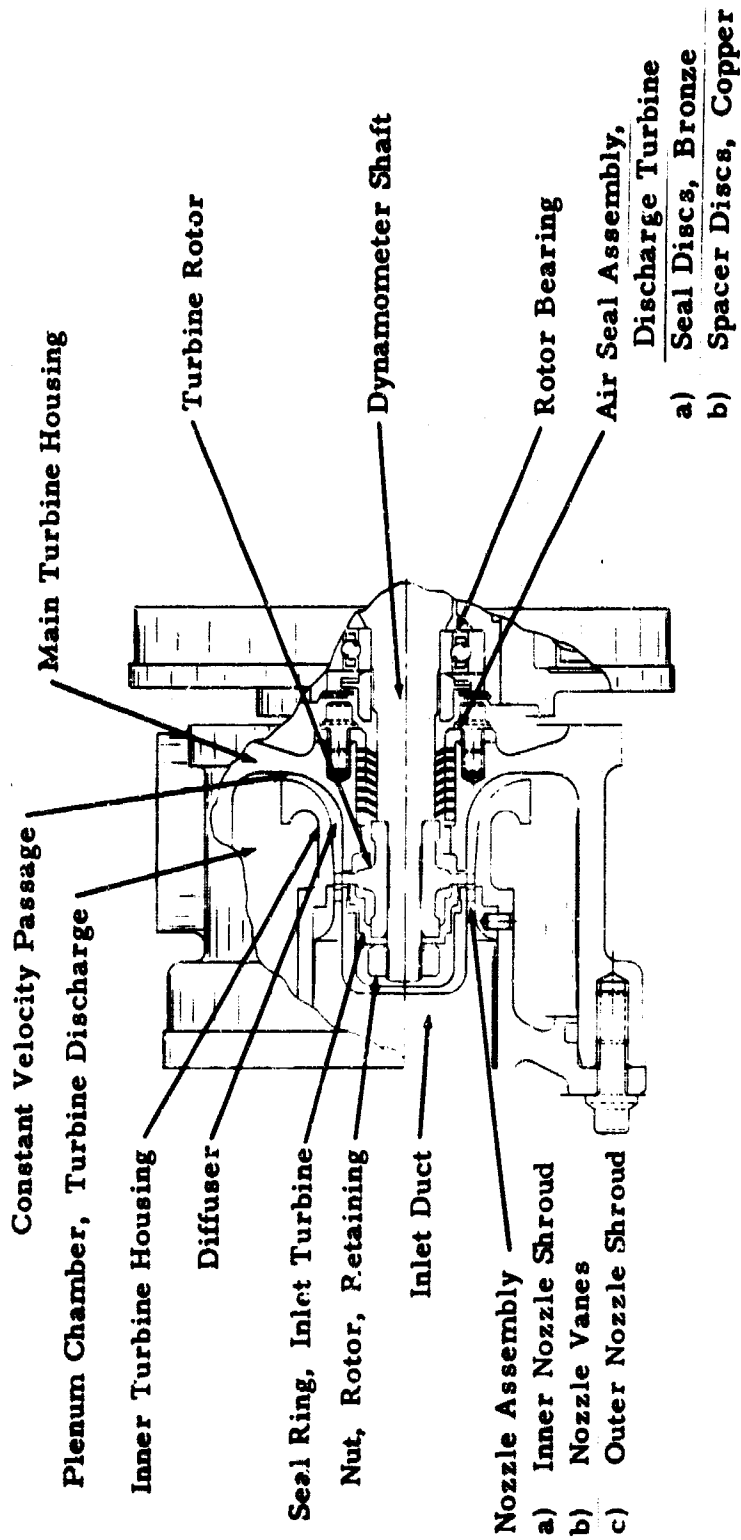
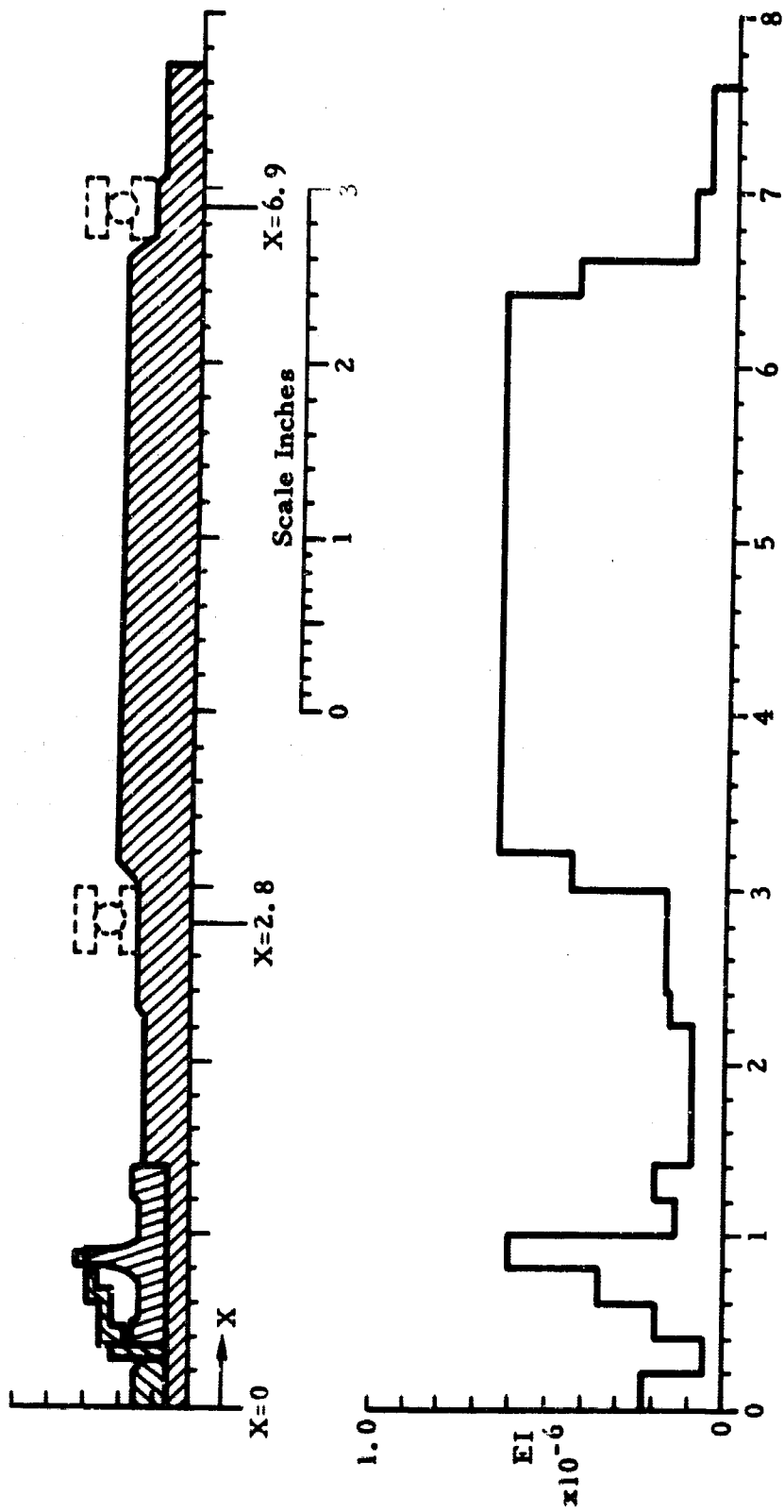


Figure 50. Air Turbine Test Configuration



44773

Figure 51. Air Turbine Assembly



4977

Figure 52. Rotor Proportions

$$y = a + bx + cx^2 + dx^3 + ex^4 + fx^5$$

where the coefficients are determined by the following boundary conditions:

$$@ x = 0, \frac{d^2 y}{dx^2} = \frac{d^3 y}{dx^3} = 0$$

$$@ x = 2.8, y = 0$$

$$@ x = 6.9, y = \frac{d^2 y}{dx^2} = 0$$

so that

$$y = e [540 - 210x + x^4 - .087x^5]$$

Invoking the Rayleigh Principle, that is,

$$\frac{1}{2} \int_0^L EI \left(\frac{d^2 y}{dx^2} \right)^2 dx = \frac{1}{2} \int_0^L m y^2 \omega_c^2 dx$$

where m = rotor mass per unit length, and

ω_c = first critical speed frequency

a numerical integration leads to:

$$\omega_c = 284,000 \text{ RPM which is over five times higher than the maximum rotor speed of } 53,800 \text{ RPM.}$$

b. Bearing Thrust

With design point pressures acting on the turbine rotor, an axial thrust of 99 lbs is developed. Two angular contact bearings installed back-to-back, and spaced by two equal length race spacers, support the rotor. The basic dynamometer design employs outer race spring loaders to make the unit suitable for a wide variety of applications. However, for this application, in order to obtain high axial stiffness and best overall bearing performance, the loading springs will be removed so that bearing preloads will be imposed across rigid spacers.

The bearings are of a basic 202 size and will use a conservative 10° contact angle. Standard AFBMA ratings indicate a dynamic thrust capacity of approximately 1100 pounds for the bearing which, at 53,800 RPM and 99 lbs thrust load corresponds to a B_{10} life of:

$$\frac{1100^3}{99} \frac{10^6}{53,800(60)} = 425 \text{ hrs,}$$

which is considered acceptable for the program.

3. INSTRUMENTATION

The air turbine air flow instrumentation will take the following measurements:

1. Turbine inlet temperature.
2. Turbine differential temperature.
3. Turbine inlet static pressure.
4. Turbine inlet to nozzle outlet differential pressure.
5. Turbine nozzle outlet to wheel outlet differential pressure.
6. Turbine inlet to diffuser outlet differential pressure.
7. Turbine inlet air flow rate.

In addition, the dynamometer will supply shaft torque data and an electronic counter will be used to measure shaft rotational speed.

The purpose of the above instrumentation is to generate sufficient data from which turbine performance can be compared to design values, and to enable the cause of any discrepancies between observed and expected performance to be determined. Differential temperature and pressure measurements will be required in order to achieve the required accuracy. The purpose of each measurement is covered completely under CRU instrumentation.

There is one significant difference between the air turbine test setup and the CRU turbine setup. The CRU turbine has room for a full turbine exhaust diffuser of efficient design. The air turbine test setup has a very short diffuser followed by a short, constant area turn which dumps the turbine exhaust flow into the turbine housing. This configuration was necessary in order to limit the overhang of the turbine on the dynamometer high speed shaft bearings, and thereby assure the dynamic stability of this assembly at the highest speeds anticipated for the air turbine tests. It was considered impractical to arrange the turbine with the inlet side closer to the dynamometer than the exhaust side, since the leakage flow which escapes through the dynamometer shaft seal would then leave the turbine flow system at a point between the nozzle and the turbine rotor. It was considered that this leakage would modify the turbine system flow characteristics to an extent that would detract from the validity of the test results.

Due to the nature of the air turbine exhaust flow path it is necessary to estimate the turbine exhaust total pressure using conventional compressible fluid flow relationships from the static pressure measurement taken at the

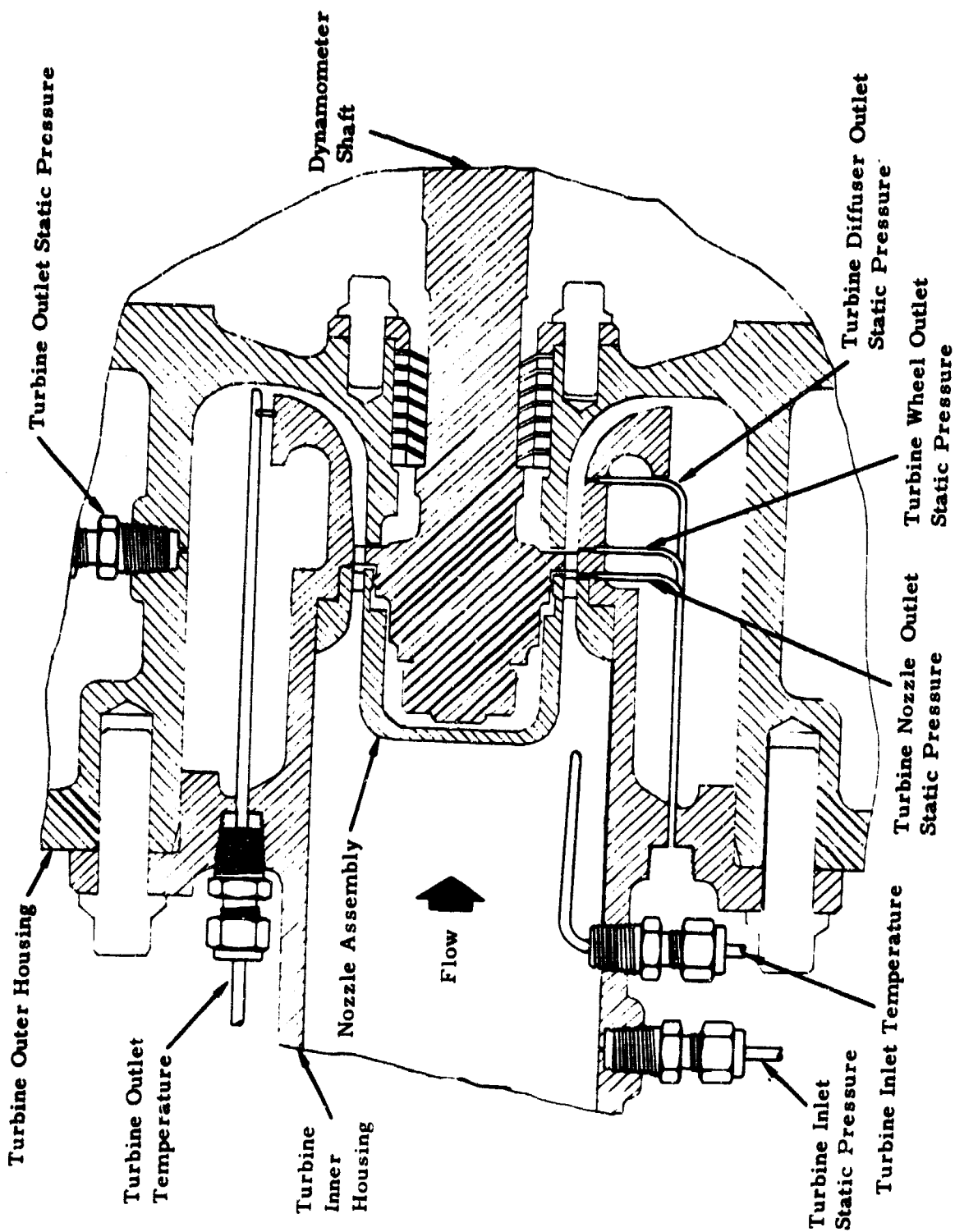
wheel exit and the discharge temperature and air flow rate measurements. The static pressure measurements at the end of the short diffuser will allow a check to be made upon the turbine wheel exit static pressure measurements since the turbulence and blade wake frequency perturbations in the static pressure at the wheel exit will have been largely damped in the diffuser. As in the case of the CRU, all pressure and temperature measurements will be taken at three points equally spaced circumferentially at each location to obtain circumferential temperature and pressure distributions and to provide data reliability through redundancy. The absolute temperatures will be sensed with thermocouples and recorded on a multipoint potentiometer recorder with an accuracy of $\pm 1\%$. The differential temperatures will be recorded with an accuracy of $\pm 2\%$. The absolute pressures and differential pressures will be read on bourdon and bellows type gauges respectively with an accuracy of $\pm 1/2\%$. Flow rate will be measured on the inlet side of the turbine by a calibrated laminar flow type meter with an accuracy of $\pm 0.5\%$. Shaft torque transmitted to the dynamometer will be measured with an accuracy of $\pm 1\%$ of full scale. Shaft speed will be measured with an accuracy of ± 60 RPM equivalent to $\pm 0.11\%$ of the equivalent air test design point speed.

Figure 53 is an enlargement of the turbine section of the air turbine assembly as shown in Figure 50 of the design section of this report, and shows the location of all thermocouples and pressure lines. All thermocouple probes are $1/16$ inch outside diameter and will be attached to the turbine inner housing with Swagelok compression fittings. The turbine inlet thermocouples will be attached, and the probes bent at right angles as shown, after the nozzle assembly is installed within the housing. The end of the turbine outlet temperature probe will be supported by small brackets spot welded to the thermocouple sheath and to the housing.

The turbine nozzle outlet, turbine wheel outlet and the diffuser outlet static pressure tap holes will each be connected to a $1/32$ inch outside diameter tube which will be seal bonded into a countersunk recess in the outside surface of the turbine inner housing. The other end of each tube will be seal bonded into a matching hole in the outer wall portion of the housing. A standard compression fitting then connects each of these holes to the appropriate pressure measuring instrument through standard instrumentation tubing.

As shown in Figure 53, the turbine inlet static pressure measurement is straightforward and requires no explanation (this pressure should be very close to the total pressure due to the low air velocity at the sense port).

All probes and pressure tubes will be checked out on the turbine inner housing prior to installation of the complete assembly into the turbine outer housing.



1975

Figure 53. Air Turbine Instrumentation

Section V

CONCLUSIONS AND RECOMMENDATIONS

1. CONCLUSIONS

As a result of the CRU and Air Turbine Preliminary Designs the following conclusions have been drawn.

1. The XFCTAP 01-01 CRU can be built with current technology and with a high degree of confidence that the unit will perform as intended.
2. The turbine wheel and nozzle can be fabricated to specifications by several methods which will result in the desired turbine design efficiency of about 0.70.
3. Information relating to turbine fabrication is interpreted as being indicative that the pump and diffuser can be fabricated to specifications that will result in the desired pump design efficiency of about 0.67.
4. The CRU design speed is below the first critical speed of the rotor allowing subcritical speed operation for all tests.
5. The rotor can be operated on working fluid bearings of the self-acting type with ample stiffness and load carrying capacity and acceptable losses based on analysis.
6. Both the CRU and Air Turbine Test Unit can be instrumented for making adequate measurements that will result in performance evaluation and will monitor and safeguard the units during testing.

2. RECOMMENDATIONS

Based on the knowledge gained during the preliminary designs and the conclusions drawn therefrom it is recommended that:

1. The preliminary designs be carried through final design and the unit be built and tested.
2. The turbine be tested in the Air Turbine Test Unit prior to testing in the CRU.
3. A simulated dynamic model of the CRU rotor be tested in a bearing test rig with supercritical CO₂ lubricant prior to testing the CRU.

This recommendation does not reflect a lack of confidence in the working fluid bearings but rather intends to insure a cost-effective CRU test program with the risks considerably

reduced. Pre-testing the rotor and working fluid bearings is analogous to pre-testing the turbine in the Air Turbine Test Unit.

REFERENCES

1. Feher, E. G., "The Supercritical Thermodynamic Power Cycle," Douglas Paper No. 4348, presented to the Intersociety Energy Conversion Engineering Conference, Miami Beach, Florida 13-17 Aug. 1967.
2. Sweigert, R. L., et al. "Thermodynamic Properties of Gases, Carbon Dioxide" Industrial and Engineering Chemistry, Vol. 38, No. 2, 1946, p. 185 ff.
3. Kennedy, G. C., "Pressure - Volume - Temperature Relations in CO₂ at Elevated Temperatures and Pressures," American Journal of Science Vol. 252, April 1954, p. 225-241.
4. Price, D., "The Thermodynamic Properties of Carbon Dioxide up to 1000°C and 1400 Bars - I. Entropy, Enthalpy and Isobaric Heat Capacity," NAVORD Report 3846, November 1954, U. S. Naval Ordnance Laboratory, White Oak, Md.
5. Newitt, D. M., et al. "Tables of Thermodynamic Functions of Carbon Dioxide," from Thermodynamic Functions of Gases, Vol. 1, edited by F. Din, Butterworths Scientific Publications, London, 1956.
6. Chen, L. H., Thermodynamic and Transport Properties of Gaseous Carbon Dioxide, ASME Book, Thermodynamic and Transport Properties of Gases, Liquids and Solids, McGraw-Hill Book Co., 1959.
7. Elrod and Malanoski, Theory and Design Data for Continuous Film, Self-Acting Journal Bearings of Finite Length, (The Franklin Institute) ASTIA AD278 660 Ref: Contract DAC-60528-F NONR 2342 (00) - Task NR 061-113 June 1962.
8. Smith and Fuller, "Journal-Bearing Operation at Superlaminar Speeds," ASME Trans. Vol. 78, 1956.
9. Constantinescu, "Analysis of Bearings Operating in Turbulent Regime," ASME J. of Basic Eng., March, 1962.
10. Boyd and Raimondi, "Applying Bearing Theory to the Analysis and Design of Journal Bearings - I and II," Design Data and Methods ASME, 1953.

11. Fuller, D. D., Theory and Practice of Lubrication for Engineers, John Wiley and Sons, 1956, p. 176.
12. Salter, Ludwig L., "Predicting Critical Speeds," Machine Design, June 25, 1959.
13. Sternlicht and Lewis, "Vibration Problems with High Speed Turbomachinery," ASME paper no. 67-DE-8.
14. Poritsky, "Contribution to the Theory of Oil Whip," Trans. ASME, Vol. 75, 1953, p. 1153-1161.
15. Graft, "Thermal Conductance Across Metal Joints," Machine Design, Sept. 15, 1960.
16. MIL-HDBK-5A, Metallic Materials and Elements for Aerospace Vehicle Structures.
17. Schenck, Hilbert Jr., Theories of Engineering Experimentation, McGraw-Hill Book Co., p. 46.

UNCLASSIFIED
Security Classification

DOCUMENT CONTROL DATA - R&D		
<small>(Security classification of title, body of abstract and indexing annotation must be entered when the overall report is classified)</small>		
1. ORIGINATING ACTIVITY (Corporate author) Astropower Laboratory, Douglas Missile and Space Systems Division, McDonnell Douglas Corporation, 2121 Campus Drive, Newport Beach, California		2a. REPORT SECURITY CLASSIFICATION Unclassified
		2b. GROUP
3. REPORT TITLE INVESTIGATION OF SUPERCRITICAL (FEHER) CYCLE		
4. DESCRIPTIVE NOTES (Type of report and inclusive dates) Final Technical Report - 1 July 1967 to 15 May 1968		
5. AUTHOR(S) (Last name, first name, initial) Feher, E. G. et al.		
6. REPORT DATE October 1968	7a. TOTAL NO. OF PAGES 136	7b. NO. OF REFS 18
8a. CONTRACT OR GRANT NO. F33615-67-C-1924	8b. ORIGINATOR'S REPORT NUMBER(S) DAC-60528-F	
8c. PROJECT NO. 3145		
8d. Task No. 314501	8e. OTHER REPORT NO(S) (Any other numbers that may be assigned this report) AFAPL-TR-68-100	
10. AVAILABILITY/LIMITATION NOTICES This document is subject to special export controls and each transmittal to foreign governments or foreign nationals may be made only with prior approval of the Air Force Aero Propulsion Laboratory, WPAFB, Ohio.		
11. SUPPLEMENTARY NOTES	12. SPONSORING MILITARY ACTIVITY Air Force Aero Propulsion Laboratory Air Force Systems Command United States Air Force	
13. ABSTRACT Preliminary Design of the XFCTAP 01-01 Combined Rotating Unit (CRU) is described in this report. The unit is intended for the investigation of Supercritical (Feher) cycle engine components. The CRU consists of a single stage axial reaction turbine, a single stage radial pump and a solid rotor alternator with its rotor supported on self-acting radial and thrust bearings with working fluid lubrication. The working fluid is supercritical CO ₂ . Net power output of the CRU is 10 kWe at a design speed of 80,000 RPM In addition, this report covers the design of an Air Turbine Test Configuration intended to verify the performance of the CRU turbine with compressed air under dynamically similar conditions prior to testing with high temperature supercritical CO ₂ . The air turbine test unit includes an air dynamometer. The turbine is attached to the dynamometer shaft for direct torque measurement. The housing provides means for regulating air flow rate. Both the CRU and the Air Turbine Unit are fully instrumented to yield data on pressures, temperatures, flow rates and electrical power from which the perform- ance of the various components can be determined. Investigation of the feasibility of miniaturized turbine fabrication resulted in the conclusion that these components can be made to specifications that will yield a turbine efficiency of about 0.70 and a pump efficiency of about 0.67 at the design point. The alternator efficiency is estimated to be about 0.89. It is recommended that these preliminary designs be carried through final design and that the units be fabricated and tested.		

DD FORM 1473
1 JAN 64

UNCLASSIFIED
Security Classification

UNCLASSIFIED
Security Classification

14 KEY WORDS	LINK A		LINK B		LINK C	
	ROLE	WT	ROLE	WT	ROLE	WT
Supercritical Cycle Feher Cycle Thermodynamic cycles Regenerative cycle Heat engines Prime movers Energy Conversion Dynamic energy conversion Combined rotating unit Turbo-pump-alternator Power System Power Conversion System						

INSTRUCTIONS

1. **ORIGINATING ACTIVITY:** Enter the name and address of the contractor, subcontractor, grantee, Department of Defense activity or other organization (*corporate author*) issuing the report.
- 2a. **REPORT SECURITY CLASSIFICATION:** Enter the overall security classification of the report. Indicate whether "Restricted Data" is included. Marking is to be in accordance with appropriate security regulations.
- 2b. **GROUP:** Automatic downgrading is specified in DoD Directive 5200.10 and Armed Forces Industrial Manual. Enter the group number. Also, when applicable, show that optional markings have been used for Group 3 and Group 4 as authorized.
3. **REPORT TITLE:** Enter the complete report title in all capital letters. Titles in all cases should be unclassified. If a meaningful title cannot be selected without classification, show title classification in all capitals in parenthesis immediately following the title.
4. **DESCRIPTIVE NOTES:** If appropriate, enter the type of report, e.g., interim, progress, summary, annual, or final. Give the inclusive dates when a specific reporting period is covered.
5. **AUTHOR(S):** Enter the name(s) of author(s) as shown on or in the report. Show last name, first name, middle initial. If military, show rank and branch of service. The name of the principal author is an absolute minimum requirement.
6. **REPORT DATE:** Enter the date of the report as day, month, year; or month, year. If more than one date appears on the report, use date of publication.
- 7a. **TOTAL NUMBER OF PAGES:** The total page count should follow normal pagination procedures, i.e., enter the number of pages containing information.
- 7b. **NUMBER OF REFERENCES:** Enter the total number of references cited in the report.
- 8a. **CONTRACT OR GRANT NUMBER:** If appropriate, enter the applicable number of the contract or grant under which the report was written.
- 8b, c, & 8d. **PROJECT NUMBER:** Enter the appropriate military department identification, such as project number, subproject number, system numbers, task number, etc.
- 9a. **ORIGINATOR'S REPORT NUMBER(S):** Enter the official report number by which the document will be identified and controlled by the originating activity. This number must be unique to this report.
- 9b. **OTHER REPORT NUMBER(S):** If the report has been assigned any other report numbers (*either by the originator or by the sponsor*), also enter this number(s).
10. **AVAILABILITY/LIMITATION NOTICES:** Enter any limitations on further dissemination of the report, other than those

imposed by security classification, using standard statements such as:

- (1) "Qualified requesters may obtain copies of this report from DDC."
- (2) "Foreign announcement and dissemination of this report by DDC is not authorized."
- (3) "U. S. Government agencies may obtain copies of this report directly from DDC. Other qualified DDC users shall request through _____."
- (4) "U. S. military agencies may obtain copies of this report directly from DDC. Other qualified users shall request through _____."
- (5) "All distribution of this report is controlled. Qualified DDC users shall request through _____."

If the report has been furnished to the Office of Technical Services, Department of Commerce, for sale to the public, indicate this fact and enter the price, if known.

11. **SUPPLEMENTARY NOTES:** Use for additional explanatory notes.
12. **SPONSORING MILITARY ACTIVITY:** Enter the name of the departmental project office or laboratory sponsoring (*paying for*) the research and development. Include address.
13. **ABSTRACT:** Enter an abstract giving a brief and factual summary of the document indicative of the report, even though it may also appear elsewhere in the body of the technical report. If additional space is required, a continuation sheet shall be attached.

It is highly desirable that the abstract of classified reports be unclassified. Each paragraph of the abstract shall end with an indication of the military security classification of the information in the paragraph, represented as (TS), (S), (C), or (U).

There is no limitation on the length of the abstract. However, the suggested length is from 150 to 225 words.
14. **KEY WORDS:** Key words are technically meaningful terms or short phrases that characterize a report and may be used as index entries for cataloging the report. Key words must be selected so that no security classification is required. Identifiers, such as equipment model designation, trade name, military project code name, geographic location, may be used as key words but will be followed by an indication of technical context. The assignment of links, rules, and weights is optional.